

UNIVERSITY OF CALIFORNIA  
RIVERSIDE

Measurement of the Transverse Single Spin Asymmetry and the Invariant Cross  
Section of Inclusive Eta Mesons Produced from Transversely Polarized  
Proton-Proton Collisions at Center of Mass Energy of 200 GeV.

A Dissertation submitted in partial satisfaction  
of the requirements for the degree of

Doctor of Philosophy

in

Physics

by

David William Kleinjan

March 2014

Dissertation Committee:

Dr. Kenneth Barish, Chairperson  
Dr. Richard Seto  
Dr. John Ellison

Copyright by  
David William Kleinjan  
2014

The Dissertation of David William Kleinjan is approved:

---

---

---

Committee Chairperson

University of California, Riverside

## Acknowledgments

Here begins both the easiest and hardest part of my thesis. As I write this on the eve of turning this work into the University, it is hard to believe that all that is left is to acknowledge all the people that made this work possible. Yet I know it will be difficult to remember everyone who gave me support in various ways throughout this adventure.

First and foremost I would like to thank my entire family. My parents Thomas and Carol Kleinjan have given nothing but their love, prayers, and support since I adventurously moved to California from South Dakota in the Fall of 2006. My four brothers Matt, Nick, Pete, and Ben were also always there for me when I needed them, even simple chats on the weekend with them and their families always lifted my spirits. In addition, so many friends come to mind, but I would particularly like to thank my close friends Seth Van Duyn, Nick Vande Weerd, and Wilt Hodges for always being there for moral support during graduate school.

So many people in my UCR physics group, both past and present, need to be thanked. First and foremost, I would like to thank my advisor for his continued support throughout my years as a graduate student. His calm demeanor and punctual clarity on how stay focused on the physics, as well as supporting me in all my travels for school, was extremely invaluable. Also thanks to Professor Richard Seto; post doctorate fellows Stephan Bathe, Paul Bourgeois, Ondrej Chvala, Oleg Eyser, Aneta Iordanova, and Richard Hollis; and fellow students Astrid Morràle, Tim Hester, Sky Rolnick, Matthew Mendoza, Ken Sedgwick, and Michael Beaumier.

Of course almost all of my research could not be done without support through the PHENIX collaboration, and so many names come to mind there is no way that

I can name them all. I would particularly like to thank Martin Purschke, Kensuke Okada, Christine Aidala, Mickey Chiu, John Koster, Beau Meredith, Matthais Grosse-Perdekemp, Ralf Seidl, Anselm Vossen, Sasha Bazilevsky, Joseph Seele, Frank Ellinghaus, Itaru Nakagawa, Abhay Desphande, Kieran Boyle, Todd Kempel, John Lajoie, Xiarong Wang, Mike McCumber, and Marzia Rosati. There are people in the greater field of Physics that I would also like to thank, from the beginnings of my career, to those in my same field. I would like to thank Keith Ruddick, Jon Urheim, Paul Crowell, and Rob Compton from my Undergraduate days at the University of Minnesota. In the wider field of nucleon spin physics, I would like to thank Marco Stratman, Markus Deihl, Delia Hasch, Alessandro Bacchetta, and Barbara Pasquini.

Special thanks must be noted among all the people that I have already mentioned. I would like to specially thank my analysis mentors Christine Aidala, Mickey Chiu, Oleg Eyser, and Richard Hollis, and my fellow MPC analyzers Beau Meredith and John Koster for their help in understanding the MPC framework. Their combined efforts, sometimes coordinated together and sometimes independent, was crucial in finishing this quality work. An additional special thanks is reserved for Richard Hollis and Oleg Eyser for their review of this thesis, as writing such a work is impossible without close editors to assist in its flow, clarity, and accuracy. I would also like to extend a special thanks to fellow UCR graduate students Tim Hester and Sky Rolnick—we really endured our graduate school experience at BNL together. Finally, I would also like to extend a very special thanks and regards to Michael Beaumier and John Koster, who during some of my hardest times in graduate school were there to help me pull through.

## ABSTRACT OF THE DISSERTATION

Measurement of the Transverse Single Spin Asymmetry and the Invariant Cross Section of Inclusive Eta Mesons Produced from Transversely Polarized Proton-Proton Collisions at Center of Mass Energy of 200 GeV.

by

David William Kleinjan

Doctor of Philosophy, Graduate Program in Physics  
University of California, Riverside, March 2014  
Dr. Kenneth Barish, Chairperson

The measurement of transverse single spin asymmetries provides insight into the structure of the nucleon. Originally expected to be small, results from PHENIX and other experiments show significant asymmetries in the forward momentum direction of the polarized proton over a wide range of center-of-mass energies. Several mechanisms have been proposed that attempt to explain these asymmetries, which include initial and final state effects based on transverse momentum dependent distributions and perturbative Quantum Chromodynamic (pQCD) calculations at higher twist. Studying the species, and the kinematic dependencies of these transverse single spin asymmetries will help to disentangle the origin of the observed asymmetries. Using the PHENIX detector at the Relativistic Heavy Ion Collider (RHIC), the cross section and transverse single spin asymmetry ( $A_N$ ) of inclusive  $\eta$  mesons produced from transversely polarized proton-proton collisions at center of mass energy of 200 GeV at forward rapidity is measured. pQCD is found to be consistent with the results of this measured cross section, and a sizeable non-zero transverse single spin asymmetry is found in the forward direction.

# Contents

<b>List of Figures</b>	<b>x</b>
<b>List of Tables</b>	<b>xiii</b>
<b>1 Introduction</b>	<b>1</b>
1.1 The Spin of the Proton . . . . .	2
1.2 Studying the Proton with Polarized Proton-Proton Collisions . . . . .	3
1.3 Objectives and Outline of This Work . . . . .	4
<b>2 The Structure of the Proton</b>	<b>5</b>
2.1 Perturbative QCD in Proton-Proton Collisions . . . . .	5
2.1.1 Universality and Factorization . . . . .	5
2.1.2 Cross Section Measurements and pQCD . . . . .	8
2.2 The Structure of the Proton . . . . .	9
2.2.1 Unpolarized Proton Structure . . . . .	9
2.2.2 Longitudinal Proton Structure . . . . .	10
2.2.3 Transverse Proton Structure . . . . .	12
2.2.4 Transverse Momentum Dependent Proton Structure . . . . .	13
2.3 Non-Zero $A_N$ Measurements . . . . .	16
2.3.1 The Sivers Effect . . . . .	17
2.3.2 The Collins Effect . . . . .	18
2.3.3 Higher-Twist effects . . . . .	18
2.3.4 Unified Picture . . . . .	19
2.4 $A_N$ of $\eta$ Mesons . . . . .	20
<b>3 Experimental Setup</b>	<b>23</b>
3.1 Relativistic Heavy Ion Collider . . . . .	23
3.1.1 Polarized Proton Source . . . . .	24
3.1.2 RHIC-AGS complex . . . . .	24
3.1.3 Siberian Snakes . . . . .	25
3.1.4 Spin Rotator . . . . .	26
3.1.5 Polarimetry . . . . .	26
3.1.5.1 p-C Polarimeter . . . . .	27
3.1.5.2 H-Jet Polarimeter . . . . .	27
3.1.6 Luminosity Monitoring and Local Polarimetry, the Zero Degree Calorimeter . . . . .	28

3.2	The PHENIX Detector . . . . .	29
3.2.1	Central Arm Spectrometers . . . . .	31
3.2.2	Muon Arms . . . . .	31
3.2.3	Global Detectors . . . . .	32
3.2.4	Data Acquisition in PHENIX . . . . .	32
3.3	A Forward Calorimeter in PHENIX, the MPC Detector . . . . .	33
3.3.1	Introduction to Electromagnetic Calorimetry . . . . .	35
3.3.2	MPC Specifications . . . . .	36
3.3.3	ADC to energy conversion in the MPC . . . . .	37
<b>4</b>	<b>Measurement of the Invariant Cross Section</b>	<b>38</b>
4.1	Quality Assurance . . . . .	39
4.1.1	MPC Warnmap . . . . .	39
4.1.2	Run Quality Assurance . . . . .	41
4.2	Event Selection Criteria . . . . .	44
4.3	Identification of $\eta$ Mesons . . . . .	45
4.3.1	Combinatorial Background Subtraction . . . . .	47
4.3.2	Yield extraction . . . . .	48
4.4	Corrections for the $\eta$ meson yields . . . . .	54
4.4.1	Single $\eta$ Meson Simulations . . . . .	55
4.4.2	Reconstruction Efficiency . . . . .	58
4.4.3	$\eta$ meson Minimum Bias trigger efficiency . . . . .	62
4.4.4	The $\eta$ meson $4 \times 4B$ trigger efficiency . . . . .	64
4.5	Luminosity . . . . .	67
4.5.1	Integrated Luminosity of the Minimum Bias Trigger . . . . .	68
4.5.2	Luminosity of the $4 \times 4B$ Trigger . . . . .	68
4.6	Systematic studies . . . . .	69
4.6.1	Energy Scale . . . . .	69
4.6.1.1	Functional Form . . . . .	69
4.6.1.2	Reconstruction Efficiency . . . . .	70
4.6.2	Yield extraction . . . . .	72
4.6.3	Mixed Event Subtraction . . . . .	75
4.6.4	GEANT . . . . .	76
4.6.5	$\eta$ meson $4 \times 4B$ trigger efficiency . . . . .	76
4.6.6	BBC cross section . . . . .	78
4.7	Bin Shift Correction . . . . .	78
4.8	Results . . . . .	81
<b>5</b>	<b>The measurement of <math>\eta</math> meson <math>A_N</math></b>	<b>85</b>
5.1	Kinematic Dependence of $A_N$ . . . . .	87
5.2	Formulae for Measuring $A_N$ . . . . .	88
5.3	Beam Polarization . . . . .	89
5.4	Quality Assurance . . . . .	90
5.4.1	Warnmap . . . . .	90
5.4.2	Run Spin Information Quality Assurance . . . . .	92
5.5	Yield Extraction and Correction for Background Sources . . . . .	92
5.5.1	Asymmetry in the Background Regions . . . . .	93
5.5.2	Simulation Studies of Correlated Background . . . . .	97

5.6	Obtaining the Asymmetry . . . . .	99
5.6.1	Asymmetry in the $\eta$ Meson Peak Region . . . . .	100
5.6.2	Calculation of Background Asymmetry . . . . .	109
5.6.3	Background Corrected $A_N$ . . . . .	109
5.6.4	Comparison of South and North MPC $A_N$ . . . . .	111
5.7	$p_T$ Dependence of Asymmetries . . . . .	112
5.8	Cross-checks and Systematics . . . . .	113
5.8.1	Systematic Uncertainty on the Fitting of the Background . . . . .	113
5.8.2	Systematic Uncertainty from Even-Odd Bunch Crossings . . . . .	114
5.8.3	Bunch Shuffling . . . . .	122
5.9	Final Asymmetry . . . . .	125
<b>6</b>	<b>Results and Discussion</b>	<b>127</b>
6.1	Cross section of $\eta$ mesons at forward rapidity . . . . .	127
6.2	$A_N$ of $\eta$ mesons as a function of $x_F$ . . . . .	129
6.3	$A_N$ of $\eta$ mesons as a function of $p_T$ . . . . .	131
6.4	Outlook . . . . .	133
<b>7</b>	<b>Conclusions</b>	<b>135</b>
<b>A</b>	<b>Tables For Cross Section</b>	<b>136</b>
A.1	The Minimum Bias Measured Spectra, invariant yields, corrections, and cross sections For the South and North MPC . . . . .	137
A.2	The Minimum Bias cross section and systematic errors . . . . .	138
A.3	The $4 \times 4B$ measured spectra, invariant yields, corrections, and cross sections For the South and North MPC . . . . .	139
A.4	The $4 \times 4B$ cross section and systematic errors . . . . .	140
<b>B</b>	<b>Tables For <math>A_N</math> vs <math>x_F</math></b>	<b>141</b>
B.1	$A_N$ vs $x_F$ Minimum Bias triggered dataset . . . . .	142
B.2	$A_N$ vs $x_F$ for $4 \times 4B$ triggered dataset . . . . .	142
B.3	$A_N$ vs $x_F$ final . . . . .	143
<b>C</b>	<b>Plots for <math>A_N</math> vs <math>p_T</math></b>	<b>144</b>
<b>D</b>	<b>Tables for <math>A_N</math> vs <math>p_T</math></b>	<b>148</b>
D.1	$A_N$ vs $p_T$ South and North . . . . .	149
D.2	$A_N$ vs $p_T$ final . . . . .	150
<b>E</b>	<b>Bunch shuffling plots</b>	<b>151</b>
	<b>Bibliography</b>	<b>156</b>

# List of Figures

2.1	Factorization of $p + p \rightarrow h + X$	6
2.2	The Cross Section of $\eta$ mesons at mid-rapidity in PHENIX	9
2.3	Unpolarized Parton Distribution	10
2.4	Longitudinal Parton Distribution Functions	12
2.5	TMD Parton Distribution Functions	15
2.6	$A_N$ of $\pi^0$ mesons	16
2.7	Sivers TMD quark density distribution in transverse-momentum-space	17
2.8	Transversity PDF and Collins FF for charged pions.	19
2.9	$A_N$ versus $p_T$ , Unified picture	20
2.10	$A_N$ of $\eta$ mesons	21
2.11	Twist-3 Prediction for $\eta$ and $\pi^0$ mesons	21
3.1	The Relativistic Heavy Ion Collider (RHIC)	24
3.2	Local Polarimetry	29
3.3	The PHENIX Detector	30
3.4	The MPC Detector	34
3.5	A $PbWO_4$ crystal tower (left panel) and an APD preamp attached to the front of a crystal (right panel).	37
4.1	Warnmap for Minimum Bias Triggered Data	40
4.2	Warnmap for $4 \times 4B$ Triggered Data	40
4.3	Photograph of Beam Pipe Stand	41
4.4	The yield per event Run QA.	42
4.5	The peak position Run QA.	43
4.6	The peak standard deviation Run QA.	44
4.7	Mixed Event Subtraction	48
4.8	Measured Spectra	49
4.9	South MPC Invariant Mass Distributions. Minimum Bias trigger	50
4.10	North MPC Invariant Mass Distributions. Minimum Bias trigger	51
4.11	South MPC Invariant Mass Distributions. $4 \times 4B$ trigger	52
4.12	North MPC Invariant Mass Distributions. $4 \times 4B$ trigger	53
4.13	Single $\eta$ Meson Simulation Kinematics	55
4.14	$z$ -vertex distribution of Single $\eta$ Mesons	56
4.15	Reconstructed Single $\eta$ mesons from Simulations	57
4.16	Reconstruction Efficiencies	60
4.17	$p_T$ weighting	60

4.18	Minimum Bias Pseudorapidity Weighting.	61
4.19	$4\times 4B$ Pseudorapidity Weighting.	61
4.20	The $\eta$ meson Minimum Bias trigger efficiency in the South (red) and North (blue) MPC	63
4.21	$4\times 4id$ Trigger Efficiency as a function of ADC	65
4.22	The $\eta$ meson $4\times 4B$ trigger efficiency	67
4.23	Luminosity of $4\times 4B$ Trigger	69
4.24	Energy Scale Systematic Error	70
4.25	Reconstruction efficiencies adjusted by the Energy Scale	71
4.26	Energy Scale Systematic Error	71
4.27	Variation of Background Fits, Minimum Bias Triggered Data, South MPC	73
4.28	Yield Extraction Systematics, Variant Fits	74
4.29	Final Yield Extraction Systematic Error	74
4.30	Real to Mixed Event Ratios	75
4.31	Mixed Event Subtraction Systematic	76
4.32	Systematic on $\epsilon_{reco}$	77
4.33	Variation of Simulated $\epsilon_{4\times 4B}^{cl}$	79
4.34	Ratio between Simulated and Real $\epsilon_{4\times 4B}^{cl}$	80
4.35	Variation of Simulated $\epsilon_{4\times 4B}^{\eta}$	80
4.36	Systematic Error on $\epsilon_{4\times 4B}^{\eta}$	81
4.37	Cross Section for the South and North MPC	82
4.38	T-test for Cross Section	83
4.39	Final Cross Section	83
4.40	Cross Section comparisons	84
4.41	Cross Section comparisons	84
5.1	Fill patterns in RHIC	87
5.2	Warnmap for Minimum Bias Triggered Data	91
5.3	Warnmap for $4\times 4B$ Triggered Data	91
5.4	Extraction of $\eta$ meson mass range	93
5.5	Spin Dependent Invariant Mass Plot	94
5.6	$\eta$ Meson Mass Spectra, with sideband regions	96
5.7	Decomposition of cluster parents contributing to the invariant mass distribution in the $\eta$ mass range	99
5.8	$\epsilon_{sqrt}$ asymmetries for South MPC, in the $\eta$ peak region	101
5.9	$\epsilon_{sqrt}$ asymmetries for North MPC, in the $\eta$ peak region	102
5.10	$\epsilon_{pol}$ asymmetries for South MPC, in the $\eta$ peak region	103
5.11	$\epsilon_{pol}$ asymmetries for North MPC, in the $\eta$ peak region	104
5.12	Raw Asymmetry Fit Parameters for the South MPC	106
5.13	Raw Asymmetry Fit Parameters for the North MPC	106
5.14	Asymmetries in the $\eta$ mass region	108
5.15	$x_F$ Asymmetries in the Background Regions	109
5.16	The measured background asymmetry, $A_N^{bg}$	110
5.17	$4\times 4B$ background corrected values of $x_F$ dependent $A_N^{\eta}$	110
5.18	Statistical uncertainty checks on $A_N$ , $4\times 4B$ trigger	111
5.19	Statistical uncertainty checks on $A_N$ , Minimum Bias trigger	111
5.20	The combined South and North MPC $A_N$ measured as a function of $x_F$	112
5.21	The combined South and North MPC $A_N$ measured as a function of $p_T$	113

5.22	Invariant mass spectra fit with different assumed background functions for $\eta$ meson peak region . . . . .	114
5.23	The fill pattern even-odd comparison for the South MPC . . . . .	116
5.24	The fill pattern even-odd comparison for the North MPC . . . . .	117
5.25	The fill pattern systematic calculations for the South MPC. . . . .	118
5.26	The fill pattern systematic calculations for the North MPC. . . . .	119
5.27	Fill pattern Systematic $\delta A_N$ Values . . . . .	120
5.28	The absolute systematic uncertainties for the $x_F$ dependent $A_N$ . . . . .	121
5.29	The absolute systematic uncertainties for the $p_T$ dependent $A_N$ . . . . .	121
5.30	The $x_F$ bunch shuffling results for $4 \times 4B$ triggered dataset using the North MPC using $\epsilon_{sqrt}$ formula. . . . .	123
5.31	The $x_F$ bunch shuffling results for $4 \times 4B$ data using the North MPC using $\epsilon_{pol}$ formula. . . . .	124
5.32	The final $x_F$ dependence of $A_N$ . . . . .	125
5.33	The final $p_T$ dependence of $A_N$ . . . . .	126
6.1	The cross section of inclusive $\eta$ mesons produced from $p + p$ collisions at $\sqrt{s} = 200$ GeV . . . . .	128
6.2	The $p_T$ Dependence of $A_N$ . . . . .	129
6.3	Comparison between the $\eta$ meson $A_N$ and other $\pi^0$ and $\eta$ meson $A_N$ results	131
6.4	The $p_T$ dependence of $A_N$ . . . . .	132
6.5	Comparison between the twist-3 prediction of $\eta$ $A_N$ as a function of $p_T$	133
C.1	Asymmetries in the $\eta$ mass region. The left (right) is for the South (North) MPC. The top panels display the raw asymmetry, and the blue points in these figures are used to calculate $A_N$ , shown in the bottom panels) . . . . .	145
C.2	$p_T$ Asymmetries in the Background Regions . . . . .	146
C.3	$4 \times 4B$ background corrected values of $p_T$ dependent $A_N^\eta$ . . . . .	146
C.4	Minimum Bias background corrected values of $p_T$ dependent $A_N^\eta$ . . . . .	147
E.1	Bunch Shuffling Minimum Bias South MPC, $x_F$ dependence, $\epsilon_{sqrt}$ formula	152
E.2	Bunch Shuffling Minimum Bias North MPC, $x_F$ dependence, $\epsilon_{sqrt}$ formula	152
E.3	Bunch Shuffling $4 \times 4B$ South MPC, $x_F$ dependence, $\epsilon_{sqrt}$ formula . . .	153
E.4	Bunch Shuffling Minimum Bias South MPC, $x_F$ dependence, $\epsilon_{pol}$ formula	154
E.5	Bunch Shuffling Minimum Bias North MPC, $x_F$ dependence, $\epsilon_{pol}$ formula	154
E.6	Bunch Shuffling $4 \times 4B$ South MPC, $x_F$ dependence, $\epsilon_{pol}$ formula . . .	155

# List of Tables

3.1	Specifications of the MPC $PbWO_4$ crystals. . . . .	36
5.1	Signal to background ratios binned in $x_F$ . . . . .	95
A.1	The invariant yield, reconstruction efficiency, bin shift correction, and invariant cross section for the South and North MPC . . . . .	137
A.2	The Minimum Bias cross section and systematic errors. . . . .	138
A.3	The invariant yield, reconstruction efficiency, bin shift correction, and invariant cross section for the South and North MPC . . . . .	139
A.4	The $4 \times 4B$ cross section and systematic errors. . . . .	140
B.1	The various $A_N$ values for the Minimum Bias triggered dataset. . . . .	142
B.2	The various $A_N$ values for the $4 \times 4B$ data. . . . .	142
B.3	The final $x_F$ dependent $A_N$ values. . . . .	143
D.1	The various $A_N$ values for the $p_T$ data. . . . .	149
D.2	The final $p_T$ dependent $A_N$ values. . . . .	150

# Chapter 1

## Introduction

Ever since the proton's magnetic moment was revealed by O. Stern *et al.* [1] to have a value of 2.79 larger than the Dirac magnetic moment, understanding nature at the level of the proton's internal picoverse has been a wide field of physics research. Deep Inelastic Scattering experiments (DIS) of electrons inelastically scattered off protons found that the electrons were elastically scattering off of sub-particle components, called *partons* [2, 3, 4]. These partons, which carry a certain momentum fraction of the original proton's momentum, were later identified as *quarks*. DIS experiments revealed that about 50% nucleon's momentum fraction is dominated by three valence quarks, plus a sea of quark-antiquark pairs. The other 50% was later revealed to be *gluons* [5, 6, 7]. The theory describing the relationship between quarks and gluons inside the proton is called *Quantum Chromodynamics* (QCD), first formulated by Gross, Wilczek and Politzer [8, 9].

## 1.1 The Spin of the Proton

The proton is a fermion, its spin is  $S_p = \frac{1}{2}\hbar$ . In the naïve quark-parton model, the three valence quarks (quarks are also fermions,  $S_q = \frac{1}{2}\hbar$ ) in the proton were assumed to carry the spin of the proton. This was put to the test by *longitudinally polarized* DIS experiments. Results from these experiments culminated with the EMC experiment [10, 11], which found that only  $\sim 20\%$  of the proton's spin is carried by the quarks!

In addition, since spatial rotations and Lorentz boosts do not commute, studies of the transverse nature of the proton reveal a different picture of the proton from that of the longitudinal picture. In particular, *transverse single spin asymmetries* ( $A_N$ ) were measured for inclusive hadrons ( $h$ ) produced from inelastic proton-proton collisions, where one of the two protons is transversely polarized ( $p^\uparrow + p \rightarrow h + X$ )

$$A_N(p^\uparrow + p \rightarrow h + X) = \frac{\sigma^\uparrow - \sigma^\downarrow}{\sigma^\uparrow + \sigma^\downarrow}. \quad (1.1)$$

The E704 experiment at Fermilab found  $A_N$  to be non-zero and large ( $\mathcal{O}(10^{-1})$ ) for pion production [12, 13], which like the results from the EMC experiment was a surprise, as  $A_N$  was predicted to be very small ( $A_N \sim 10^{-4}$ ) based on QCD calculations.

These early results on probing the nuclear spin structure revealed that the proton internal nature is much more complicated than originally thought. What will further studies reveal about the structure of the proton?

## 1.2 Studying the Proton with Polarized Proton-Proton Collisions

Upon a deeper examination of QCD, the spin-1/2 of the proton has contributions from the quark spin ( $\Delta\Sigma$ ) and gluon spin ( $\Delta G$ ), and quark ( $L_q$ ) and gluon ( $L_g$ ) angular momentum [14, 15, 16]

$$S_{proton} = \frac{1}{2} = \frac{1}{2}\Delta\Sigma + L_q + \Delta G + L_g \quad (1.2)$$

With the pieces of this proton spin puzzle in hand, the natural step is to measure contributions from each component: the quark spin contribution, the gluon spin, and the partonic orbital angular momentum effects. The valence quark contribution to  $\Delta\Sigma$  contribution is well known, but the sea-quark spin contribution is less constrained ( $\Delta\Sigma = \Delta u + \Delta\bar{u} + \Delta d + \Delta\bar{d} + \Delta s + \Delta\bar{s}$ ), the gluon spin contribution,  $\Delta G$ , is only partially accessible from polarized DIS [17], and orbital momentum effects remain largely unexplored.

For the latest studies, the Relativistic Heavy Ion Collider (RHIC) at Brookhaven National Laboratory is used, which is the only polarized proton-proton collider in the world. It has the ability to collide longitudinally or transversely polarized protons at center of mass collision energies as high as 510 GeV. The RHIC spin program explores the spin of the proton on several fronts. The gluon spin contribution,  $\Delta G$  will be measured to much better certainty than previous DIS measurements could provide, since gluon interactions are directly accessed at leading order pQCD in proton-proton collisions. Flavor separated anti-quark distributions  $\Delta\bar{u}$  and  $\Delta\bar{d}$  will be measured through the parity violation of  $W$ -bosons. The transverse structure of protons will also be stud-

ied, which may provide insight into parton angular momenta, as well as highlight the differences between the transverse and longitudinal picture of the proton. A current review of the RHIC spin program's achievements and outlook is given in [18].

### 1.3 Objectives and Outline of This Work

The objective of this Thesis is to study the transverse nature of the proton by measuring the *invariant cross section*,  $\sigma(p + p \rightarrow \eta + X)$ , and transverse single spin asymmetry,  $A_N(p^\uparrow + p \rightarrow \eta + X)$ , of inclusive  $\eta$  mesons at forward rapidity produced from transversely polarized proton-proton collisions at RHIC at center of mass collision energy of  $\sqrt{s} = 200$  GeV. An overview of the proton-proton collision process and a current understanding of the structure of the proton will be discussed first, with emphasis on their relationship to the measurements highlighted. Then a review of the RHIC polarized proton-proton collider facility and the PHENIX experiment and detectors used for the measurements will be given, followed by an in-depth description of the analysis procedure used to procure the measurements of  $\sigma(p + p \rightarrow \eta + X)$  and  $A_N(p^\uparrow + p \rightarrow \eta + X)$ . A final chapter is reserved for discussion of the results derived from these these measurements.

## Chapter 2

# The Structure of the Proton

### 2.1 Perturbative QCD in Proton-Proton Collisions

Consider an inelastic collision between two protons that produces a hadron,  $p_1 + p_2 \rightarrow h + X$ . At the partonic level, this is a collision of  $a + b \rightarrow c$ . Here  $a$  represents the parton from the first proton,  $b$  represents the parton from second proton, and  $c$  represents the scattering of either parton  $a$  or  $b$ , which in turn *fragments* into hadron  $h$  (plus other  $X$ ). The primary concept that underlies all of RHIC spin physics is the predictive power of *perturbative* QCD (pQCD) [19] in calculating the cross section  $\sigma(p_1 + p_2 \rightarrow h + X)$ .

#### 2.1.1 Universality and Factorization

In the collinear<sup>1</sup> framework of pQCD, the cross section  $\sigma(p_1 + p_2 \rightarrow h + X)$  can be understood and calculated in terms of *Factorization* and *Universality*. The collinear factorization theorem states that large scale momentum interactions can be

---

<sup>1</sup>Collinear means that the momentum of the parton inside the proton is entirely along the proton's momentum, *i.e.* there is no transverse momentum Dependent (TMD) contribution to the parton's momentum. The case of non-zero TMD contributions will be discussed in Section 2.2.4

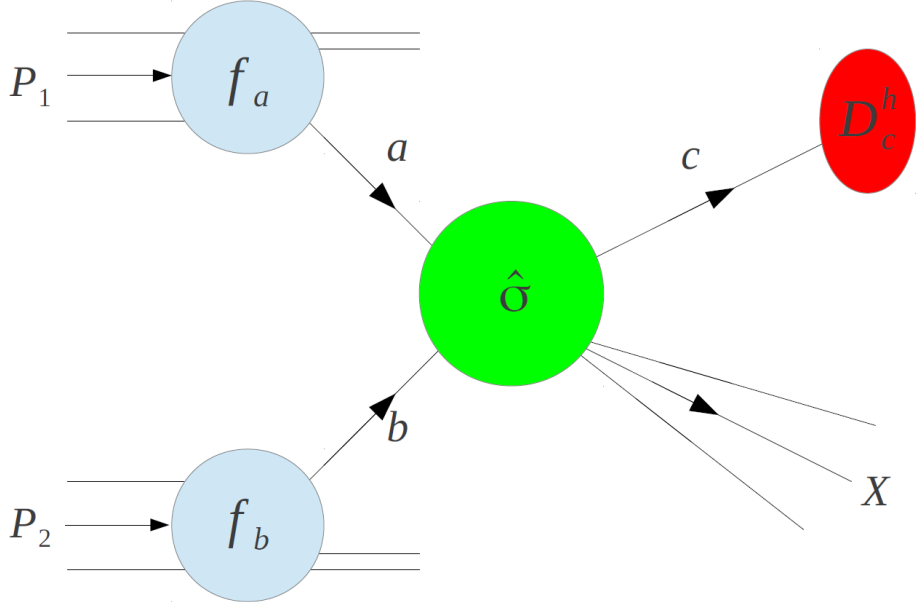


Figure 2.1: The Factorization of  $p+p \rightarrow h+X$  in terms of the parton densities, partonic hard scattering, and fragmentation functions

factorized into long distant (soft, or nonperturbative) and short (hard, or perturbative) distant reactions [20, 21]. The factorization theorem applied to inelastic proton-proton collisions, demonstrated by a graphic shown in Fig. 2.1, yields

$$d\sigma(p+p \rightarrow h+X) = \sum_{a,b,c} f_a(x_a, \mu_F) \otimes f_b(x_b, \mu_F) \otimes d\hat{\sigma}_{abc}(x_a, x_b, z_c, \mu_R, \mu_F) \otimes D_c^h(z_c, \mu'_F) \quad (2.1)$$

in which  $x_{a,b}$  represent the fraction of proton momenta carried by parton  $a, b$ , and  $f_{a,b}$  represent the parton's momentum density function, called the *parton distribution function* (PDF). The parton distribution function represents the probability of finding a parton with proton momentum fraction  $x$ .  $D_c^h$  is the fragmentation function (FF), which represents the probability of parton  $c$  fragmenting into hadron,  $h$  (carrying momentum fraction  $z_c$  of parton  $c$ 's momentum).  $f_a$ ,  $f_b$ , and  $D_c^h$  represent the soft part of

factorization, and must be measured experimentally. The hard part of the interaction is contained in the hard partonic cross section,  $d\hat{\sigma}$ , which is calculable in pQCD. Another way to view factorization is that it separates the initial and final states of the interaction from the interaction itself, *i.e.* the interaction state.

The dividing line between soft and hard scales is contained in the factorization scale  $\mu_F$  in Eq. 2.1, which is on the order of the momentum transfer of the interaction ( $\mu_F \approx Q^2$ ). This is a purely theoretical construct, it represents the uncertainty in theoretical predictions of the interactions taking place in Eq. 2.1. The higher the order of pQCD used in the calculation, the more accurate the factorization scale is known. A similar factorization scale,  $\mu'_F$ , separates of the hard and soft scales in the fragmentation, and in theory is usually set to  $\mu_F$ . An additional renormalization scale,  $\mu_R$  related to  $\alpha_s$  is included in the hard scattering, and is also usually set to  $\mu_F$ . Since this is an experimental Thesis, for simplicity we shall neglect theoretical scaling factors from now on, and discuss PDFs, FFs in terms of the momentum fractions  $x_{a,b}$ ,  $z_c$  and, where necessary, in terms of the underlying momentum transfer ( $\mu_F \approx Q^2$ ). For a more in depth descriptive explanation of QCD and factorization scales, see [22, 23, 19]

The second assumption in pQCD is the principle of *universality*. Universality states that the initial and final state parton densities and fragmentation functions, respectively, are independent of the process involved, whether they occur in  $p + p$  collisions, DIS, Semi-Inclusive DIS (SIDIS), or electron-positron annihilation (SIA). For an example, if the fragmentation function  $D_c^h$  in Eq. 2.1 was measured from  $e + e^-$  annihilations, it could be used to calculate the parton density functions in Eq. 2.1. For an overview of  $p + p$ , DIS, SIDIS, and SIA, and their relations to one another in terms of PDFs and FFs, see [24].

### 2.1.2 Cross Section Measurements and pQCD

Once the soft components in Eq. 2.1 have been measured, pQCD factorization can be used to predict  $\sigma(p_1+p_2 \rightarrow h+X)$ . The cross section of  $\eta$  meson production versus transverse momentum ( $p_T$ ) measured by PHENIX for  $p+p \rightarrow \eta+X$  at  $\sqrt{s}=200$  GeV at mid-rapidity ( $|\eta| < 0.35$ )<sup>2</sup> is shown in Fig. 2.2 [25], with a comparison to a theoretical calculation using next to leading order (NLO) pQCD. This is one example of the power of pQCD to predict cross section of hadrons from proton-proton collisions.

The first goal of this Thesis is to measure  $\sigma(p+p \rightarrow \eta+X)$  at  $\sqrt{s}=200$  GeV at *forward-rapidity* ( $\eta \approx 3.5$ ). In terms of pQCD, the forward rapidity  $\eta$  meson cross section is interesting on its own merits for two reasons. First,  $\eta$  mesons measured at forward rapidity may possibly be produced from non-perturbative interactions, thus it will test pQCD factorization in the non-perturbative versus perturbative QCD limit. Second, the cross section can be used to further determine the values of the  $\eta$  meson fragmentation function. A *global analysis*<sup>3</sup> of the FF of  $\eta$  mesons is given in [26]. For  $z_{min}=0.2$ , the gluon dependent fragmentation function is known to  $\delta D_g^\eta = \pm 15\%$  from this global analysis, but  $u, d$  dependent fragmentation is less known to  $\delta D_{u,d}^\eta = {}^{+30}_{-20}$ . The forward rapidity  $\eta$  meson cross section will improve on these uncertainty values.

---

<sup>2</sup>  $\eta$ , called pseudorapidity, is defined as

$$\eta = -\ln \left[ \tan \left( \frac{\theta}{2} \right) \right] \quad (2.2)$$

where  $\theta$  is the polar angle with the beam axis

<sup>3</sup> *global analyses* use data from various collision types, whether  $p+p$ , DIS, SIDIS, or SIA at various energies to determine PDFs or FFs.

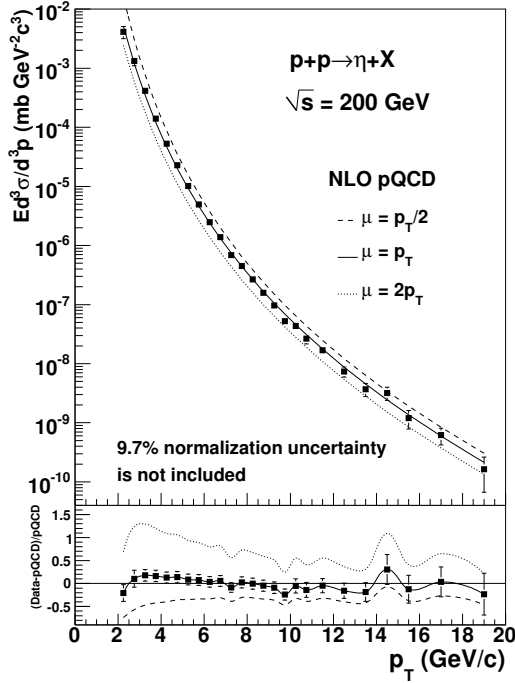


Figure 2.2: The Cross section of  $\eta$  mesons produced in  $p+p$  collisions at  $\sqrt{s} = 200$  GeV at mid-rapidity in PHENIX [25], compared to theoretical calculation using next to leading order (NLO) pQCD.

## 2.2 The Structure of the Proton

### 2.2.1 Unpolarized Proton Structure

The parton distribution functions in Eq. 2.1 are momentum density functions, written in terms of the momentum of the parent proton. For a proton with a given momentum,  $P$ , the probability that a parton carries momentum  $xP$  is given by

$$f(x) = \sum_{q,\bar{q},g} q_i(x) \quad (2.3)$$

Here  $f(x)$  represents the flavor integrated parton distribution function, whereas  $q_i(x)$  represents the quark-antiquark flavor and gluon separated parton distribution functions. Integration over the momentum fractions of the partons in Eq. 2.3 gives the PDF mo-

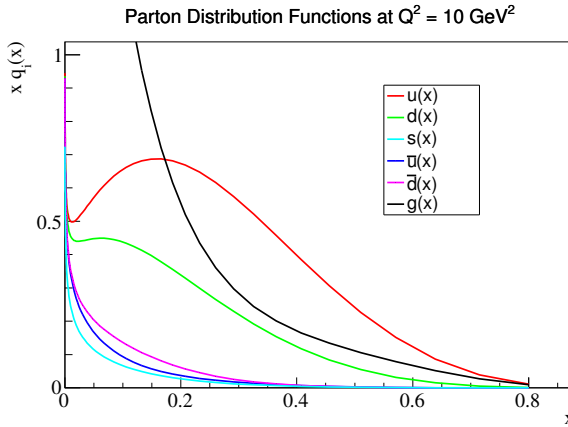


Figure 2.3: . The unpolarized parton distribution functions at  $Q^2 = 10 \text{ GeV}$ , calculated using the MRST scheme [27] using the PDF calculator found in [28].

momentum sum rule

$$1 = \sum_{q,\bar{q},g} \int_0^1 dx x q_i(x) \quad (2.4)$$

Experimental results from DIS revealed that the integration over the quark PDFs in Eq. 2.4 carry 50% of the proton's momentum fraction, which (mentioned in the Introduction) was the precursor for the prediction and discovery of gluons. The unpolarized PDFs are very well known. The PDFs at  $Q^2 = 10 \text{ GeV}$  are shown in Fig. 2.3.

### 2.2.2 Longitudinal Proton Structure

The longitudinal PDFs measure the spin density of partons in a proton whose spin vector is aligned parallel with its momentum. The longitudinal PDFs represent the probability that a quark in a proton with momentum fraction  $x$  carries spin parallel to the proton's spin minus spin anti-parallel to the proton's longitudinal spin.

$$\Delta f(x) = \sum_{q,\bar{q},g} \Delta q_i(x) \quad (2.5)$$

where  $\Delta q$  is defined as

$$\Delta q_i(x) = q^+(x) - q^-(x) \quad (2.6)$$

note that the unpolarized PDFs are simply

$$q_i(x) = q^+(x) + q^-(x) \quad (2.7)$$

The spin contribution of quarks and gluons to the total spin of the proton (see Eq. 1.2) are

$$\Delta\Sigma = \frac{1}{2} \sum_{q,\bar{q}} \int_0^1 dx x \Delta q_i(x) = \frac{1}{2} \int_0^1 dx x [\Delta q_i(x) + \Delta \bar{q}_i(x)] \quad (2.8)$$

$$\Delta G = \int_0^1 dx x \Delta q_g(x). \quad (2.9)$$

A global analysis, performed by De Florian, Sassot, Stratmann, and Vogelsang (DSSV) for the longitudinal PDFs [29], is shown in Fig. 2.4. From this analysis, it can be seen that the up-quark and down-quark distributions are well known. The sea quark and the gluon distributions are less well known.

Following up on what was mentioned in Section 1.2, measurements of  $W$ -boson longitudinal single spin asymmetries,  $A_L^{W\pm}$  at RHIC will provide a clean channel to significantly reduce the uncertainty on the sea quark distributions  $\Delta \bar{u}$  and  $\Delta \bar{d}$ .  $\Delta G$  is probed at RHIC by measuring longitudinal double spin asymmetries,  $A_{LL}^{inc}$ , of various inclusive processes.

Discussion on the status  $A_L^{W\pm}$  and  $\Delta G$  programs at RHIC can be found in [18]. Current measurements of  $A_L^{W\pm}$  show large non-zero asymmetries, while the preliminary

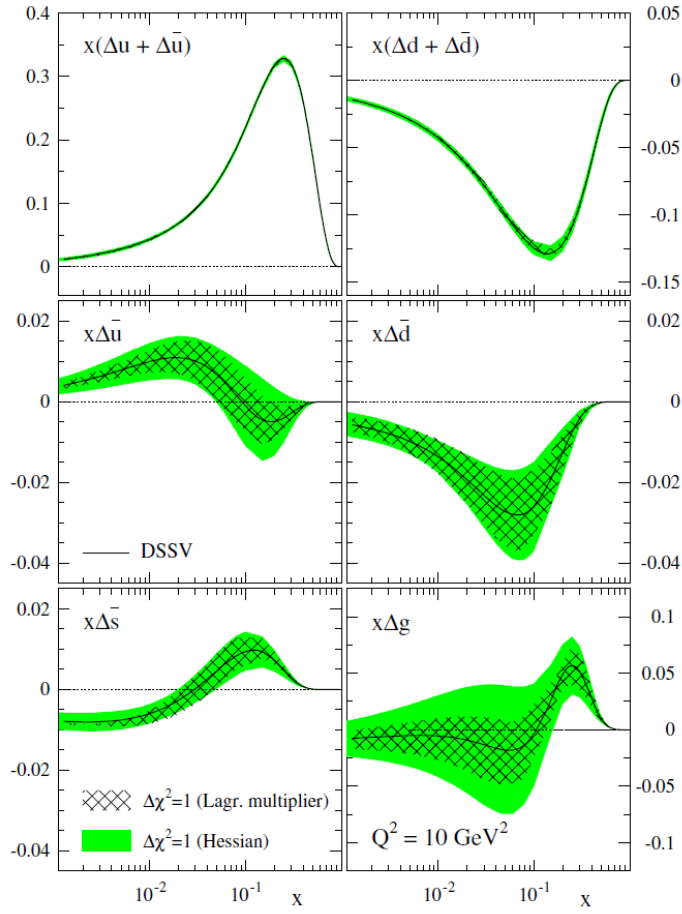


Figure 2.4: The longitudinal PDFs for the quarks and gluons, taken from [29]

DSSV++ global analysis finds  $\Delta G$  to be positive,  $\Delta G = 0.1^{+0.06}_{-0.07}$ . Although positive, the value of  $\Delta G$  (and  $\Delta \bar{q}$ ) may not fully account for the missing spin of the proton in Eq. 1.2, *i.e.* contributions from  $L_{q,g}$  must also be understood.

### 2.2.3 Transverse Proton Structure

The *transversity* PDFs are found by aligning the spin of the proton normal to its momentum. They were first discussed in [30]. The transversity PDFs represent the probability that a quark in a transversely polarized proton with momentum fraction  $x$  carries spin parallel to the proton's spin minus spin anti-parallel to the proton's spin.

$$\delta f(x) = \sum_{q,\bar{q}} \delta q_i(x) \quad (2.10)$$

where  $\delta q$  is defined as

$$\delta q_i(x) = q_i^\uparrow(x) - q_i^\downarrow(x) \quad (2.11)$$

note again that the unpolarized PDFs are simply

$$\delta q_i(x) = q_i^\uparrow(x) + q_i^\downarrow(x) \quad (2.12)$$

Note the absence of gluons in the summation of Eq. 2.10. Transversity is a chiral odd function, such that the partons change sign from initial state to the final. This leads to no gluon transversity distribution, since there is no mechanism to flip the spin-1 gluon.

Hard processes in pQCD conserve chirality, thus chiral odd functions must appear in pairs. Any observable accessing the transversity PDFs must conserve chirality. Transversity can be accessed via the convolution of two transversity PDFs via the transverse double spin asymmetry ( $A_{TT}$ ) [31], or by coupling the transversity with a chiral-odd fragmentation function, which will be discussed in Section 2.3.2.

#### 2.2.4 Transverse Momentum Dependent Proton Structure

Transverse Momentum Dependent (TMD) PDFs are formed by including the non-collinear transverse momentum of the partons ( $k_T$ ) with respect to the momentum of the proton. By considering parton  $k_T$  in addition to the proton and parton spin, eight leading-twist<sup>4</sup> transverse momentum dependent PDFs can be calculated using pQCD

---

<sup>4</sup>leading-twist, also called *Twist-2*, indicates that only the hard scattering of the two partons is considered.

- $f_1(x, k_T)$  unpolarized TMD;
- $g_{1L}(x, k_T)$  helicity TMD;
- $h_{1T}(x, k_T)$  transversity TMD;
- $f_{1T}^\perp(x, k_T)$  Sivers TMD;
- $h_{1T}^\perp(x, k_T)$  Boer-Mulders TMD;
- $g_{1T}^\perp(x, k_T)$  worm-gear TMD, or transversal helicity TMD;
- $h_{1L}^\perp(x, k_T)$  worm-gear TMD, or Kotzinian-Mulders TMD, or longitudinal transversity TMD;
- $h_{1T}^\perp(x, k_T)$  pretzelosity TMD, or quadrupole TMD.

The notation used in the PDFs above is the Jaffe-Ji-Mulders classification, and all TMDs are fully described and discussed in [32, 33]. Distributions indicated by  $f$  represents an unpolarized partons,  $g$  represents longitudinally polarized partons, and  $h$  represents transversely polarized partons. The subscript 1 indicates that it is leading twist, whilst the additional subscripts  $L$  or  $T$  indicate that the proton is polarized longitudinally or transversely, respectively. The superscript  $\perp$  indicates an explicit dependence on  $k_T$ . The TMDs  $f_1(x, k_T)$ ,  $g_{1L}(x, k_T)$ , and  $h_{1T}(x, k_T)$  do not disappear after integration over  $k_T$ , *i.e.* they are simply the collinear distributions  $f_1(x)$ ,  $\Delta f_1(x)$ , and  $\delta f_1(x)$  discussed in the previous three sections, whilst the remaining TMDs disappear upon integration over  $k_T$ . The Sivers and Boer-Mulders TMDs are time-reversal odd, whilst the worm-gear TMDs and the pretzelosity TMD are time-reversal even (T-even). The geometry of each of the eight PDFs are shown in Fig. 2.5.

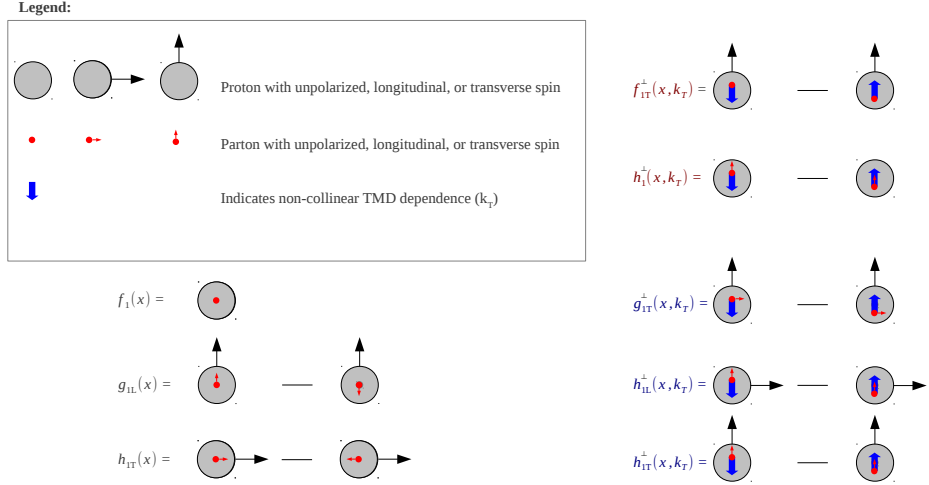


Figure 2.5: The eight leading twist parton distribution functions. The notations in black font represent the three collinear PDFs. The notations in red (blue) font indicate the  $k_T$  dependent PDFs that are T-odd (T-even).

TMDs are important because they could provide insight into angular momentum effects of the proton, although that relationship remains unclear. Many of the properties of TMDs remain a mystery, and they form a vibrant area of research in pQCD. The collinear factorization theorem has not been proven for the non-collinear TMDs, with the exception of the Drell-Yan process [34]. In fact, it has been shown that for hadron-hadron collisions that produce an inclusive hadron, TMD-factorization breaks down due to the entanglement of partons across hadrons [35]. More specifically, it is the breakdown of factorization that leads to the non-zero transverse single spin asymmetries [36] first mentioned in Section 1.1.

The next section expands on the discussion of the Sivers TMD and Transversity (first introduced in Section 2.2.3), as they both may be involved in phenomena related to the measurements of inclusive  $A_N(p + p \rightarrow h + X)$ .

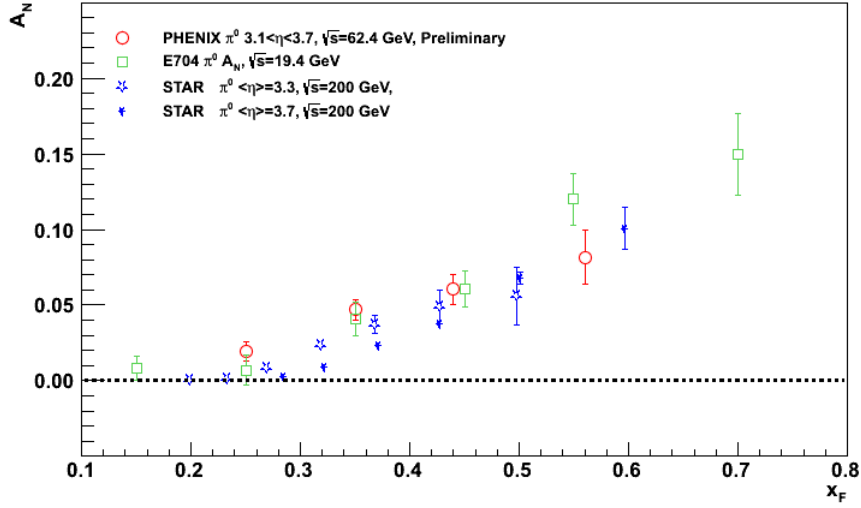


Figure 2.6: Transverse SSAs as a function of  $x_F$  for  $p^\uparrow + p \rightarrow \pi^0 + X$  from experiments E704 [13], PHENIX [43], STAR [42].

### 2.3 Non-Zero $A_N$ Measurements

Transverse single spin asymmetries were initially predicted by pQCD to be small, on the order of  $A_N \sim 10^{-4}$  [37]. Thus, the large non-zero  $A_N$  results first measured as a function of Feynman- $x$  ( $x_F$ , definition in footnote<sup>5</sup>) for pions at forward rapidity were an enigma [38, 39, 40], but they were not completely in  $p + p$  collision energy range ( $\sqrt{s}$ ) of pQCD calculations, *i.e.* they could arise from soft QCD interactions. However, the E704 experiment at Fermilab observed non-zero  $A_N$  measurements for inclusive pion production at forward rapidity at  $\sqrt{s} = 19.2$  GeV [12], well into collision energy range of pQCD. These asymmetries have persisted at forward rapidity at various energies, including measurements made at RHIC by the BRAHMS, STAR, and PHENIX experiments [41, 42, 43]. Results for  $\pi^0 A_N$  as a function of  $x_F$  at various energies from various experiments are shown in Fig. 2.6.

Since the non-zero  $A_N$  results cannot originate from the hard-partonic scatter-

<sup>5</sup>Feynman- $x$  is defined as  $x_F = 2p_z/\sqrt{s}$ , where  $p_z$  is the momentum of the measured inclusive hadron parallel to the beam momentum

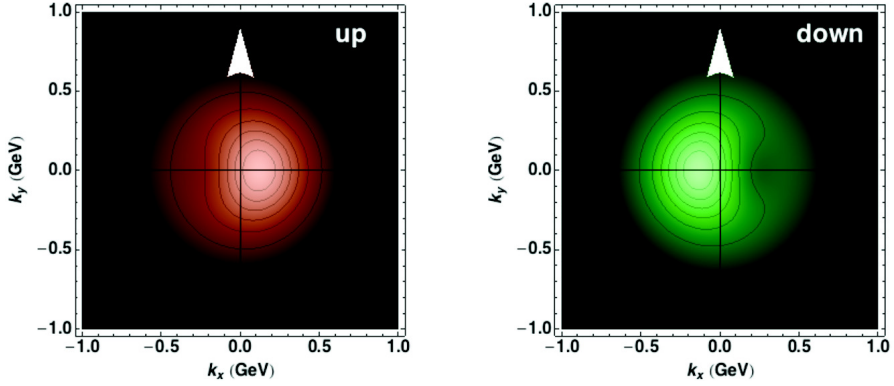


Figure 2.7: The up and down quark density distribution in transverse-momentum-space for the Sivers TMD. The white vertical arrow represents the transverse spin of the proton. Figure by Alessandro Bacchetta [47]

ing, initial and final state interactions are considered. The three possible explanations which have been developed to explain these non-zero asymmetries are outlined below.

### 2.3.1 The Sivers Effect

The Sivers TMD function,  $f_{1T}^\perp(x, k_T)$  [44, 45], introduces an intrinsic parton  $k_T$  in the initial state as a result of the transverse spin of the proton. Naively, these asymmetries can be seen to originate from the orbital angular momentum of the partons. The *Sivers Effect* explains non-zero  $A_N$  observables as a result of an intrinsic  $k_T$  imbalance in the initial state parton correlated with the proton's spin

$$A_N \propto \sum f_{(a)1T}^\perp(x_a, k_{T(a)}) \otimes f_{(b)1}(x_b) \otimes d\hat{\sigma}(x_a, x_b, z_c) \otimes D_c^h(z_c) \quad (2.13)$$

This intrinsic  $k_T$  imbalance is demonstrated in Fig. 2.7, where studies of the Sivers function reveals a density bias in transverse momentum space for the  $u$  quark and  $d$  quarks [46]. This intrinsic  $k_T$  imbalance leads to a bias in the transverse momentum of the hadron produced in the fragmentation of these quarks, which in turn leads to the

non-zero transverse single spin asymmetry.

### 2.3.2 The Collins Effect

As mentioned in Section 2.2.3, the transversity PDF,  $h_{1T}(x)$ , is a chiral odd function, thus to preserve chirality it must couple with another chiral odd function in either the initial or final state. It can preserve chirality by coupling with a chiral odd fragmentation function. Such a function was introduced by John Collins [48].

$$A_N \propto \sum h_{(a)1T}(x_a) \otimes f_{(b)1}(x_b) \otimes d\hat{\sigma}(x_a, x_b, z_c) \otimes H_{(c)1}^{h\perp}(z_c, p_T^h) \quad (2.14)$$

Here  $h_{1T}(x)$  is the transversity PDF first discussed in Section 2.2.3, which couples with the spin dependent *Collins fragmentation function*,  $H_1^{h\perp}(z, p_T^h)$ , in the final state<sup>6</sup>. Due to the initial transverse spin of the quark in the initial state, the  $p_T$  of the leading hadron in the final state Collins fragmentation has a non-zero azimuthal dependency with respect to this initial transverse quark spin of the quark. A global analysis done by Anselmino *et. al.* [49] of the transversity distribution and Collins FF are shown in Fig. 2.8. Since neither transversity nor Collins are non-zero, the Collins Effect is one possible explanation on the origin of non-zero SSAs.

### 2.3.3 Higher-Twist effects

Higher twist effects (twist-3) explain non-zero  $A_N$  results by the interference between a gluon field in the initial or final states within the collinear factorization limit. Qiu and Sterman showed how twist-3 interactions in the initial state affect  $A_N$  [50], and Kanazawa and Koike showed how twist-3 interactions in the final state affect  $A_N$  [51].

---

<sup>6</sup>The Collins function is a TMD fragmentation function, it is dependent on the transverse momentum of the fragmenting parton.

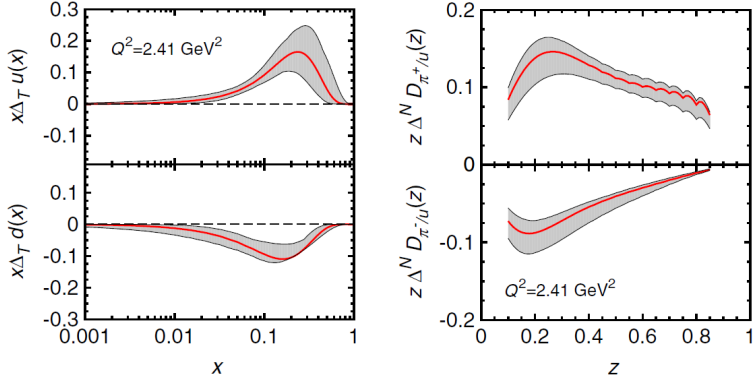


Figure 2.8: Global analysis of the transversity PDF for the valence quarks and Collins FF for charged pions.

A numerical analysis of twist-3 effects of the RHIC  $A_N$  results was recently calculated by Kanazawa and Koike, which explain non-zero RHIC  $A_N$  measurements as a result of a combination of twist-3 effects in the initial and final state, given in the reference [52] as

$$\begin{aligned} \Delta\sigma = & G^{(3)}(x_1, x_2) \otimes f(x') \otimes D(z) \otimes \hat{\sigma}_A \\ & + h(x) \otimes f(x') \otimes \hat{E}^{(3)}(z_1, z_2) \otimes \hat{\sigma}_B \\ & + h(x) \otimes E^{(3)}(x'_1, x'_2) \otimes D(z) \otimes \hat{\sigma}_C \end{aligned} \quad (2.15)$$

Where  $f$ ,  $h$ , and  $D$  represent the twist-2 unpolarized PDF, the transversity PDF, and the unpolarized fragmentation function. The upper index functions represent the twist-3 distributions.  $G$  is the twist-3 distribution of the polarized proton,  $E$  of the unpolarized proton, and  $\hat{E}$  of the final state fragmentation function.

### 2.3.4 Unified Picture

It is possible that non-zero  $A_N$  are explained as a convolution of TMDs and higher twist effects in terms of the partonic momentum transfer  $Q^2$ . This was first

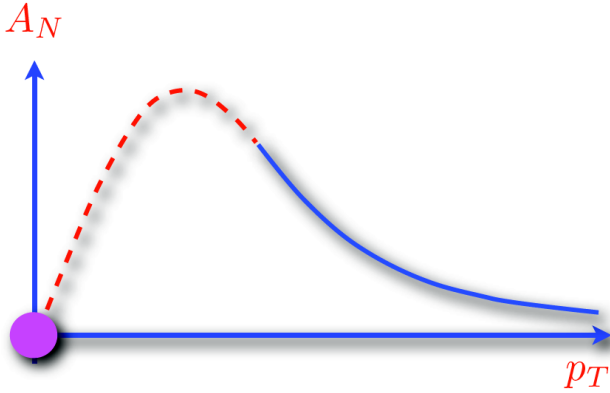


Figure 2.9:  $A_N$  versus  $p_T$ , taken from [55], that demonstrates the convolution of TMD effects with twist-3 effects. The red dashed line represents where the TMD framework dominates. The solid blue line represents where the twist-3 framework dominates

suggested by Ji, Qiu, Vogelsang for the Sivers function, and by Kang and Yuan for the Collins function [53, 54]. In the unified picture, the non-zero  $A_N$  arises from TMD effects at low- $Q^2$ , and from the twist-3 effects at high- $Q^2$ , with some convolution of the two at mid- $Q^2$ .

This convolution effect can be probed by measuring  $A_N$  as a function  $p_T$ , see Fig. 2.9

$$A_N \approx \frac{\alpha}{p_T} - \frac{\alpha'}{p_T^3} + \dots \quad (2.16)$$

Thus, measurements of the  $p_T$  dependence of  $A_N$  can be made to check for convolution effects.

## 2.4 $A_N$ of $\eta$ Mesons

In addition to the pion  $A_N$  measurements mentioned in Section 2.3, the  $\eta$  meson  $A_N$  has been measured by the E704 [56] and STAR [57] experiments. The  $\eta$  meson  $A_N$  results from these two experiments are shown in Fig. 2.10. Kanazawa and Koike predicted that the  $A_N$  of  $\eta$  meson is larger than the  $\pi^0$   $A_N$  due to initial state

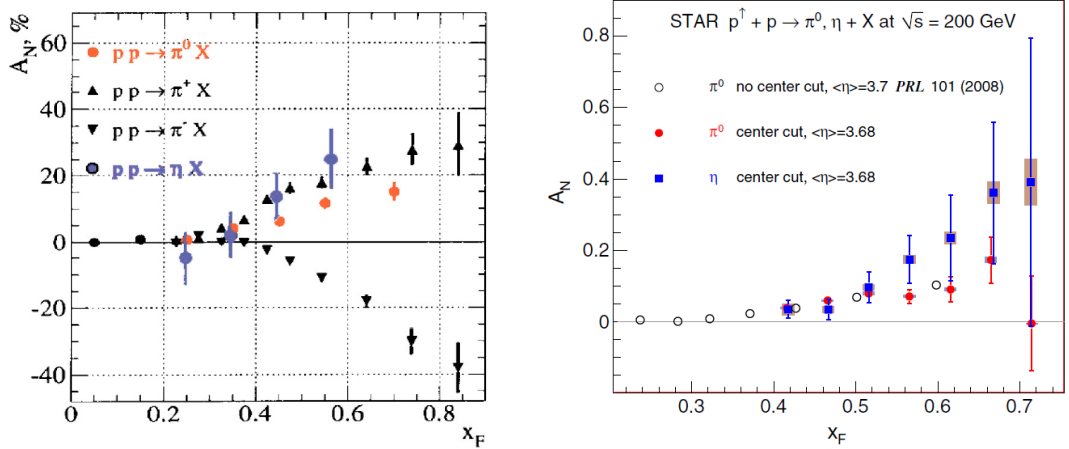


Figure 2.10: The  $\eta$  meson  $A_N$  as seen by the E704 [56] and STAR [57] experiments.

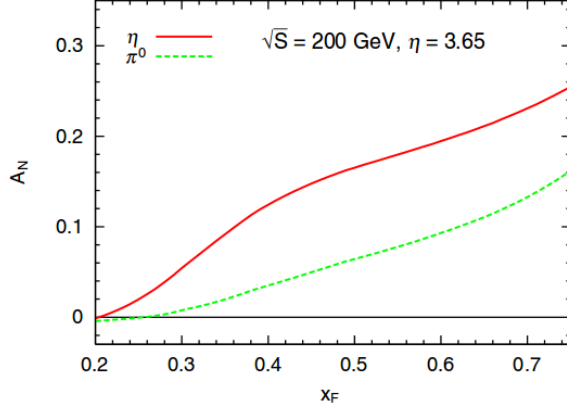


Figure 2.11: The predicted  $\eta$  and  $\pi^0$  meson  $A_N$  from  $p^\uparrow + p \rightarrow h + X$  at  $\sqrt{s} = 200$  GeV at forward pseudo-rapidity ( $\eta = 3.65$ ), calculated by Kanazawa and Koike [58].

twist-3 effects [58] for strange quarks. A prediction for the  $\eta$  meson  $A_N$  at  $\sqrt{s} = 200$  GeV is shown in Fig. 2.11.

The second goal of this Thesis is to measure the transverse single spin asymmetry of  $\eta$  mesons at  $\sqrt{s} = 200$  GeV. Non-zero transverse single spin asymmetries in inelastic proton proton collisions could originate from the Sivers effect, the Collins Effect, higher twist effects, or some convolution of all three. Measurements of the  $\eta$  meson  $A_N$  as a function of  $x_F$  and  $p_T$  and their comparison to the theoretical framework, and

to existing pion and  $\eta$  meson  $A_N$  measurements will help disentangle the origins of these asymmetries, and provide further insight into the structure of the proton.

## Chapter 3

# Experimental Setup

### 3.1 Relativistic Heavy Ion Collider

The Relativistic Heavy Ion Collider (RHIC) is a particle accelerator located at Brookhaven National Laboratory in Upton, New York. The facility culminates with counter-circulating ion beams, each 3.83 kilometers in circumference. For convenience, the clockwise beam is labelled as the blue beam, whilst the counter-clockwise beam is labelled as the yellow beam. Each beam is made up of (at most) 120 bunches of ions, which consist of  $\mathcal{O}(10^{11})$  protons for  $p + p$  collisions. The beams are steered to cross at four different points around the ring, where  $p + p$  interactions occur. Four different experiments have operated at RHIC: PHENIX [59], STAR [60], BRAHMS [61], and PHOBOS [62], where the latter two experiments have concluded their experimental research phases. RHIC is a versatile machine in terms of both the species it collides, as well as the energy of the collision. RHIC is capable of colliding heavy ions ( $A + A$  collisions) at center of mass energies ranging from  $7 < \sqrt{s_{NN}} < 200$  GeV, as well as proton-proton collisions at energies of  $62 < \sqrt{s} < 510$  GeV.

RHIC also has the capability of injecting, accelerating, and colliding polarized

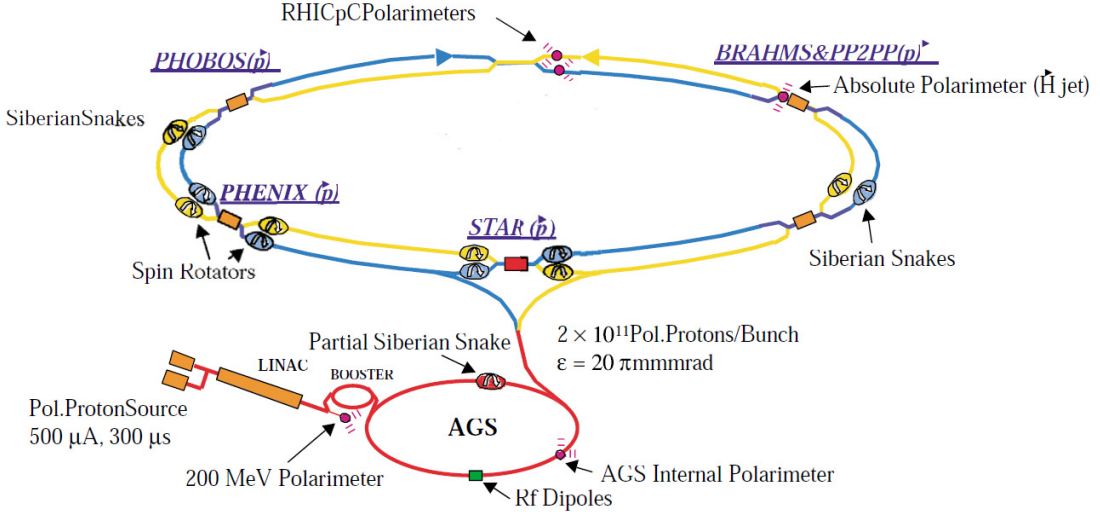


Figure 3.1: The Polarized proton hadron facility at Brookhaven National Laboratory.

proton bunches, a feature which is unique to RHIC. Onward in this Thesis, only the polarized proton aspects of RHIC will be discussed. A schematic of RHIC-AGS complex setup as a polarized proton collider is shown in Fig. 3.1. Information about RHIC as a polarized proton-proton collider is given in [63].

### 3.1.1 Polarized Proton Source

Polarized protons are generated by the optically pumped polarized ion source (OPPIS). The OPPIS produces  $9 \times 10^{11}$  polarized  $H^-$  ion bunches in 300 microsecond long pulses. The  $H^-$  ions are accelerated to 200 MeV in the Linear Accelerator (LINAC), stripped of their electrons, and passed onto the AGS Booster. In the AGS Booster they are further accelerated to a beam energy of 1.5 GeV.

### 3.1.2 RHIC-AGS complex

Proton bunches are next injected into the Alternating Gradient synchrotron (AGS), and are accelerated to 25 GeV. The proton bunches are then transferred to

RHIC. The final stage accelerates the proton bunches to an energy of 100-255 GeV, resulting in a collision energy of  $\sqrt{s} = 200\text{-}510$  GeV.

### 3.1.3 Siberian Snakes

As protons are accelerated in the AGS and RHIC, the spin of a protons in the bunches precesses due to the intrinsic magnetic moment of the proton and due to magnetic fields in the accelerator. This spin precession follows the Thomas-BMT equation.

$$\frac{d\vec{P}}{dt} = - \left( \frac{e}{\gamma m} \right) \left[ G\gamma\vec{B}_\perp + (1+G)\vec{B}_\parallel \right] \times \vec{P} \quad (3.1)$$

Where  $e$  is the proton's electric charge,  $m$  is the mass of the proton,  $G=1.7928$  is the proton's anomalous magnetic moment, and  $\gamma = E/m$ , where  $E$  is the proton's energy.  $\vec{P}$  is the Polarization vector of the proton beam in its rest frame, and  $B_\perp$  and  $B_\parallel$  are the directions of the external magnetic field. Note that at high energies, the  $B_\perp$  term dominates. The revolution of the protons circumventing RHIC is governed by the Lorentz force equation, which describes the orbital motion of a particle in an external magnetic field.

$$\frac{d\vec{v}}{dt} = - \left( \frac{e}{\gamma m} \right) \left[ \vec{B}_\perp \right] \times \vec{v} \quad (3.2)$$

In comparing Eqs. 3.1 and 3.2, for every revolution a proton makes in RHIC, the spin vector of the proton will precess  $G\gamma$  times. The  $G\gamma$  term is referred to as the spin tune,  $v_{sp}$ . The spin tune is vital, because there are certain situations where this can lead to depolarizing resonances of bunch polarization in RHIC. During acceleration (increase in beam energy), depolarizing resonances are encountered when the spin precession fre-

quency equals the frequency of a spin-perturbing magnetic field. Two main types of depolarizing resonances occur: *imperfect* and *intrinsic*. Imperfection resonances occur due to magnet errors and misalignments, while intrinsic resonances are based on magnetic focusing field settings of RHIC<sup>1</sup>

To overcome these depolarization resonances, *Siberian Snakes* [64] were introduced to RHIC, which rotate the polarization direction of the proton beam. As long as the spin rotation from the Siberian Snake is much larger than the spin rotation due to resonance fields, the stable spin direction is unperturbed. A partial snake which rotates the beam polarization by 9° is installed in the AGS, and two 180° snakes are installed in RHIC.

### 3.1.4 Spin Rotator

Four spin rotators are installed in PHENIX (four more also in STAR), one each at the entrance and exit of both beams. The primary purpose of the spin rotators is to rotate the RHIC-default vertical transverse spin direction of the beam by 90° to the horizontal transverse (radial to beam momentum) spin direction or the horizontal longitudinal (parallel with beam momentum) spin direction, as they enter the PHENIX interaction region (IR), and then back to the vertical transverse position as they exit PHENIX.

### 3.1.5 Polarimetry

A key aspect of spin asymmetry measurements is the maximization of the number of ions in the bunches which are polarized in the needed direction. This fraction,

---

<sup>1</sup>Imperfect resonances occur whenever  $v_{sp} = n$ , where  $n$  is an integer. Intrinsic resonances occur when  $v_{sp} = kP \pm v_y$ , where  $k$  is an integer,  $v_y$  is the vertical betatron tune, and  $P$  is the super-periodicity. In the AGS, depolarization resonances are partially suppressed by betatron beam-tuning techniques. At higher energies in RHIC, these techniques become too difficult and tedious. See [63] for full description.

the *polarization*<sup>2</sup>, must be measured to correctly scale any asymmetry measurements. The polarization of the beams in RHIC is determined within a systematic uncertainty  $\Delta P/P \approx (\mathcal{O})5\%$  using two different polarimeters: Proton-Carbon (p-C) polarimeter and the Hydrogen-Jet (H-Jet) polarimeter. In addition, the polarimetry is locally measured by the PHENIX detector as a relative cross check.

### 3.1.5.1 p-C Polarimeter

The p-C polarimeter measures polarization at RHIC by utilizing elastic proton-Carbon scattering in the Coulomb-Nuclear Interference (CNI) region. In each RHIC ring, a thin ribbon of Carbon is placed in the path of the beam, and the asymmetry of recoiled carbon is measured using six silicon detectors

$$P_{beam} = \frac{\epsilon_{pC}}{A_N^{pC}} = \frac{1}{A_N^{pC}} \frac{N_L^C - N_R^C}{N_L^C + N_R^C} \quad (3.3)$$

where  $P_{beam}$  is the beam polarization,  $N_L(N_R)$  are the number of protons scattered to the left and right of vertical beam polarization normalized to luminosity, and  $A_P^{pC} \approx 0.01$  is the  $A_N$  of the  $p^\uparrow + C \rightarrow p + C$  scattering known from measurement and theory. The p-C polarimeter provides a fast and precise polarization measurement of each beam. A full description of the p-C polarimeter can be found in [63].

### 3.1.5.2 H-Jet Polarimeter

The H-Jet polarimeter provides an independent measurement of the polarization and calibrates the p-C polarimeter. When combined with the p-C polarimeter measurement, the uncertainty of  $\Delta P_{beam}/P_{beam}$  is attained to  $(\mathcal{O})5\%$ . The H-jet po-

---

<sup>2</sup>Polarization is defined as the fraction of protons in a bunch with their spins aligned along the polarization vector of the bunch.

larimeter is a free atomic beam, which crosses RHIC in the vertical direction. The polarization of the jet is well known at  $P_{H-jet} > 92 \pm 4\%$ . The asymmetry of the H-Jet target protons scattered elastically  $\epsilon(p^\uparrow + p \rightarrow p + p)$  off of the RHIC proton beam is measured, and vice-versa. Since they are the same process,  $A_N^{target} = A_N^{beam}$

$$A_N = \frac{\epsilon_{target}}{P_{target}} = \frac{\epsilon_{beam}}{P_{beam}} \quad (3.4)$$

which upon rearrangement of the terms gives  $P_{beam}$  as

$$P_{beam} = \frac{\epsilon_{target}}{\epsilon_{beam}} \cdot P_{target} \quad (3.5)$$

Information on the H-Jet hardware and analysis procedure can be found in [65, 66].

### 3.1.6 Luminosity Monitoring and Local Polarimetry, the Zero Degree Calorimeter

A pair of Zero-degree calorimeters (ZDC) are installed at each of the experiments at RHIC. The ZDCs consist of two hadronic calorimeters which primarily measure neutrons. The primary goal of the ZDC is to act as an event trigger and a luminosity monitor [67].

In addition to being a localized luminosity monitor, the ZDC also acts as a local polarimeter for PHENIX. Combined with a shower maximum detector (SMD) in front of the ZDC, the transverse single spin asymmetry of very forward neutron production was found to be non-zero up to 10% [68]. By measuring the neutron transverse asymmetry while taking data, deviations from pure vertical/radial transverse polarization polarization can be detected, see Fig. 3.2.

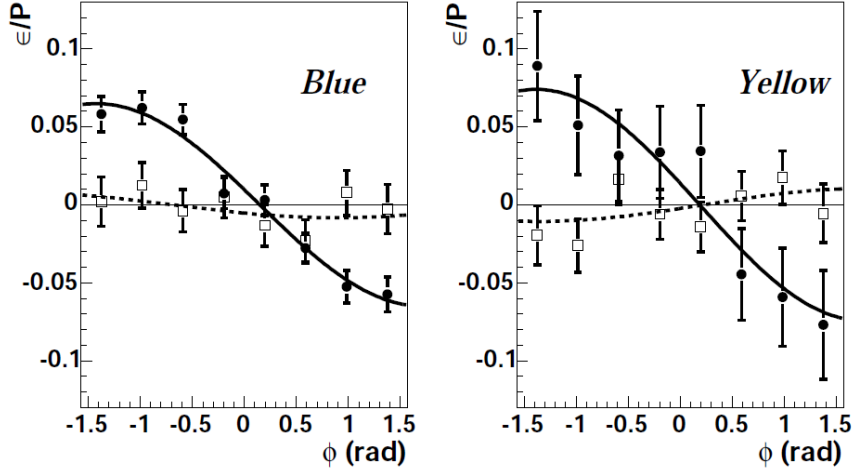


Figure 3.2: The raw asymmetry of the beam polarization,  $\epsilon/P$  as a function of azimuthal angle,  $\phi$  [69]. The open points indicate longitudinal (spin rotator on) beam polarization, whereas the closed points represent transverse (spin rotator off) beam polarization.

### 3.2 The PHENIX Detector

As of the 2008 RHIC  $p + p$  run, The PHENIX detector is one of two currently active detectors at RHIC. For the 2008 RHIC  $p + p$  running, PHENIX (Fig. 3.3) consisted of two Spectrometer arms at central rapidity  $|\eta| < 0.35$ , two Muon arms at rapidity  $1.2 < |\eta| < 2.4$ , two global detectors, and two calorimeters at forward rapidity  $3.1 < |\eta| < 3.9$ . A detailed description of the PHENIX detector is given in [59].

Before proceeding, the lab frame coordinates shall be defined, *i.e.* the PHENIX coordinates. The  $z$  direction is defined parallel to the beam axis, and is positive (negative) in the direction of the blue (yellow) beam, which is North of the interaction point. The  $x, y$  directions are defined perpendicular to the beam axis. Positive (negative)  $x$  is towards geographical West (East), and positive (negative)  $y$  is defined towards the sky (earth). The origin is set at the nominal interaction (IR) point in PHENIX.

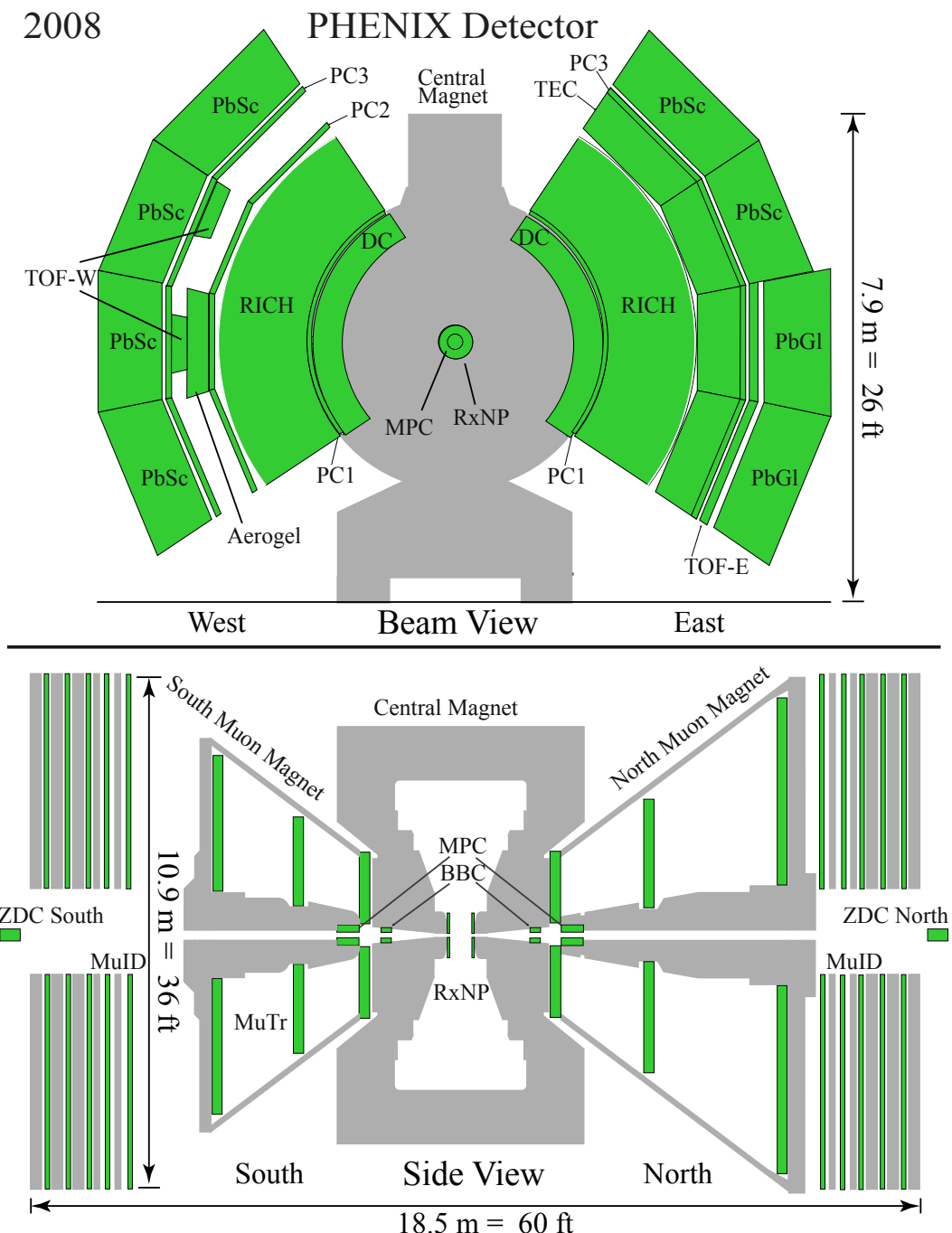


Figure 3.3: The PHENIX Detector setup in 2008.

### 3.2.1 Central Arm Spectrometers

The central arm spectrometers comprise tracking systems for detecting charged particles (electrons, charged pions, kaons, protons) and photons. The magnetic field from the central arm magnets [70] bends charged particles which gives a measure of the particle momentum. The Drift Chambers (DCs) are tracking detectors which provide an estimate of a charged particle's bend. Further from the IR, the Pad Chambers (PCs) provide the three-dimensional position, in coincidence with the DC, which improves on the  $p_z/p_T$  estimate for each track [71]. Behind the tracking detectors lie Ring Imaging Cherenkov Counters (RICH) which separate electrons from charged hadrons. The Time-of-Flight detectors provide identification separation of low mass charged particles (pions, kaons, protons) [72]. The outermost region of the Central arms consists of Electromagnetic Calorimeters (EmCal) which provide energy measurements for tracks which can be used to identify photons and electrons.

### 3.2.2 Muon Arms

The muon arms are designed to measure low to mid momentum muons, with the aim to detect  $J/\psi$  and low mass vector mesons. Similar to the Central Arm, the muon magnets generate a magnetic field which allows trajectory tracking [70]. The Muon Trackers consist of three stations of drift chambers which provide charged tracking, while the Muon Identifiers consist of interleaved steel absorbers and Iarocci style streamer tubes. The Combined Muon Tracker and Muon I.D. detectors allow charged hadron background rejection of  $3 \times 10^{-3}$  [73].

### 3.2.3 Global Detectors

There are two Global Detectors: The Beam-Beam Counters (BBC), and the Zero Degree Calorimeters (ZDC) [74]. The Zero Degree Calorimeters, were discussed in Section 3.1.6. There are two arrays of Cherenkov BBCs in PHENIX, one in the South and one in the North of PHENIX. Each BBC is  $z = \pm 144$  cm from the nominal IR and covers  $3.0 < |\eta| < 3.9$ . They are each composed 64 quartz Cherenkov detectors connected to Photomultiplier tubes (PMTs). The primary function of the BBC is to efficiently measure charged particles, which in turn signal inelastic collisions in the PHENIX IR. In addition, the BBC provides a measure of the position of the collision along the beam axis to a resolution of  $\pm 2$  cm in proton-proton collisions, as well as the start time for TOF measurements.

### 3.2.4 Data Acquisition in PHENIX

An efficient and streamlined triggering system is designed to optimize data taking in PHENIX. For every bunch crossing in RHIC, each PHENIX detector subsystem's signals are processed by their Front End Modules (FEM) and passed to the detector's Front End Electronics (FEE), where the analog and timing signals measured by the detector is converted to digital format by analog-to-digital conversion (ADC) and timing-to-digital conversion (TDC). The FEE receives a signal from the Level-1 Trigger (LVL1) which is preset by the user to determine if an event is interesting for a given subsystem. Upon passing the LVL1 trigger condition, signals from the FEE are sent from the PHENIX IR via fiber optic cables to the PHENIX Control Room where they are passed to the Data Collection Modules (DCM). After Quality assurance and signal reprocessing in DCM, parallel DCM signals are passed to the Sub Event Builder

(SEB) and onto the Assembly and Trigger Processors (ATP). Data passing all the above conditions are then passed to the PHENIX On-line Control System (ONCS), where it is further processed and stored for eventual offline analysis. A full description of the data taking procedure, from the initial processing of signals in the FEM to data storage is outlined in [75] and [76].

### 3.3 A Forward Calorimeter in PHENIX, the MPC Detector

#### **tor**

The forward calorimeters in PHENIX, called the Muon Piston Calorimeter<sup>3</sup> (MPCs) were originally proposed in 1999 [77], and were finally implemented in 2005 [78]. The South MPC was installed and commissioned in 2005/2006 RHIC Run, while the North MPC was installed and commissioned in 2006/2007 RHIC Run. This analysis thus takes advantage of a fully installed and commissioned South and North MPC for the 2008 RHIC run. A complete description of the design, construction, readout, and commissioning of the MPC is given in [79].

The MPC consists of two forward electromagnetic calorimeters, referred to as the South (North) MPC, placed  $\pm 220$  cm from the nominal interaction point, covering a pseudorapidity of  $-3.7 < \eta < -3.1$  ( $3.1 < \eta < 3.9$ ). The South (North) MPC is made up of 196 (220)  $2.2 \times 2.2 \times 18$  cm<sup>3</sup>  $PbWO_4$  crystal towers. A schematic of the MPC is shown in Fig. 3.4. The primary goal of the MPC is to identify  $\pi^0$  and  $\eta$  mesons.

---

<sup>3</sup>The name *Muon Piston* is solely based on the location of the forward calorimeters in PHENIX, and has nothing to do with measuring muons. The MPC reside inside the Muon Pistons magnet return yoke, which move the Muon Arms in and out for maintenance purposes.

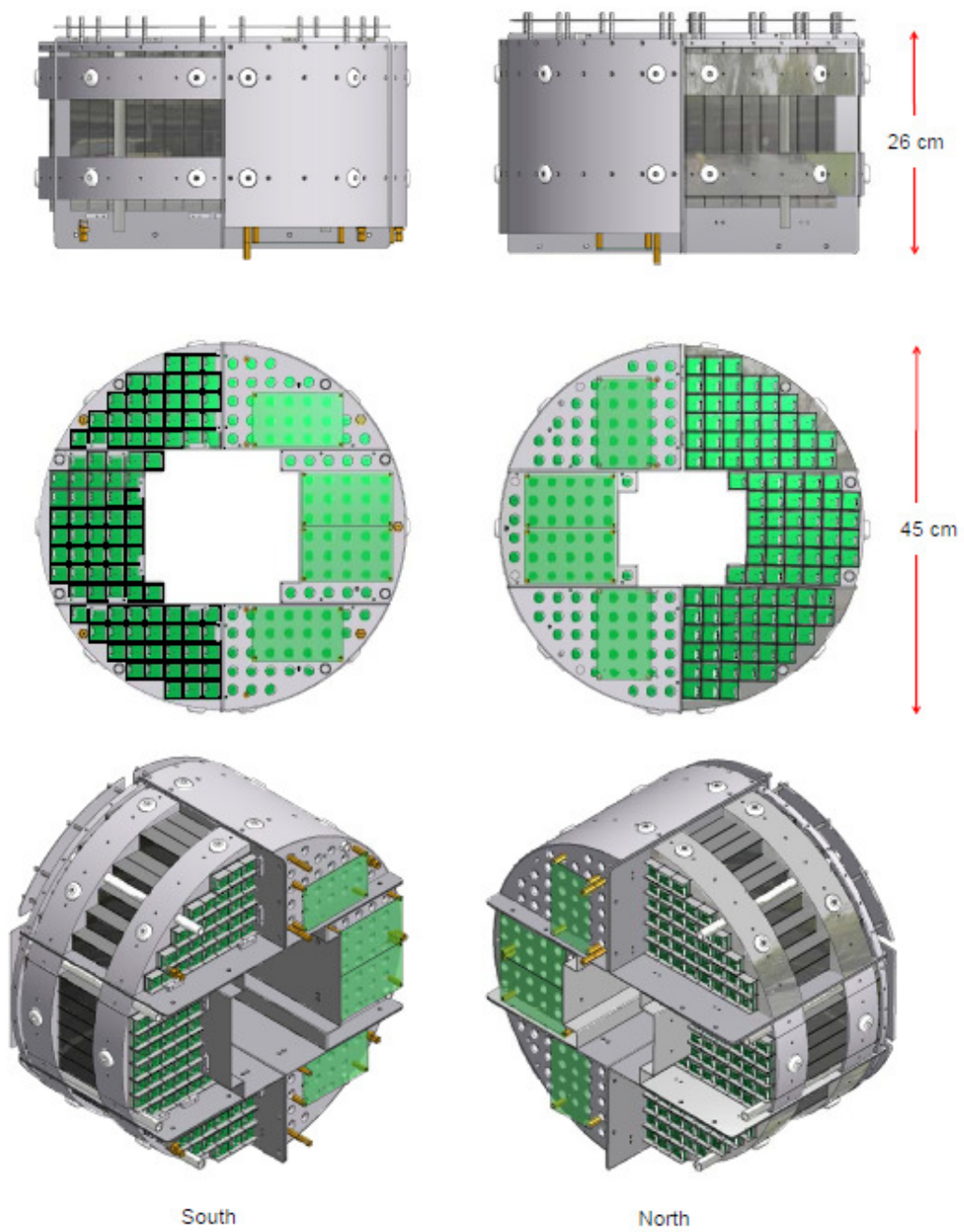


Figure 3.4: A schematic of the South (left) and North (right) MPC. The top panel gives a side view, the middle panel a beam view, and the bottom panel shows the part of the detector facing the collision point.

### 3.3.1 Introduction to Electromagnetic Calorimetry

Electromagnetic Calorimeters are designed primarily to measure the energy of photons and electrons (and positrons). When a high energy photon or electron ( $> 100$  MeV) enters a calorimeter, they *shower* into a plethora of photons, electrons, and positrons via Bremsstrahlung radiation and pair production. The *radiation length*,  $L_{rad}$ , is defined as the longitudinal depth of calorimetric material it takes for a photon to convert into an  $e^+e^-$  via pair production or an electron to emit a photon via Bremsstrahlung, which at high energies is roughly the same for both processes. The depth of the ensuing shower is dependent on the energy,  $E_0$  of the incident photon or electron.

$$L_{depth} = L_{rad} \frac{\ln E_0/E_C}{\ln 2} \quad (3.6)$$

where  $E_C$  is the critical energy, which is the point at which shower development slows drastically. The transverse behaviour of an electromagnetic shower is defined in terms of the *Molière Radius* ( $R_M$ ). Transverse effects are caused by finite opening angles in  $e^+e^-$  via pair production from the incident axis, multiple scattering of electrons, and off axis bremsstrahlung photons.  $R_M$  is defined as

$$R_M = L_{rad} \frac{E_s}{E_c} \quad (3.7)$$

where  $E_s = m_e c^2 \sqrt{4\pi/\alpha}$ .

When designing an electromagnetic calorimeter, the Molière radius  $R_M$  and radiation length  $L_{rad}$  are crucial parameters, and define optimal calorimeter transverse and length, respectively. Primary background sources for an electromagnetic calorime-

MPC Crystal Tower Properties	
Size	$2.2 \times 2.2 \times 18 \text{ cm}^3$
Density	8.28 g/cm <sup>3</sup>
Molière radius	2.0 cm
Radiation Length	0.89 cm
Interaction Length	22.4 cm
Hardness	4 Moh
Refractive index ( $\lambda = 634 \text{ nm}$ )	2.16
Main emission lines	420, 480-520 nm
Temperature Coefficient	-2%/deg C
Radiation Hardness	1000 Gy

Table 3.1: Specifications of the MPC  $PbWO_4$  crystals.

ter come from charged particles (*e.g.* muons, pions, and protons) interacting through ionization losses via the Bethe-Bloch formula, and from hadrons interacting with nuclei to form a hadronic shower. At energies above  $\sim 500$  MeV, however, both backgrounds sources are heavily suppressed. For further discussion of calorimetry, see [80, 81].

### 3.3.2 MPC Specifications

Due to the location of the MPC in relation to the IR and due to tight space constraints in the Muon Pistons arms, the ideal calorimetric material used for the MPC must have a short radiation length and small Molière radius. The material chosen was lead-tungstate scintillating crystals ( $PbWO_4$ ), which were originally developed and extensively tested for the use in the ALICE and CMS experiments at CERN [82]. The properties the  $PbWO_4$  crystals are given in Table 3.1.

Scintillation light produced from the showers in an MPC  $PbWO_4$  crystal is measured by an avalanche photodiode (APD) and preamplifier combination attached to the end of each the MPC crystal. The crystal/APD combination is defined as an MPC tower. Figure 3.5 shows a  $PbWO_4$  crystal tower and the APC preamp.

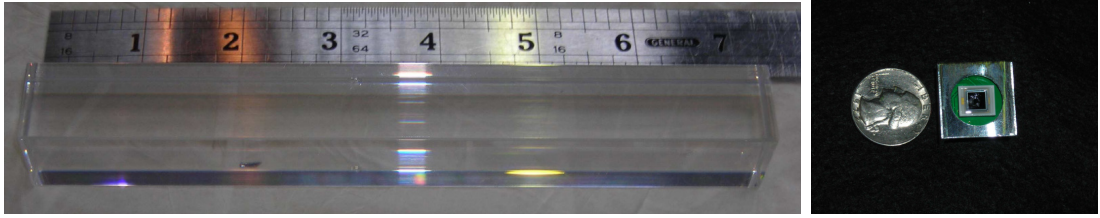


Figure 3.5: A  $PbWO_4$  crystal tower (left panel) and an APD preamp attached to the front of a crystal (right panel).

Driver Boards attached to the end of the MPC supply power and readout APD/preamps for up to 24 towers. Signals from the Driver Boards are passed on to Receiver Boards, which forces the signals to imitate those in the Central Arm EmCal. Signals from the Receiver Boards are then passed on the MPCs FEEs, which are exact replicas of the EmCal FEEs, hence the reason for the receiver boards. MPC FEE data then follows the procedure outlined in Section 3.2.4.

### 3.3.3 ADC to energy conversion in the MPC

As mentioned in section 3.2.4, signals measured in PHENIX are converted to ADC values and sent to PHENIX. In the MPC, tower energies are obtained from the ADC value by

$$E_{tow} = ADC_{tow} * G_{tow} * R_{tow}(t) \quad (3.8)$$

where  $G \approx 0.0162$  is the *absolute gain* of the MPC, and  $R(t)$  is the *relative gain*, which changes in the MPC as RHIC operations progresses. The relative gain is needed due to temperature fluctuations during RHIC running, and for radiation damage which accrues as RHIC running progresses. The relative gain is set using a real time fast LED monitoring system [79].

## Chapter 4

# Measurement of the Invariant Cross Section

The cross section is measured using the 2008 RHIC dataset of  $p + p$  collisions at  $\sqrt{s} = 200$  GeV. To measure the cross section of any reaction ( $p + p \rightarrow h + X$ ) which produces a particle “ $h$ ”, two quantities need to be measured: the sample injected Luminosity and the number times particle  $h$  is found

$$\sigma_h = \frac{N_h}{\mathcal{L}_{pp,inel}} \quad (4.1)$$

From this, the invariant cross section can be defined. The invariant cross section relates the cross section at a given  $p_T$  with the number of particles,  $N_h$ , in a given phase space

$$\sigma_{inv} = E \frac{d^3\sigma_h}{dp^3} = \frac{1}{\mathcal{L}_{pp,inel}} \frac{1}{2\pi p_T} \frac{d^2N_h}{dp_T d\eta}. \quad (4.2)$$

The cross section is measured using a minimally biased data sample (called the Minimum Bias trigger), which records data when at least one BBC PMT on each array

records a signal. Additionally, the collision vertex is required to be within  $\pm 30$  cm of the nominal IR.

As the number of collisions delivered by RHIC exceeds the data-taking rate of the PHENIX data acquisition system, only a fraction of events can be recorded as “minimum bias.” To enhance the more rare (higher momentum)  $\eta$  mesons in the data stream a second trigger is used to measure the high- $p_T$  part of the cross-section with higher statistical significance. This higher momentum trigger (called the  $4\times 4$ B trigger) records an event when any  $4\times 4$  array of MPC towers satisfies an energy threshold of  $E > 20$  GeV.

From 47 RHIC machine *fills*<sup>1</sup> classified as physics, a total of 266 (254) Minimum Bias ( $4\times 4$ B) PHENIX *runs*<sup>2</sup> were taken. Combined, these triggers sampled  $\mathcal{L} = 3.87 \text{ pb}^{-1}$ . The Minimum Bias triggered dataset essentially measures the cross section from  $0.5 < p_T < 4.0$  GeV/ $c$  whereas the  $4\times 4$ B triggered data extends this to  $\sim 5.5$  GeV/ $c$ .

## 4.1 Quality Assurance

### 4.1.1 MPC Warnmap

The first quality assurance study eliminates faulty towers in the MPC, producing a *warnmap*, which is used to mask channels which do not operate optimally. The full warnmap study used in this analysis is documented in [83]. There are two significant pieces of the North MPC which are flagged as non-optimal. First, there is a beam pipe support stand (see Fig. 4.3), which is situated directly in front of the North MPC which

---

<sup>1</sup>A RHIC *fill* is defined as when RHIC has ions in both beams. An optimal RHIC fill lasts eight hours, but may be shorter or longer depending on circumstances

<sup>2</sup>A PHENIX *run* is defined as when PHENIX is fully online taking data from all subsystems. Several runs occur during a RHIC fill. An optimal PHENIX run lasts one hour, but may be shorter due to various circumstances.

shadows 14 towers at low-rapidity. These are not used in this analysis. In addition, a noisy driver board which caused issues for low energy thresholds ( $< 1$  GeV) on the right side of the North MPC. The noisy driver board towers are not used for the cross section analysis. The warnmap used for the Minimum Bias triggered dataset is shown in Fig. 4.1. The warnmap for the  $4 \times 4B$  triggered dataset is shown in Fig. 4.2.

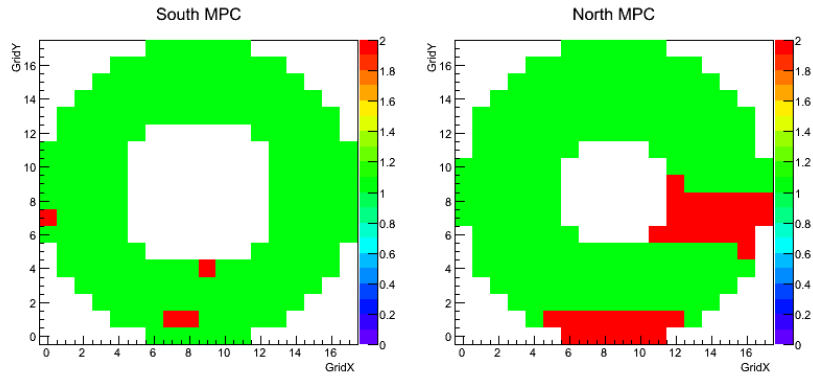


Figure 4.1: Warnmap used for Minimum Bias triggered dataset. The left (right) panel shows the South (North) MPC warnmap. Clusters which have their primary tower position in red are removed from the analysis.

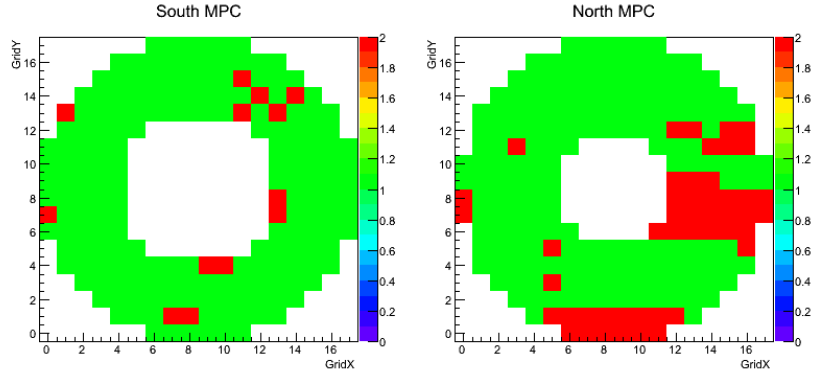


Figure 4.2: Warnmap used for  $4 \times 4B$  triggered dataset. The left (right) panel shows the South (North) MPC warnmap. Clusters which have their primary tower position in red are not used in this analysis.



Figure 4.3: The north MPC, with the v-shaped beam pipe stand directly in front of it.

#### 4.1.2 Run Quality Assurance

The PHENIX data are divided into *runs* separating periods of down time of the RHIC accelerator, and also breaks for calibrations and changes to the trigger configurations. For this analysis each run must pass certain Quality Assurance (QA) criteria in order to be used in the cross section measurement. The first check is to make sure the MPC was operational during a given run. For four runs, the high voltage of the MPC was not activated.

The next test is to check the  $\eta$  meson yield per event (Fig. 4.4), the peak position (Fig. 4.5), and the peak width (Fig. 4.6) for deviations from the mean value. For each panel, a constant line is fit to the run-by-run data points with and LTS<sup>3</sup> regression of 0.7, and calculate a standard deviation. This is done separately for the South and North MPC, as well as for the Minimum Bias and 4×4B triggered datasets. For the Minimum Bias data Run QA,  $\pi^0$  mesons are used instead of  $\eta$  mesons because there are not enough  $\eta$  mesons to extract a reliable signal. Runs that are more than  $2\sigma$  from the average are removed from this analysis. Only one run is removed from the Minimum Bias triggered dataset, and eight runs are removed from the 4×4B triggered

---

<sup>3</sup>Least trimmed squares (LTS) is a statistical method that fits a function to a set of data whilst rejecting a certain amount of outliers. For an example, if the LTS regression is set to 0.9, then 10% of data points will be ignored in the fit.

dataset. Figure 4.4 demonstrates why Run quality assurance is important. The bottom two plots in Fig. 4.4 give a lower yield per event during the first 40 or so runs because of different gain settings in the MPC, which is accounted for in the final calibrations.

Out of the original 266 (254) PHENIX runs recorded, a total of 261 (246) PHENIX runs are used for the Minimum Bias ( $4 \times 4B$ ) cross section measurement.

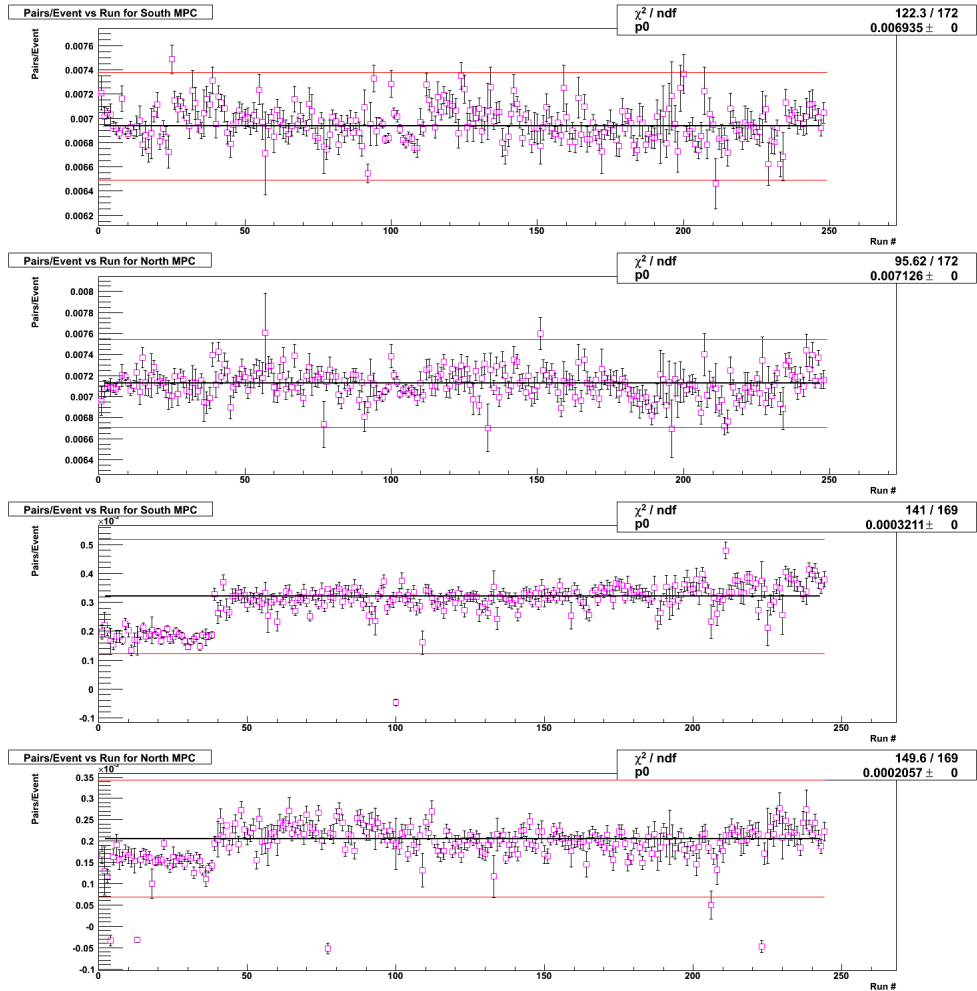


Figure 4.4: The raw yield of  $\pi^0(\eta)$  per event in Minimum Bias (top pair) and  $4 \times 4B$  (bottom pair) data sample. The top (bottom) figure in each pair represents the South (North) MPC.

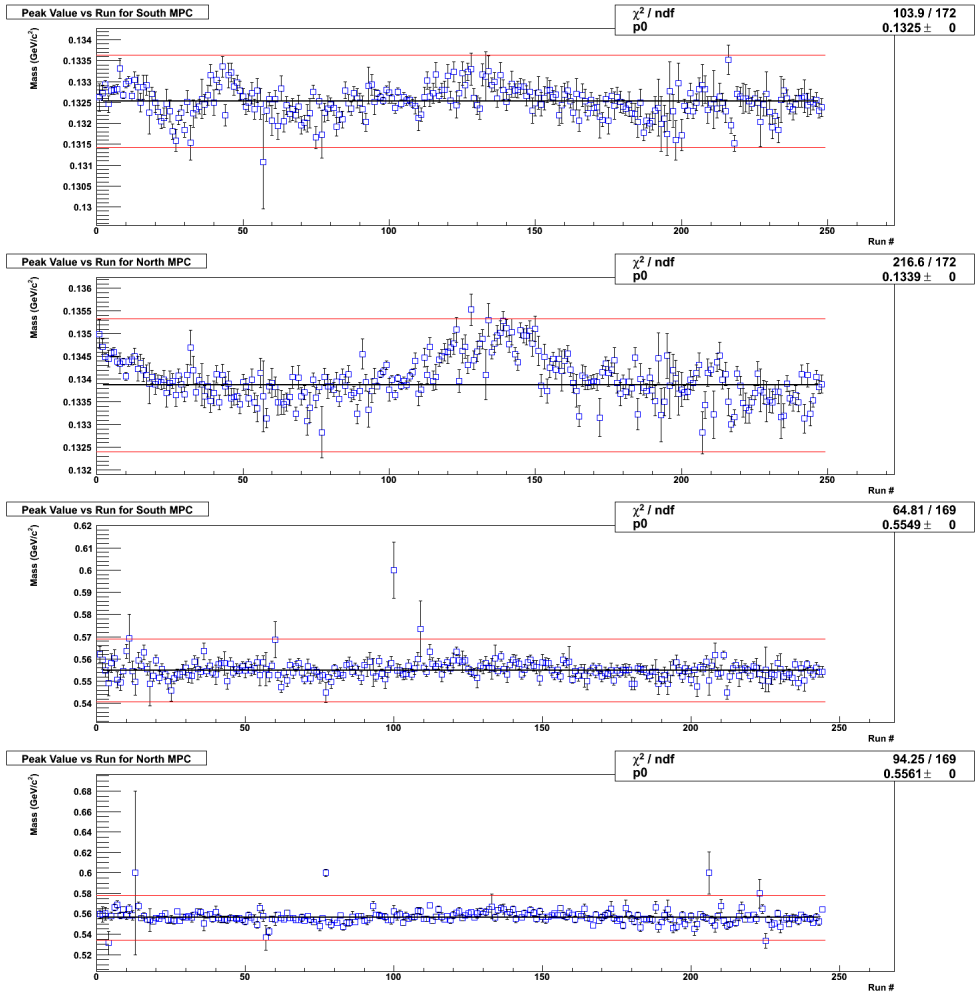


Figure 4.5: The measured di- $\gamma$  invariant mass peak position in Minimum Bias (top pair) and 4x4B (bottom pair) data sample. The top (bottom) figure in each pair represents the South (North) MPC.

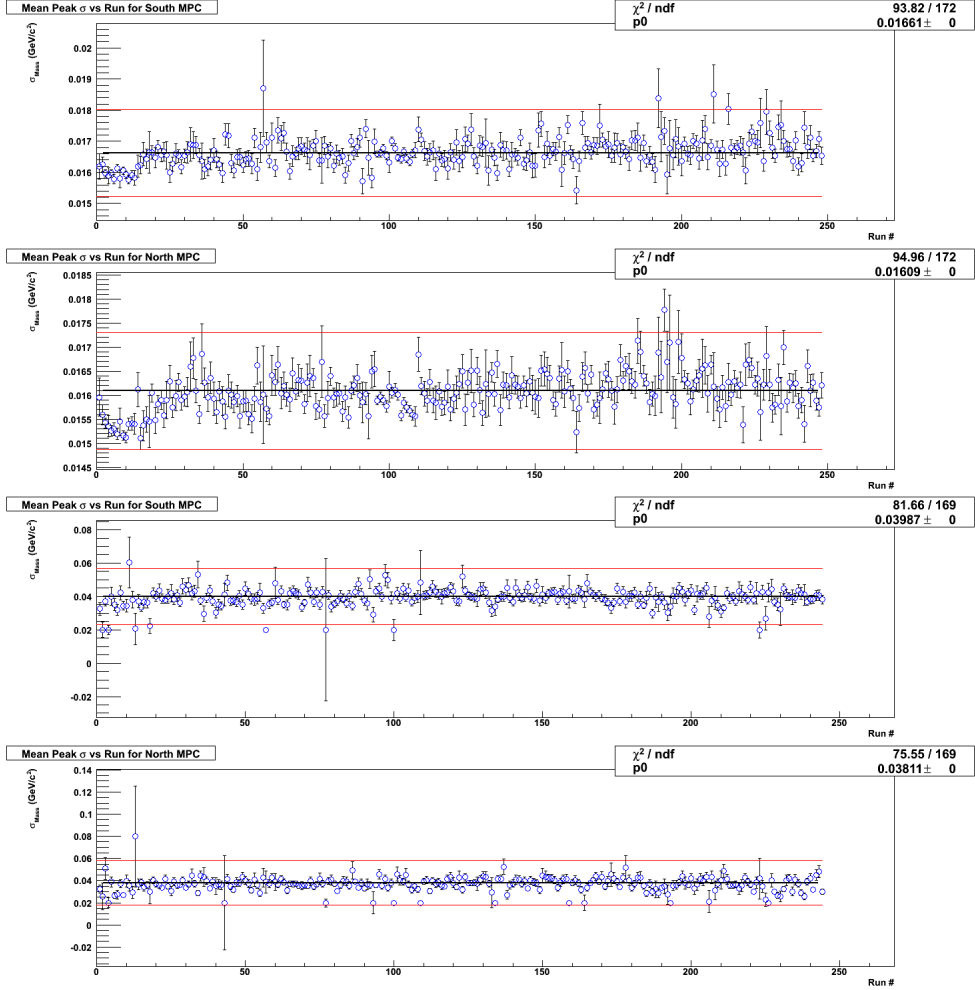


Figure 4.6: The measured di- $\gamma$  invariant mass peak width in the Minimum Bias (top pair for  $\pi^0$  meson) and 4×4B (bottom pair for  $\eta$  meson) data sample. The top (bottom) figure in each pair represents the South (North) MPC. Note: Top (bottom) pair measures  $\pi^0$  ( $\eta$ ) meson width.

## 4.2 Event Selection Criteria

The BBC was used to determine the  $p + p$  collision point along the beams ( $z$ -vertex). A  $z$ -vertex cut of  $-30 < z < 30$  cm cut about the nominal IR is made in both the Minimum Bias and 4×4B triggered dataset. This cut keeps 85% of all recorded Minimum Bias events, and 43% of all recorded 4×4B events.

### 4.3 Identification of $\eta$ Mesons

The MPC identifies  $\eta$  mesons via the decay channel  $\eta \rightarrow \gamma\gamma$ , which has a branching ratio of 0.3942. The other main decay channels:  $\eta \rightarrow 3\pi^0$  and  $\eta \rightarrow \pi^+\pi^-\pi^0$  are not used in this analysis [84], as their acceptance in the MPC is very small, limiting their statistical significance.

In order to reconstruct an  $\eta$  meson in the MPC both decay photons must deposit all of their energy in the MPC towers. Individual photons in the MPC cannot be identified directly, as other types of particles (hadrons or electrons) may also impinge the detector and masquerade as a photon. All possible photon candidates are identified as *clusters*, which are combinations of correlated  $3\times 3$  towers which have a total energy above a certain threshold. To optimize the likelihood that the clusters are real photon sources and to eliminate background sources, several quality assurance cuts are made on clusters. The following cuts are made on single clusters

- Cluster energy cut of  $E_{cl} > 2$  GeV (6 GeV) in the Minimum Bias ( $4\times 4B$ ) trigger.
- Cluster quality:  $\chi^2_{core} < 2.5$  and  $disp_X, disp_Y < 4.0$ .

These cuts maximize the likelihood that the cluster candidate is from a photon.

Further discussion and optimization of these cuts can be found in [83].  $\chi^2_{core}$  is a  $\chi^2/NDF$  variable that compares the measured shower-shape with that predicted.  $disp_X, disp_Y$  are based on the lateral dispersion of the shower in the  $x$  and  $y$  directions.

- Fiducial cut of  $11 < r < 19$  cm, where  $r = 0$  cm is the center of the beam pipe.

This eliminates leakage of energies at the edges of the MPC.

- Central tower energy cut:  $E_8/E_{cent} < 0.14$  and  $disp_X, disp_Y > 0.5$

$E_{cent}$  represent the central tower energy in the  $3 \times 3$  towers making up a cluster, and  $E_8$  represents the energy of the surrounding eight towers. The purpose of these cuts is to eliminate single tower spallation neutron background.

- ADC and TDC overflow cuts (see Section 3.2.4 and 3.3.3) [85].

The ADC overflow cut eliminates high energy particles that are beyond the energy kinematic readout of the MPC detector. The TDC overflow cut eliminates residual contamination that occurs from previous event crossings.

Once the cluster sample is reduced to an enhanced sample of real photons, clusters are paired together to form an invariant mass

$$M_{\gamma\gamma} = 4 \cdot E_{cl1} \cdot E_{cl2} \cdot \sin(\alpha_{12}/2) \quad (4.3)$$

where  $E_{cl1,cl2}$  are the measured energies of each cluster, and  $\alpha_{12}$  is the opening angle between the momentum vectors of the two clusters. Additional kinematic cuts are made on paired clusters to enhance the number pairs that originate from  $\eta$  mesons, and minimize combinatorial background contamination. The following cuts are made on cluster pairs

- A pair energy cut  $7 < E_{pair} < 70$  GeV ( $10 < E_{pair} < 100$  GeV) in the Minimum Bias ( $4 \times 4$ B) triggered dataset.
- Minimum cluster separation cut,  $\Delta R < 2.6$  cm, which prohibits clusters from overlapping.
- Energy asymmetry cut of  $\alpha < 0.8$ , where

$$\alpha = \left| \frac{E_1 - E_2}{E_1 + E_2} \right| \quad (4.4)$$

- For the  $4 \times 4$ B trigger at least one of the two clusters must be  $E_{cl1,cl2} > 20$  GeV.

This is the threshold of the  $4 \times 4$  tiles in the  $4 \times 4$ B trigger, so at least one cluster must be above this threshold.

After these cuts are applied, invariant mass pairs are formed, which are demonstrated by the blue points in Fig. 4.7. A clear  $\eta$  meson peak can be seen at  $M_{ClCl} \approx 0.547$  GeV/ $c^2$ .

### 4.3.1 Combinatorial Background Subtraction

After purifying the sample to all photon pairs, the remaining pairs are classified in two categories: *real* pairs and *uncorrelated* combinatorial pairs. Real pairs originating from  $\eta \rightarrow \gamma\gamma$  should form a pair-mass which is close to that of the  $\eta$  meson. Combinations (for example using a photon from the wrong  $\eta$  or  $\pi^0$  decay or from a misidentified charged hadron) form an uncorrelated combinatorial background, unrelated to the  $\eta$  mass. Figure 4.7 illustrates this scenario. Event-by-event, pairs are indistinguishable (blue curves) and have to be statistically separated. To account for the combinatorial background, photon candidates are analyzed from different events (necessarily breaking all real combinations) to form a mixed event distribution (red curves in Fig. 4.7). Subtracting real event and mixed event pairs results in a final  $\eta$  mass peak which has all uncorrelated background removed (black curves in Fig. 4.7). Any residual background that is still present after mixed-event subtraction is called *correlated* background.

For this analysis, a mixed-event subtraction is used to procure  $\eta$  meson yields from the Minimum Bias triggered dataset. Since mixed-event only removes a small fraction of the uncorrelated background in the  $4 \times 4$ B triggered dataset, this technique is not used in this case (Fig. 4.7, right panel).

Subtraction of the correlated background is explained in the next section. Fur-

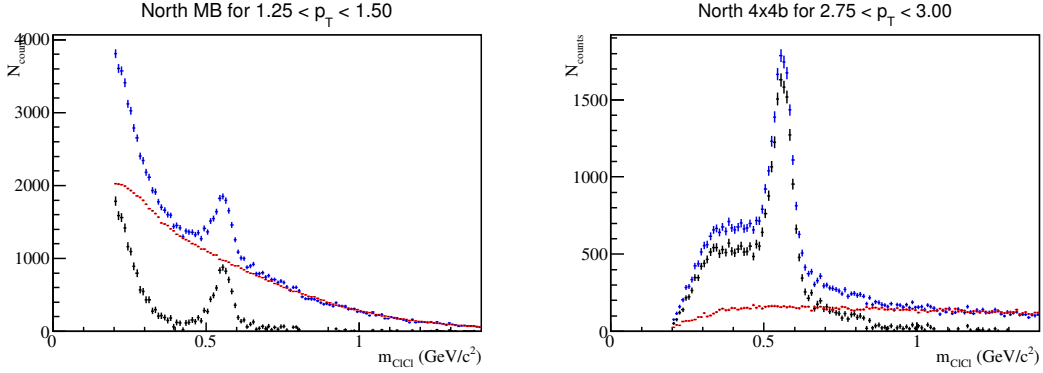


Figure 4.7: Demonstration of  $\eta$  meson signal extraction in the North MPC as a function of invariant mass from the Minimum Bias ( $4 \times 4B$ ) triggered dataset, shown in the left (right) panel. The signal (black) is extracted by taking the difference between the real event pairs (blue) and mixed event pairs (red), which represents the removal of the uncorrelated combinatorial background.

ther explanation of correlated background sources, as well as a study of correlated background in the  $4 \times 4B$  triggered dataset will be given in 5.5.2.

### 4.3.2 Yield extraction

The mixed event subtracted yields for the Minimum Bias triggered dataset are fit with an exponential background function plus a normalized Gaussian for the signal peak

$$F(x) = ae^{-bx} + \frac{N}{\sigma\sqrt{2\pi}}e^{-\frac{1}{2}\left(\frac{x-M}{\sigma}\right)^2} \quad (4.5)$$

where  $a$ ,  $b$  are fit parameters for the background exponential function,  $N$  is the raw yield of  $\eta$  mesons, and  $M$  and  $\sigma$  is the mass value and width, respectively of the  $\eta$  meson peak. The fits to the invariant mass distributions for the Minimum Bias triggered data are shown in Figs. 4.9 (South) and 4.10 (North). For  $p_T$  bins below 2.75 GeV/ $c$ , a mixed event subtraction is applied. Above 2.75 GeV/ $c$ , no mixed event subtraction is used since the background levels are too low.

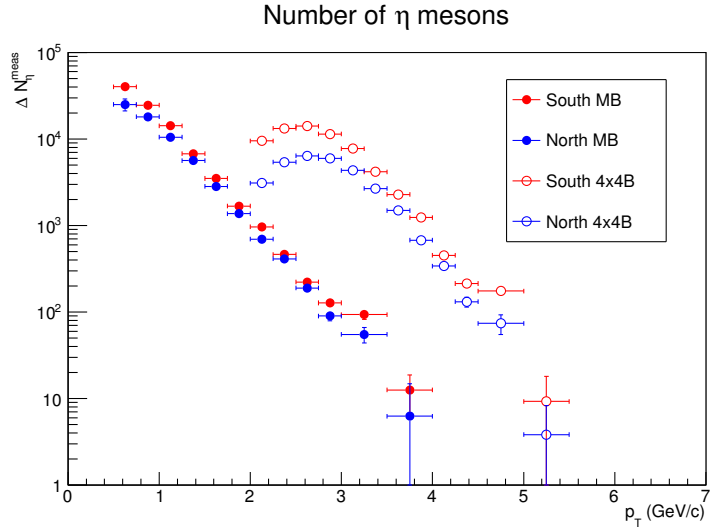


Figure 4.8: Measured spectra as a function of  $p_T$ .

To extract the yields for the  $4 \times 4B$  triggered data, the background is fit with a Gamma Distribution Function and the signal peak with a normalized Gaussian

$$F(x) = F(x, a, \gamma, \mu, \beta) + \frac{N}{\sigma \sqrt{2\pi}} e^{-\frac{1}{2}(\frac{x-M}{\sigma})^2} \quad (4.6)$$

where  $a$ ,  $\gamma$ ,  $\mu$ , and  $\beta$  are fit parameters for the background Gamma Distribution Function,  $N$  is the raw yield of  $\eta$  mesons, and  $M$  and  $\sigma$  is the mass value and width, respectively of the  $\eta$  meson peak. The fits to the invariant mass distributions for the  $4 \times 4B$  triggered data are shown in Figs. 4.11 (South) and 4.12 (North).

The raw  $\eta$  meson spectra are shown in Fig. 4.8. The functional form of Eqs. 4.5 and 4.6 are varied to estimate the systematic effect of the fit functions on the yield extraction, which is discussed in section 4.6. From Fig. 4.8, the advantage of having two triggers is made clear. The Minimum Bias ( $4 \times 4B$ ) triggered dataset extracts  $\eta$  mesons in the range of  $0.5 < p_T < 4.0$  GeV/c ( $2.0 < p_T < 5.5$  GeV/c).

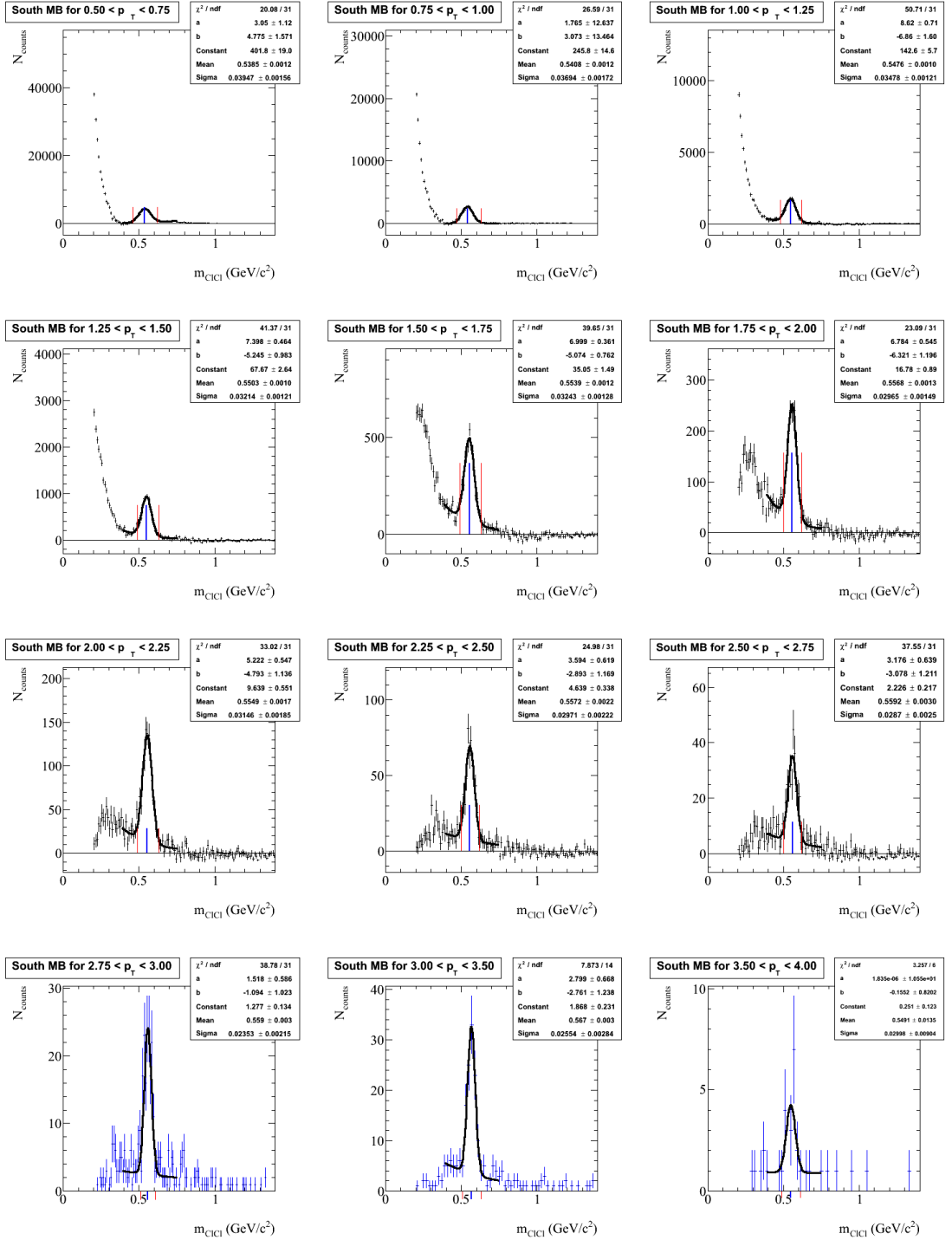


Figure 4.9: The invariant mass distributions in the South MPC for the Minimum Bias triggered dataset, binned in  $p_T$ . The correlated background + signal is fitted with Eq. 4.5. The last three bins,  $2.75 < p_T < 4.0$   $\text{GeV}/c$  do not have a mixed event subtraction.

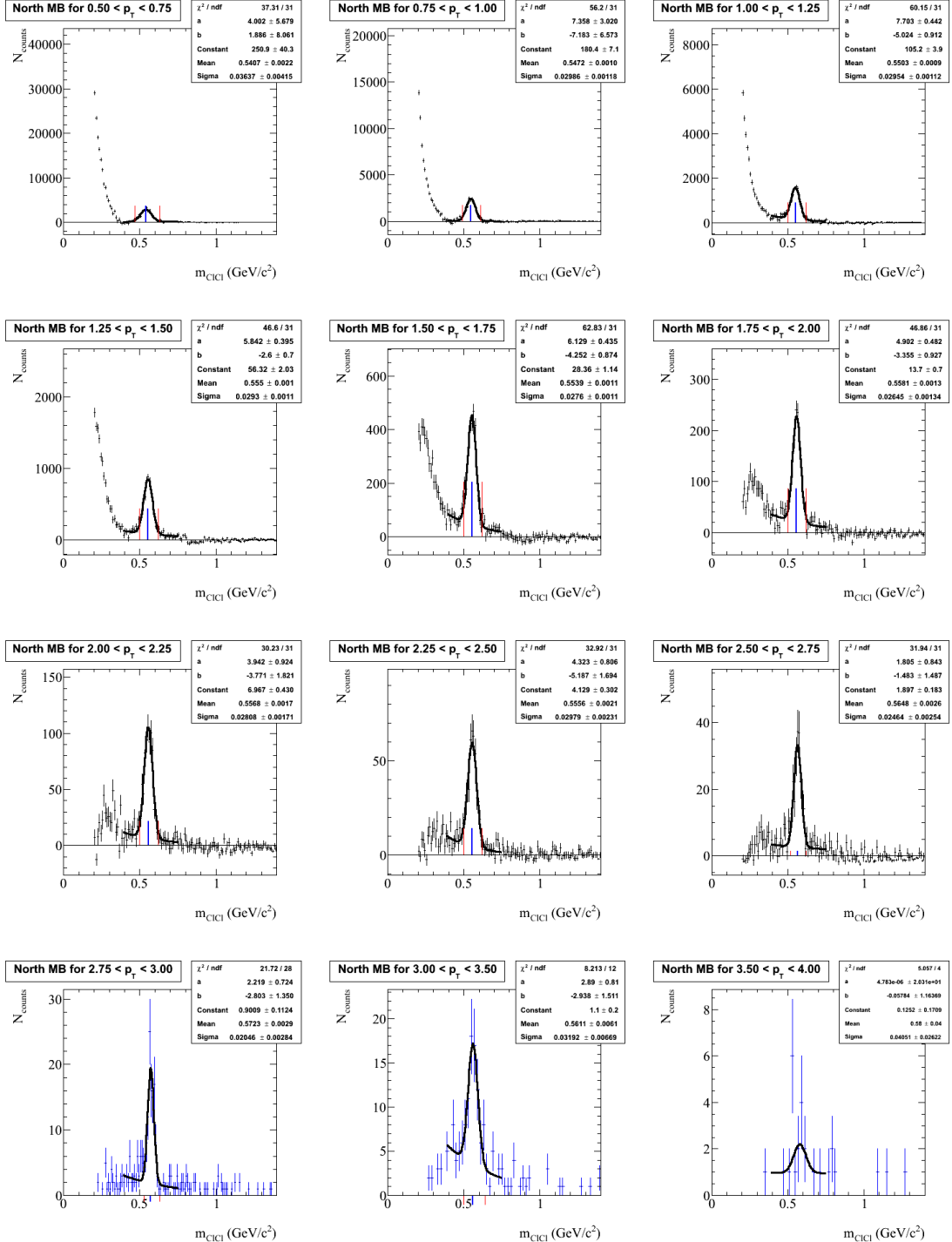


Figure 4.10: The invariant mass distributions in the North MPC for the Minimum Bias triggered dataset, binned in  $p_T$ . The correlated background + signal is fitted with Eq.4.5. The last three bins,  $2.75 < p_T < 4.0$  GeV/ $c$ , do not have a mixed event subtraction.

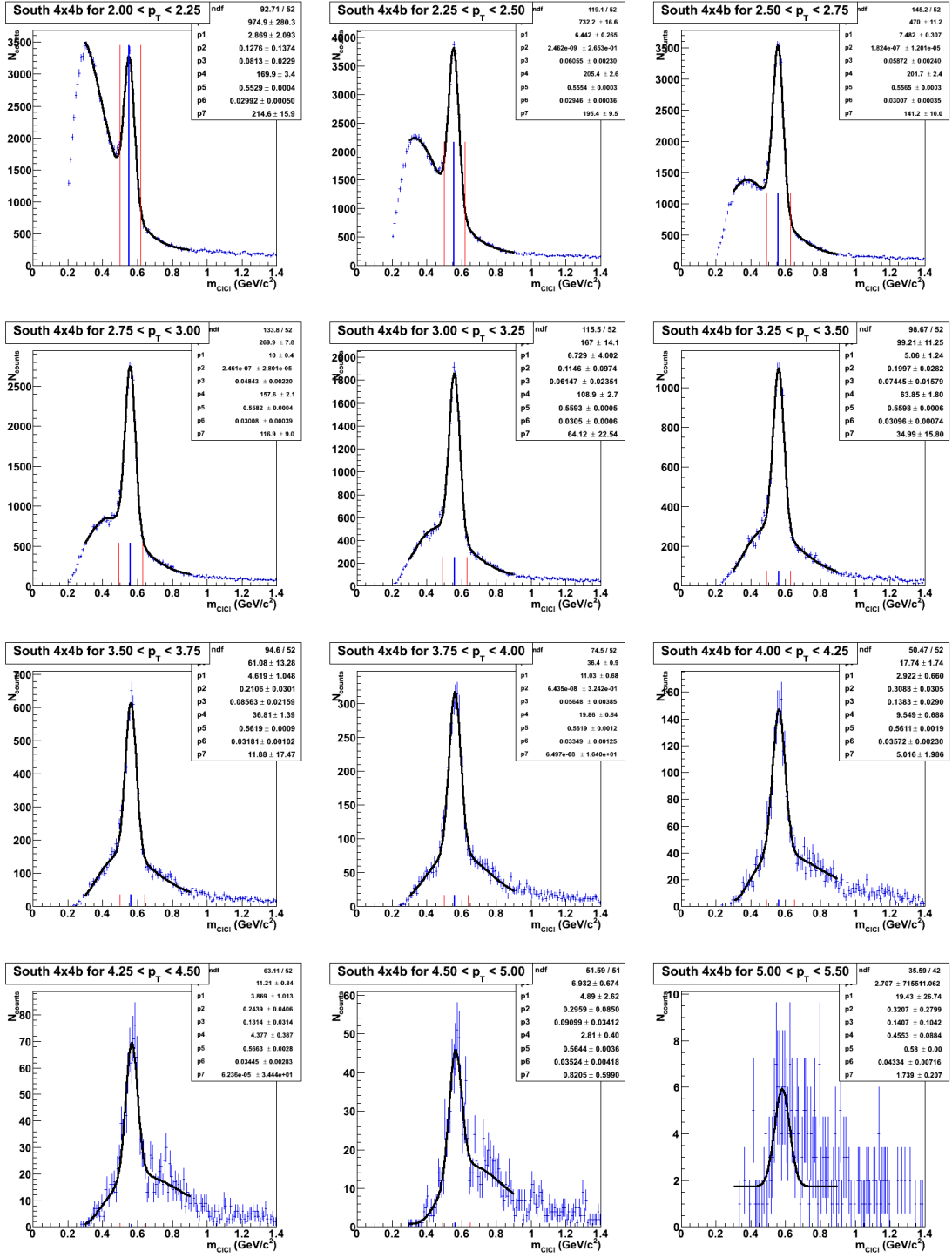


Figure 4.11: The Invariant Mass distributions in the South MPC for the  $4 \times 4B$  triggered dataset, binned in  $p_T$ . The correlated background + signal is fitted with Eq. 4.6.

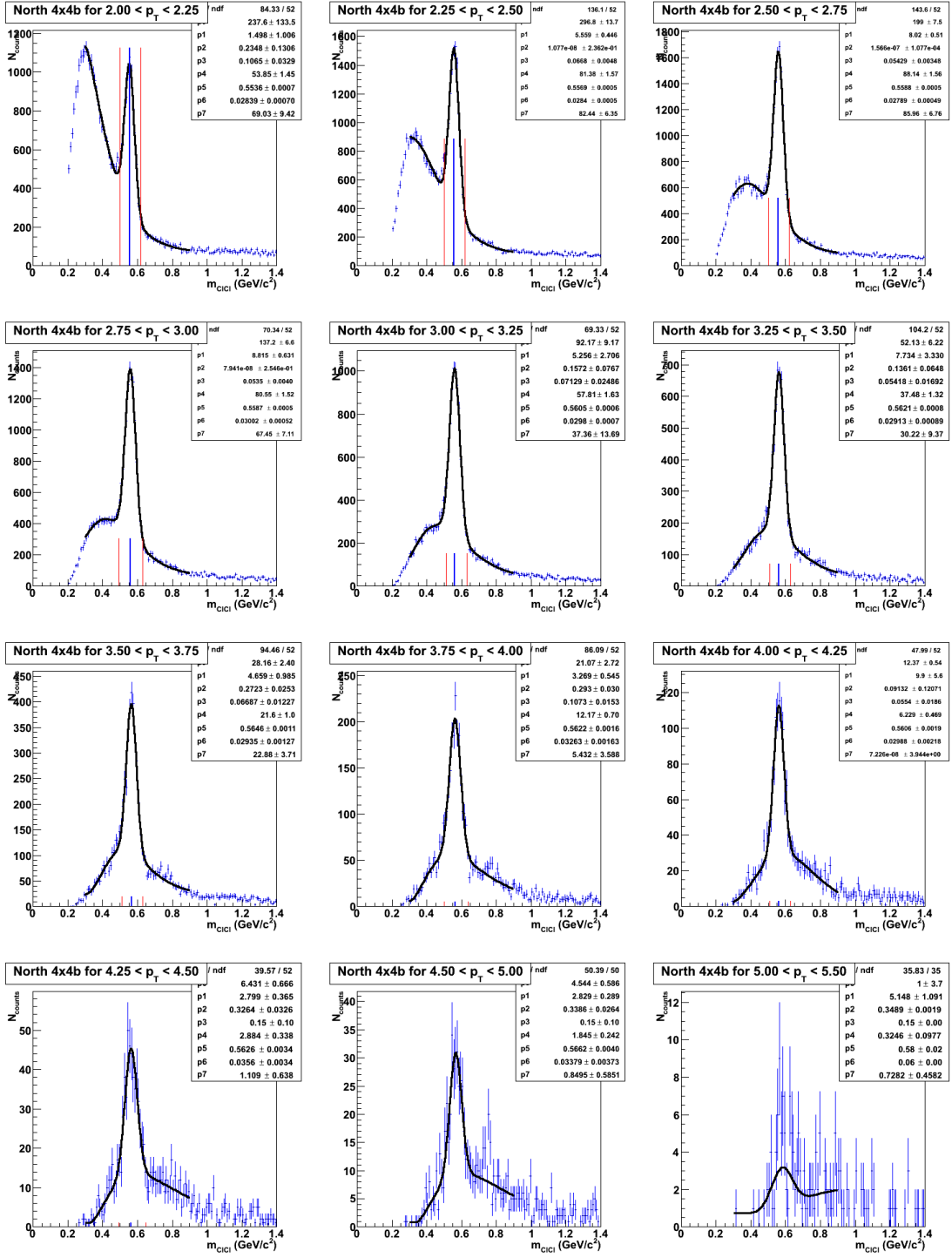


Figure 4.12: The invariant mass distributions in the North MPC for the  $4 \times 4B$  triggered dataset, binned in  $p_T$ . The correlated background + signal is fitted with Eq.4.6.

## 4.4 Corrections for the $\eta$ meson yields

The raw spectra in Fig. 4.8 are used to calculate the number of  $\eta$  mesons,  $dN_h$ , in the cross section given in Eq. 4.2. However, these represent only the  $\eta$  mesons that the MPC was able to identify, and not the whole number of  $\eta$  mesons that were actually produced. Experimentally, the MPC detector can only measure an  $\eta$  meson to a certain degree of efficiency. The efficiency to measure  $\eta$  mesons is determined by four factors: The branching ratio of the identification channel used ( $\epsilon_{br}$ ), the geometric acceptance of the detector ( $\epsilon_{geo}$ ), the efficiency of the detector to reconstruct an  $\eta$  meson ( $\epsilon_{det}$ ), and the efficiency of the trigger in recording the data ( $\epsilon_{trig}$ ). The number of measured  $\eta$  mesons is then related to the number produced via

$$N_h^{meas} = \epsilon_{br} \cdot \epsilon_{geo} \cdot \epsilon_{det} \cdot \epsilon_{trig} \cdot N_h. \quad (4.7)$$

The Cross Section, from Equation 4.2, can be then written in experimental form is as follows:

$$E \frac{d^3\sigma_h}{dp^3} = \frac{1}{\mathcal{L}_{pp,inel}} \frac{1}{2\pi p_T} \frac{\Delta N_h^{meas}}{\epsilon_{br} \cdot \epsilon_{geo} \cdot \epsilon_{det} \cdot \epsilon_{trig} \Delta p_T \Delta \eta}. \quad (4.8)$$

The branching ratio (first mentioned in Section 4.3) for  $\eta \rightarrow \gamma\gamma$ , is  $\epsilon_{br} = 0.3942$  [84]. The trigger efficiency  $\epsilon_{trig}$  is calculated from a combination of real data and simulations. The combination of  $\epsilon_{geo}$  and  $\epsilon_{det}$  gives the reconstruction efficiency,  $\epsilon_{reco} = \epsilon_{geo} \cdot \epsilon_{det}$  of the MPC, and is calculated using simulations.

The same set of simulations is used to calculate both  $\epsilon_{reco}$  and  $\epsilon_{trig}$ . The simulations set will be outlined in the next section, followed by the reconstruction efficiency in Section 4.4.2, and the procedure to calculate the Minimum Bias and 4×4B trigger

efficiency in Sections 4.4.3 and 4.4.4, respectively.

#### 4.4.1 Single $\eta$ Meson Simulations

In order to calculate the needed corrections to the cross section measurement, a full Monte Carlo of single  $\eta$  mesons is *generated*. Using Pythia [86],  $\approx 80$  million single  $\eta$  mesons are generated flat in  $p_T$  ( $0.3 < p_T < 6.0$  GeV/c), flat in pseudorapidity ( $2.5 < |\eta| < 4.5$ ), and with a 42 cm width Gaussian distributed  $z$ -vertex, see Fig. 4.13.

In order to produce  $\eta$  mesons similar to those we reconstruct in the Minimum Bias (4×4B) triggered dataset, the generated  $z$ -vertex distribution is weighted to represent to the Minimum Bias (4×4B) triggered dataset  $z$ -vertex distribution (see Fig. 4.14). Then the generated single  $\eta$  mesons are passed through the GEANT [87] based PHENIX software. Finally, the *reconstructed*  $\eta$  mesons are embedded into real Minimum Bias events. The same event selection criteria from Section 4.2 ( $-30 < z < 30$  cm cut) and the full reconstruction chain outlined in Section 4.3 (with the same cluster identification and pair cuts) is then followed to form the invariant mass distributions, as shown in Fig. 4.15.

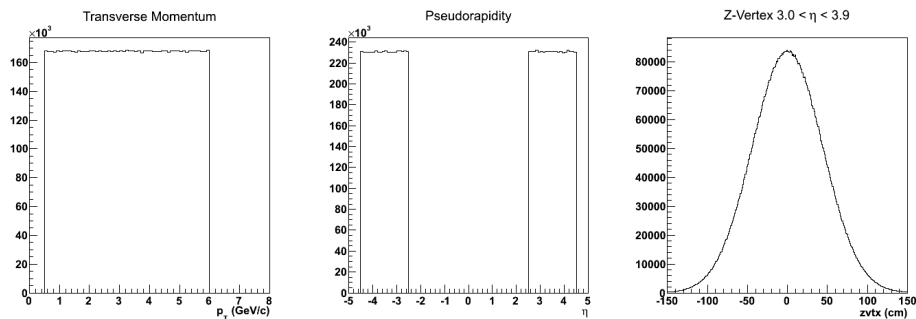


Figure 4.13: The generated  $p_T$ , pseudorapidity, and  $z$ -vertex distributions for the simulation of 10 million  $\eta$  mesons.

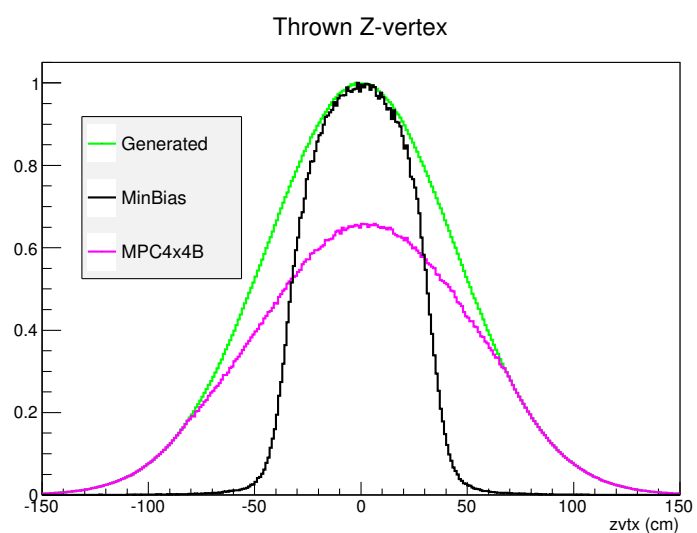


Figure 4.14:  $z$ -vertex weighting shown for each trigger configuration. Green represents the generated  $z$ -vertex, black represents the weighting applied to the generated  $z$ -vertex distribution to obtain the Minimum Bias triggered dataset  $z$ -vertex distribution, magenta represents the weighting for the  $4 \times 4$ B triggered dataset  $z$ -vertex distribution.

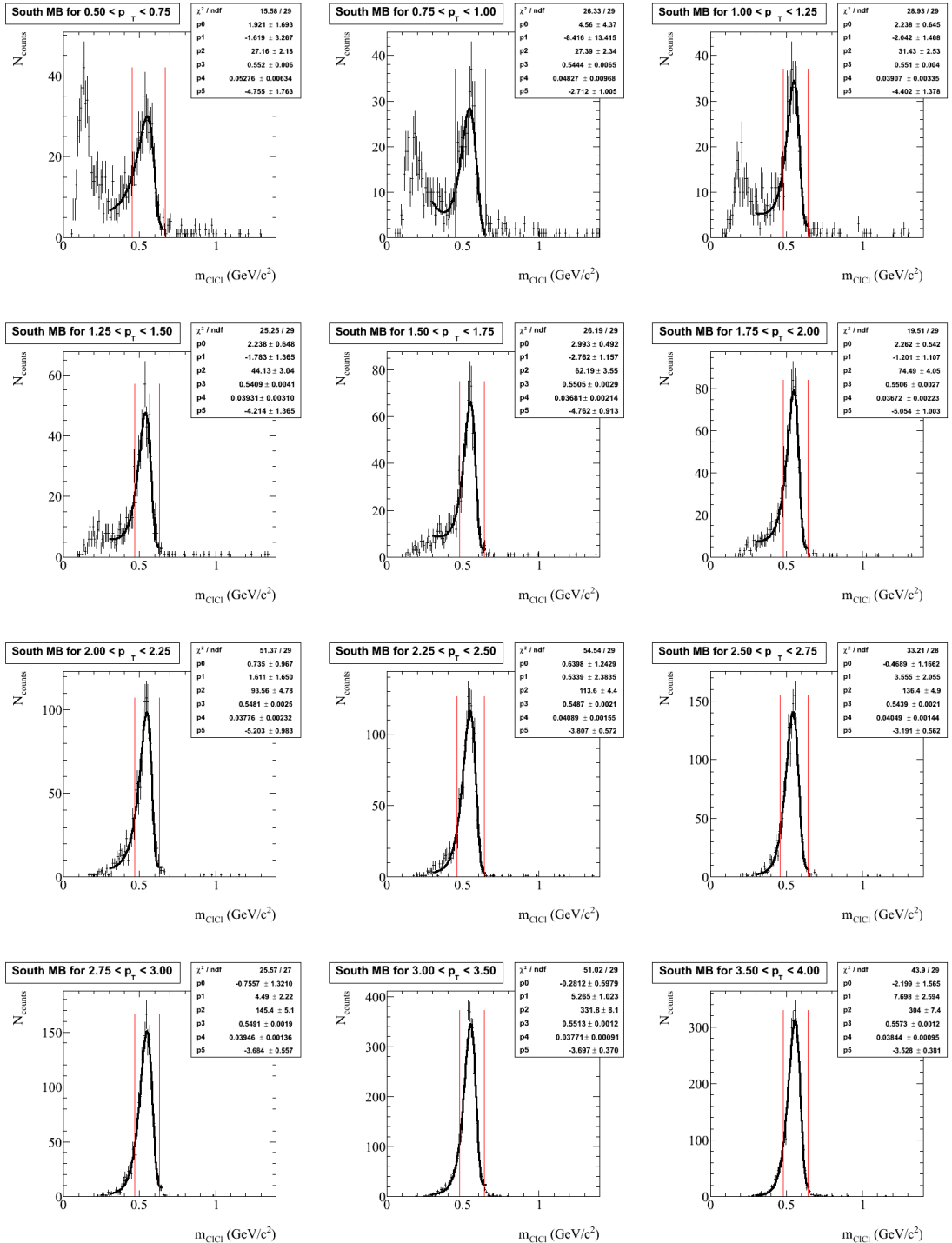


Figure 4.15: The reconstructed single  $\eta$  meson simulations in the South MPC.

#### 4.4.2 Reconstruction Efficiency

The reconstruction efficiency is the probability that an  $\eta$  meson generated at a given  $p_T$  and pseudorapidity will be reconstructed in the MPC.

$$\epsilon_{reco}(p_T^{reco}, \eta^{reco}) = \frac{N^{reco}(p_T^{reco}, \eta^{reco})}{N^{gen}(p_T^{gen}, \eta^{gen})} \quad (4.9)$$

The simulations mentioned in Section 4.4.1 are used to calculate the reconstruction efficiency. The generated (reconstructed)  $\eta$  mesons are evaluated at the  $p_T$  for the denominator (numerator) in Eq. 4.9. Since the simulations are generated with a flat distribution in  $p_T$  and pseudorapidity, both the numerator and denominator in Eq. 4.9 must be weighted based on the generated  $p_T$  and pseudorapidity.

$$\epsilon_{reco}(p_T^{reco}, \eta^{reco}) = \frac{\sum N^{reco}(p_T^{reco}) \times w(p_T^{gen}) \times w(\eta^{gen})}{\sum N^{gen}(p_T) \times w(p_T^{gen}) \times w(\eta^{gen})} \quad (4.10)$$

This weighting accounts for asymmetric  $p_T$  smearing effects at the edge of the reconstructed  $p_T$  bins, and for the falling pseudorapidity dependence at forward rapidity. The efficiency is weighted in  $p_T$  and pseudorapidity using an iterative procedure

1. Weight generated and reconstructed  $\eta$  mesons using a reasonable function. For this analysis, the initial weighting was found using by simulating  $\eta$  meson spectra  $p_T$  and pseudorapidity spectra from  $p + p \rightarrow \eta + X$  at  $\sqrt{s} = 200$  GeV generated from Pythia. The weight in  $p_T$  is shown in Fig. 4.17. The weight in pseudorapidity is  $p_T$  dependent, and is shown in Figs. 4.18 and 4.19.
2. Calculate the reconstruction efficiency using Eq. 4.10
3. Apply the correction factor ( $\epsilon_{reco}$ ) to the measured yield (see Fig. 4.8) from the

real data,  $dN^{meas}/dp_T$ , by the reconstruction efficiency

$$\frac{dN}{dp_T} = \frac{dN^{meas}}{dp_T} / \epsilon_{reco} \quad (4.11)$$

If measuring the reconstruction efficiency for the  $4\times 4B$  trigger, the  $\epsilon_{4\times 4B}$  from Fig. 4.22 is included to account for  $4\times 4B$  turn on in the measured yield (see Fig. 4.8)

$$\frac{dN}{dp_T} = \frac{dN^{meas}}{dp_T} / (\epsilon_{reco} \times \epsilon_{4\times 4B}) \quad (4.12)$$

4. Fit the corrected yields in Eq. 4.11 with a power law function.

$$f(p_T) = a \left( \frac{b}{b+1} \right)^c \quad (4.13)$$

Eq. 4.13 is parametrized and used as the  $p_T$  weighting function in the next iteration instead of  $p_T$  weighting input from Pythia.

5. Repeat steps one to three until convergence. For this analysis, it is repeated five times.

The final reconstruction efficiency for the South and North MPC after the sixth step of iteration is shown in Fig. 4.16. The North MPC has a lower efficiency than the South MPC, which is caused by the more restrictive warnmap in the North MPC due to the beam pipe stand and the noisy driver board.

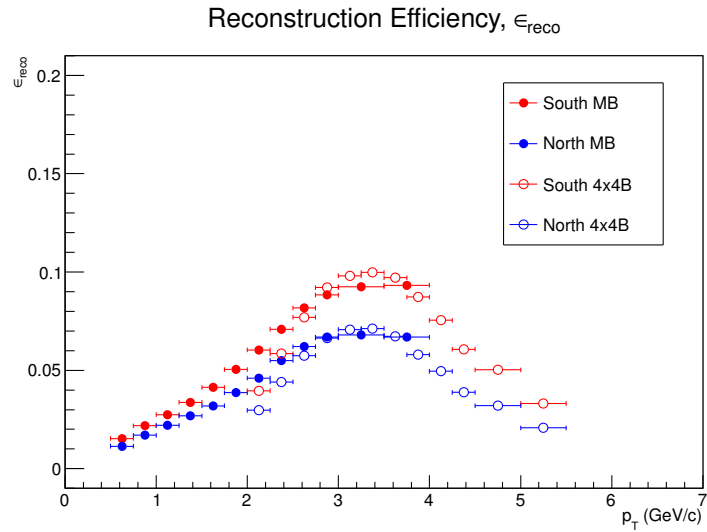


Figure 4.16: The reconstruction efficiencies for the Minimum Bias (4×4B) triggered dataset, shown in the left (right) panel. The red (blue) points are the reconstruction efficiency the South (North) MPC.

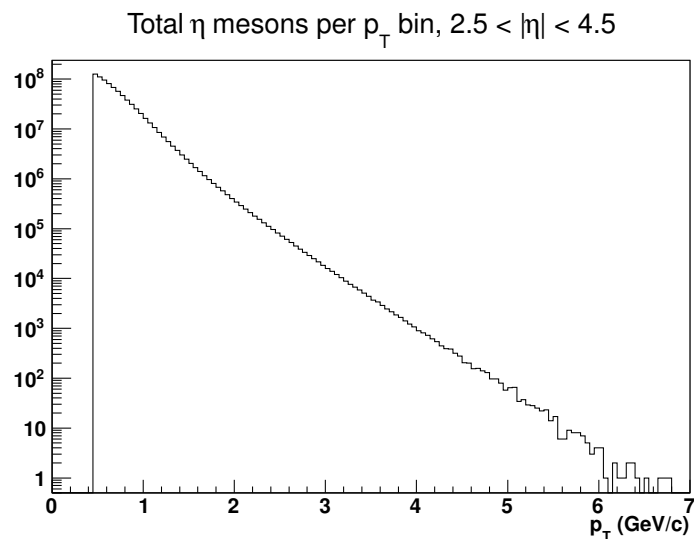


Figure 4.17: The  $p_T$  weighting functions binned in  $p_T$  for the Minimum Bias reconstruction efficiency. Input is calculated using Pythia.

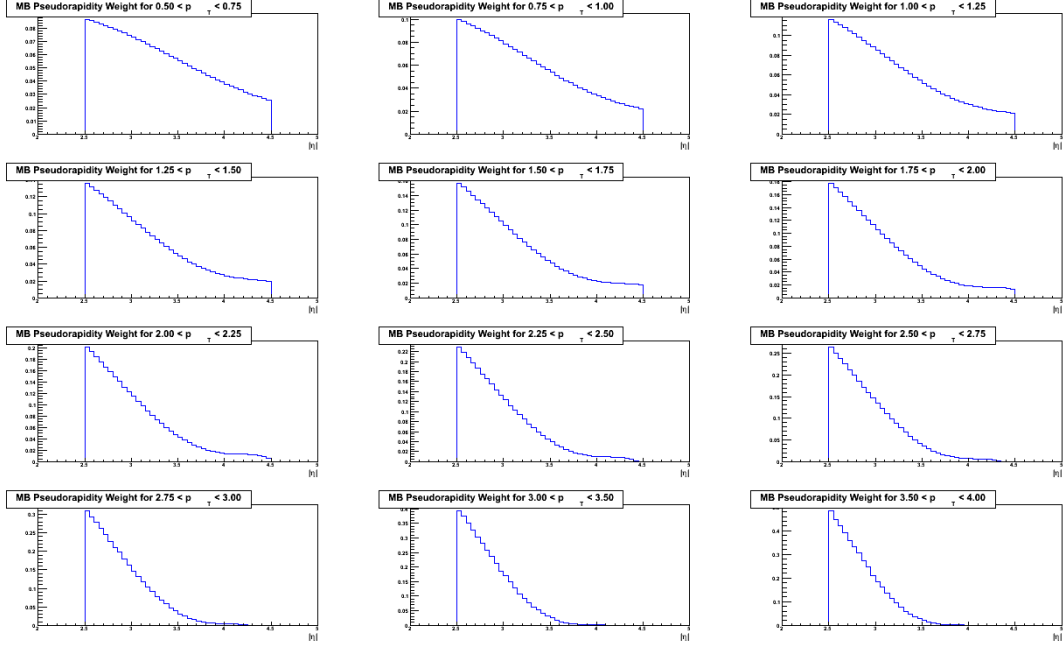


Figure 4.18: The pseudorapidity weighting functions binned in  $p_T$  for the Minimum Bias reconstruction efficiency. Input is calculated using Pythia.

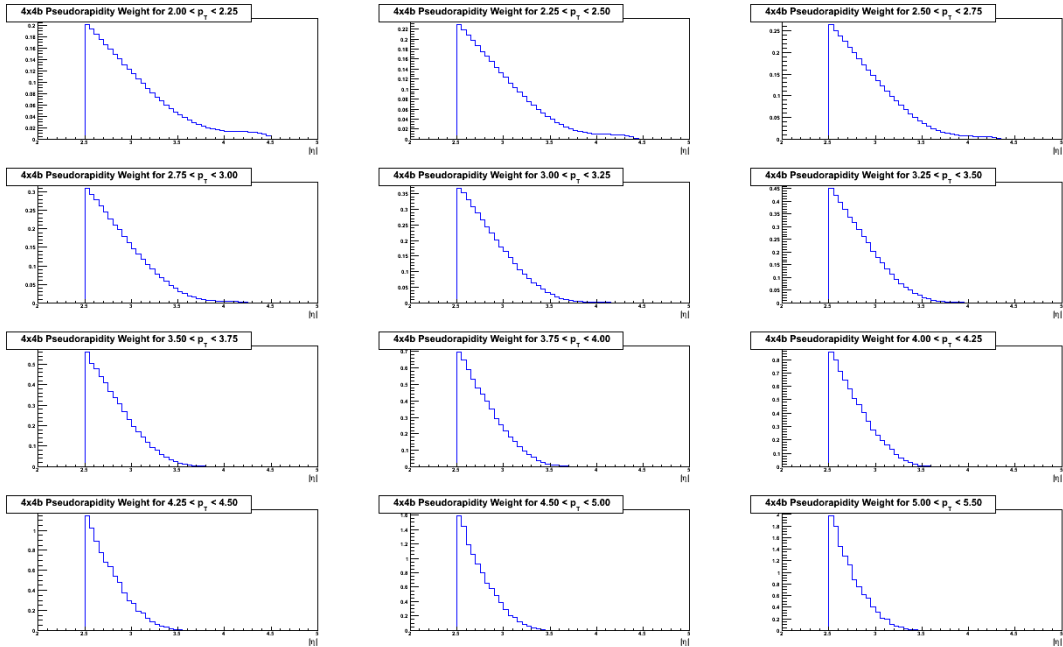


Figure 4.19: The pseudorapidity weighting functions binned in  $p_T$  for the  $4 \times 4B$  reconstruction efficiency. Input is calculated using Pythia.

#### 4.4.3 $\eta$ meson Minimum Bias trigger efficiency

The Minimum Bias trigger efficiency can be found by taking the ratio of  $\eta$  meson yields from the Minimum Bias trigger in coincidence with an unbiased trigger divided by the unbiased trigger. For the unbiased trigger, the  $4 \times 4B$  trigger is used as this maximises the  $\eta$  meson yield statistics. The Minimum Bias trigger efficiency is defined as

$$\epsilon_{trig}^{MB}(p_T) = \frac{N_{MB \wedge 4 \times 4B}^{\eta}(p_T)}{N_{4 \times 4B}^{\eta}(p_T)} \quad (4.14)$$

A certain fraction of events in the  $4 \times 4B$  triggered dataset have no  $z$ -vertex information, *i.e.* the BBC did not fire. The procedure in calculating these yields is the same as in [88], we set the  $z$ -vertex to zero for ALL pairs used in both the numerator and denominator, and the effect cancels out. The  $\eta$  meson peaks are smeared out, but the procedure to get the yields for the numerator and denominator is the same as in Section 4.3.2. The measured Minimum Bias trigger efficiency is independent of  $\eta$  meson  $p_T$ , and is shown in Fig. 4.20. The Minimum Bias trigger efficiency for the South (North) MPC is  $\epsilon_{MB}^{\eta} = 0.76$  ( $\epsilon_{MB}^{\eta} = 0.72$ )

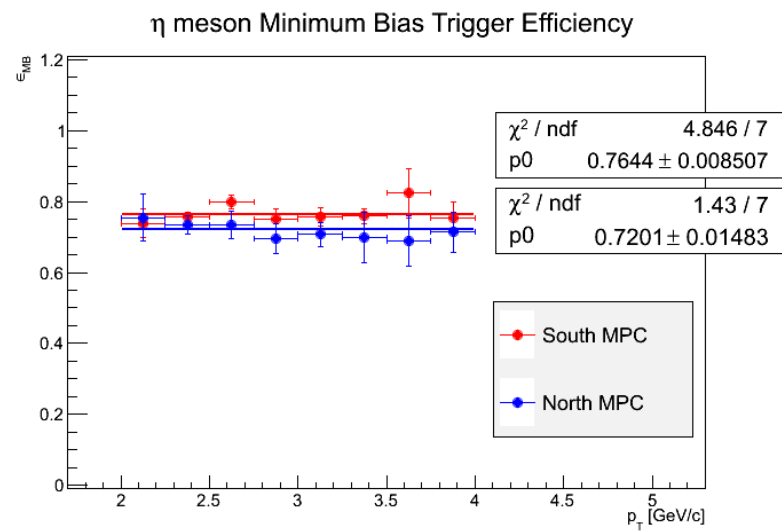


Figure 4.20: The  $\eta$  meson Minimum Bias trigger efficiency in the South and North MPC.

#### 4.4.4 The $\eta$ meson $4\times 4B$ trigger efficiency

The  $4\times 4B$  trigger efficiency can be found by taking the ratio of  $\eta$  meson yields of the  $4\times 4B$  trigger in coincidence with an unbiased trigger divided by the unbiased trigger. For the unbiased trigger, the Minimum Bias trigger is used. The  $4\times 4B$  trigger efficiency is defined as

$$\epsilon_{4\times 4B}^{\eta} = \frac{N_{4\times 4B \wedge MB}^{\eta}(p_T)}{N_{MB}^{\eta}(p_T)} \quad (4.15)$$

The statistics in the Minimum Bias sample is limited, however, and the efficiency can only be calculated to 3.0 GeV/ $c$ , see Fig. 4.22, and with poor statistics high systematic error due to low count yield extraction in the numerator of Eq. 4.15.

Instead, the  $4\times 4B$  trigger efficiency is calculated indirectly using the  $4\times 4$  trigger tiles ( $4\times 4$ ids) as a function of the sum of the ADCs of the towers in the tile

$$\epsilon_{4\times 4B}^{4\times 4id}(ADC) = \frac{N_{4\times 4B \wedge MB}^{4\times 4id}(ADC)}{N_{MB}^{\eta}(ADC)} \quad (4.16)$$

There are a total of 56 (61)  $4\times 4$ id tiles in the (South) North MPC. The use of the  $\epsilon_{4\times 4B}^{4\times 4id}$  as a function of ADC is done for two reasons. First, the  $4\times 4B$  trigger fires as a step function on ADC sum of the towers in the tile. The ADC of an MPC tower is converted to energy using Eq. 3.8. The relative gain changes throughout the RHIC Run due to temperature and radiation damage (see Section 3.3.3), as well as the initial non-uniformity of the gains of each tower in the MPC would make the  $4\times 4$ id efficiency as a function of energy impractical, as the ADC to energy conversion would smear out the trigger turn-on. Second, The distance between the two decay photons,  $\Delta R$ , is often small enough that the two photons fall into the same  $4\times 4$ id tile, so their energy sum

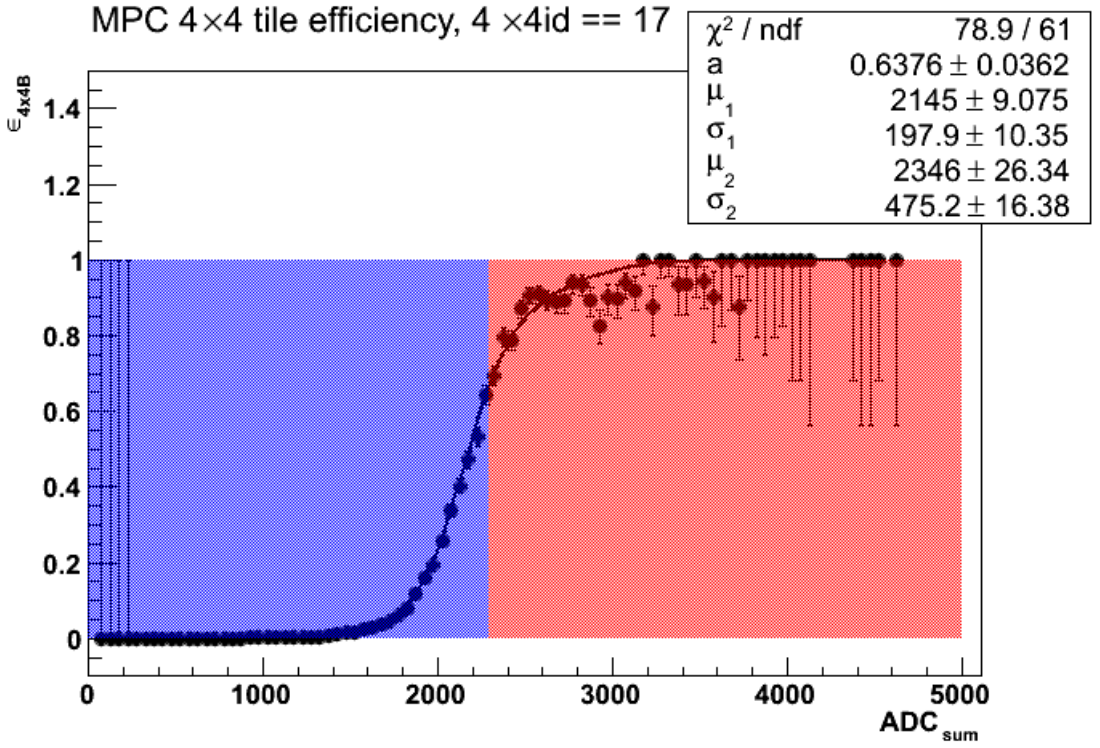


Figure 4.21: The  $4 \times 4$ id  $4 \times 4$ B trigger efficiencies for  $4 \times 4$ id=17. The red (blue) area represent ADC values above (below) the trigger threshold of  $\epsilon_{thresh} = 0.66$ . the ADC threshold for  $4 \times 4$ id=17 is 2295.

fires the trigger together.

The 127 individual  $4 \times 4$ id efficiencies calculated using Eq. 4.16 are fit with a double error function

$$f(x) = \int_{-\infty}^x [ag_1(x') + (1 - a)g_2(x')] \quad (4.17)$$

where  $g_1(x)$  and  $g_2(x)$  are Gaussian distributions. This is demonstrated by the fits to  $4 \times 4$ id = 17 in Fig. 4.21.

With fit parameters from the 127 different  $4 \times 4$ id efficiency curves, the  $\eta$  meson trigger efficiency can be calculated using the reconstructed single  $\eta$  mesons discussed in Section 4.4.1 as:

$$\epsilon_{4 \times 4B}^{\eta}(p_T^{reco}, \Theta) = \frac{\sum [N^{reco}(p_T^{reco}) \times \Theta(\theta_{cl1,4 \times 4id=(i,j,k,l)}(ADC), \theta_{cl2,i=(i,j,k,l)}(ADC))]}{\sum [N^{reco}(p_T)]} \quad (4.18)$$

Here the step function,  $\Theta(\theta_{cl1,4 \times 4id=(i,j,k,l)}(ADC), \theta_{cl2,i=(i,j,k,l)}(ADC))$ , checks whether either cluster in the MPC fires the trigger based on their underlying  $4 \times 4$ id ADC *threshold*,  $\epsilon_{4 \times 4B}^{4 \times 4id}(ADC_{thresh}) = \epsilon_{thresh}$ . If any underlying  $4 \times 4$ id ADC value for the given cluster is above the trigger threshold, it fires the trigger. There is up to four underlying  $4 \times 4$ ids for each cluster, so a total of up to eight  $4 \times 4$ id ADC values are checked to see if they fire the trigger. The trigger threshold criteria,  $\theta_{cl,i}(ADC)$ , and is defined as

$$\theta_{cl,i}(ADC) = \begin{cases} 1 & [ADC > \epsilon_{thresh} = 0.66] \\ 0 & [ADC < \epsilon_{thresh} = 0.66] \end{cases} \quad (4.19)$$

which fires when the ADC value of any underlying  $4 \times 4$ id is above the trigger threshold, which was found to be ideal at  $\epsilon_{thresh} = 0.66$ . The selection of the  $\epsilon_{thresh}$  is included in the systematic error discussion for  $\epsilon_{4 \times 4B}^{\eta}$  in Section 4.6.5.

Figure 4.22 shows the  $\eta$  meson  $4 \times 4B$  trigger efficiency calculated using Eq. 4.18, shown as green points with the systematic error shown as green bands around the points (see Section 4.6.5). The red points represent  $\epsilon_{4 \times 4B}^{\eta}$  as calculated using Eq. 4.15 from the Minimum Bias triggered dataset. The use of the  $4 \times 4$ id to calculate the  $4 \times 4B$  trigger efficiency is in agreement with the statistically limited values measured from the Minimum Bias trigger in the overlap region of  $2.0 < p_T < 3.0$  GeV/ $c$ .

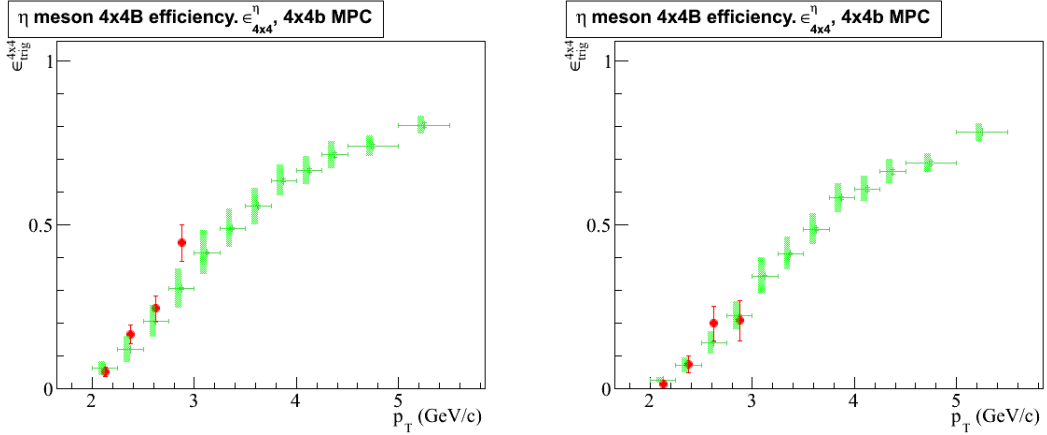


Figure 4.22: The  $\eta$  meson  $4 \times 4$ B trigger efficiency,  $\epsilon_{4 \times 4}^\eta$ . The red points represent  $\epsilon_{4 \times 4}^\eta$  calculated using Eq. 4.15 using the Minimum Bias triggered dataset. The blue points represent  $\epsilon_{4 \times 4}^\eta$  calculated using Eq. 4.18 with  $4 \times 4$ id efficiencies from Eq. 4.16.

## 4.5 Luminosity

The sampled integrated luminosity in PHENIX is estimated from the number of inelastic  $p + p$  collisions that are counted in the trigger,  $N_{pp,inel}^{meas}$ , and the known inelastic cross section for inelastic  $p + p$  collisions,  $\sigma_{pp,inel} = 42.2$  mb [84]. As the trigger is not 100% efficient, a correction must be applied to account for the number of interactions missed by the trigger

$$\mathcal{L}_{pp,inel} = \frac{N_{pp,inel}}{\sigma_{pp,inel}} = \frac{N_{pp,inel}^{meas}}{\epsilon_{BBC} \cdot \sigma_{pp,inel}} = \frac{N_{pp,inel}^{meas}}{\sigma_{BBC}} \quad (4.20)$$

where  $\epsilon_{BBC}$  is the efficiency of the BBC detector to measure an inelastic  $p + p$  collision. The efficiency of the BBC to detect inelastic collisions was estimated using a Vernier scan in a prior data set [89] to be  $\epsilon_{BBC} = 0.545$ . This is used here as the BBC detector configuration has not changed in the intervening years. The BBC cross section for inelastic  $p + p$  collisions at  $\sqrt{s} = 200$  GeV can be written as  $\sigma_{BBC} = \epsilon_{BBC} \times \sigma_{pp,inel}$ . The systematic error on  $\sigma_{BBC}$  is discussed in Section 4.6.6. The sampled luminosity is calculated for each trigger separately.

### 4.5.1 Integrated Luminosity of the Minimum Bias Trigger

The sampled integrated luminosity is determined from the number of analyzed Minimum Bias events whether or not an  $\eta$  meson is present. For this dataset a total of  $N_{MB}^{evts} = 4.43 \times 10^8$  events were recorded by this trigger, giving a total integrated luminosity of  $\mathcal{L}_{MB} = 1.92 \times 10^{-2} pb^{-1}$ .

### 4.5.2 Luminosity of the 4×4B Trigger

As the 4×4B trigger does not represent a “minimum bias” sample, the same  $\sigma_{BBC}$  cannot be used in conjunction with the number of recorded events. As measuring the precise 4×4B cross section is not possible, the number of *underlying* minimum bias events from the BBCs is used, even though these may not be read out and recorded in data. The number of underlying Minimum Bias events,  $\tilde{N}_{MB}^{evts}$ , of the 4×4B triggered dataset is found by taking the number of analyzed 4×4B events times the trigger *rejection factor*, which is obtained from the Minimum Bias triggered dataset

$$\tilde{N}_{MB}^{evts} = N_{4\times 4B}^{evts} \cdot \text{Rejection} = N_{4\times 4B}^{evts} \cdot \left[ \frac{N_{MB}^{evts}}{N_{MB}^{evts} \wedge N_{4\times 4B}^{evts}} \right]_{MB} \quad (4.21)$$

The total luminosity sampled for this trigger is then given by

$$\mathcal{L}_{4\times 4B} = \sum_{run} \frac{\tilde{N}_{MB}^{evts}}{\sigma_{BBC}} = \sum_{run} \frac{N_{4\times 4B}^{evts}}{\sigma_{BBC}} \times \text{Rejection} \quad (4.22)$$

The luminosity is calculated on a run by run basis to take into account gain changes in the MPC. The number of 4×4B events and Rejection factors are shown in Fig. 4.23.

The total sampled integrated luminosity of the 4×4B triggered dataset is  $\mathcal{L}_{4\times 4B} = 3.87 pb^{-1}$ .

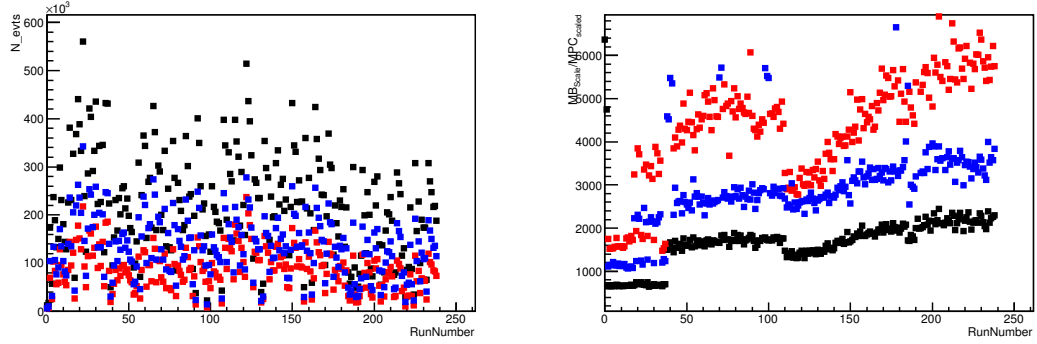


Figure 4.23: The left panel shows the number of analyzed  $4 \times 4$ B events for South (red), North (blue) and combined (black)  $4 \times 4$ B triggers. The right panel shows the estimated rejection factor.

## 4.6 Systematic studies

The PHENIX collaboration defines systematic errors on measurements in three different ways

- **Type A.** Point-to-point random systematic errors.
- **Type B.** Internal correlated systematic errors, by which all the points move by the same amount
- **Type C.** External Global systematic errors which underlay the measurement

### 4.6.1 Energy Scale

A scale error of the MPC is  $\delta E/E = 2\%$  is used to account for the uncertainty in the MPC energy scale [85]. The energy scale systematic is applied to the functional form of the spectra, and to the reconstruction efficiency, outlined in the next two sections.

#### 4.6.1.1 Functional Form

The scale error is propagated into the systematic uncertainty for the spectral functional form of the spectra,  $f(p_T) = dN/dp_T$ , via

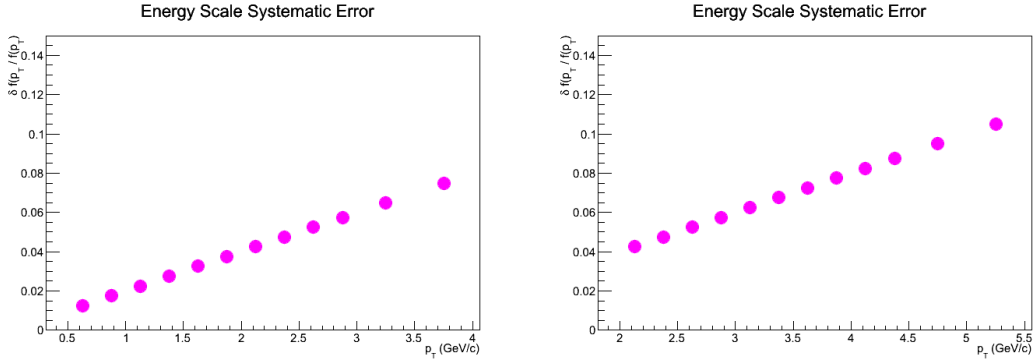


Figure 4.24: Energy scale systematic error on the measured invariant yields. The left panel shows Minimum Bias triggered dataset, the right shows the is for  $4 \times 4B$  triggered dataset.

$$\delta f(p_T = |\frac{df(p_T)}{dp_T}|^{p_T} \times 0.02p_T) \quad (4.23)$$

The functional form ( $f(p_T)$ ) used is the  $p_T$  spectra from the final iteration step from Eq. 4.13. The average of the South and North MPC is used for this systematic error. The results are shown in Fig. 4.24, and varies from 1% at low  $p_T$  to 10% at the maximum  $p_T$  in this analysis. The energy scale systematic error is a type-A systematic error.

#### 4.6.1.2 Reconstruction Efficiency

An additional energy scale systematic is calculated using the reconstruction efficiency in Eq. 4.10 where the underlying energy of the cluster is adjusted by  $E_{cl} = E_{cl} \pm 0.02 * E_{cl}$ . The calculated reconstruction efficiencies, along with their differences are shown in Fig. 4.25. The final systematic error is calculated by taking the greater error of the  $\pm 2\%$  adjustment in the South or North MPC, and is shown in Fig. 4.26. The energy scale systematic error is a type-A systematic error.

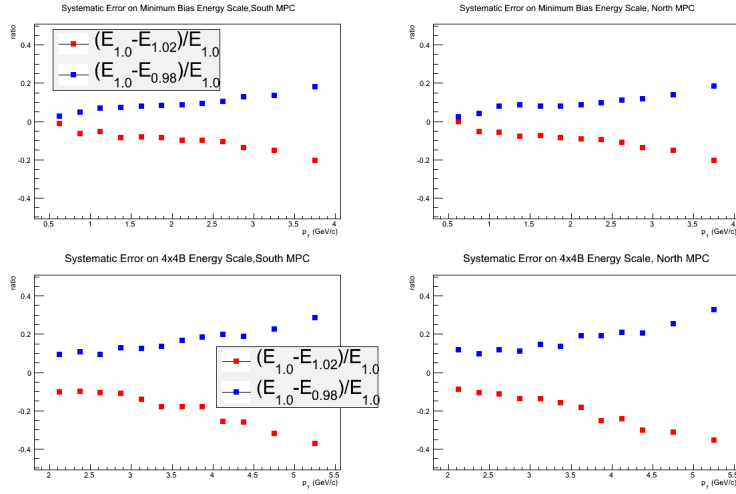


Figure 4.25: The systematic error as adjusted by the energy scale. The left (right) panel is for the South (North) MPC. The red (blue) represent the difference in the reconstruction efficiency after adjusting the energy scale of the clusters by  $+(-)2\%$ .

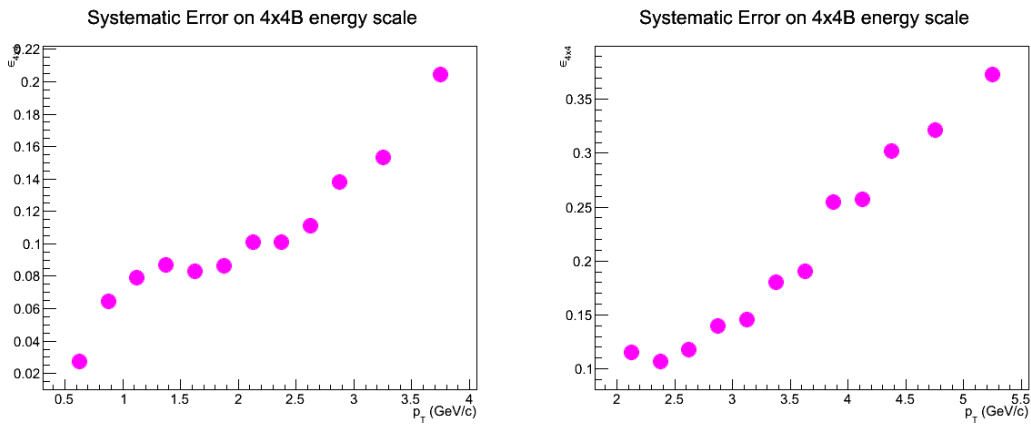


Figure 4.26: Energy Scale systematic error on the Measured Invariant Yields. The left plot is for Minimum Bias triggered dataset, the right plot is for  $4 \times 4B$  triggered dataset.

### 4.6.2 Yield extraction

To estimate the systematic uncertainty due to the fit function used to measure the signal (Gaussian) and background (exponential) from Eqs. 4.5 and 4.6, several alternative fits were used. First, the background function was kept the same (exponential), and the normalized Gaussian was changed to an asymmetric Gaussian.

$$F(x) = ae^{-bx} + \frac{N}{\sigma\sqrt{2\pi}}e^{-\frac{1}{2}\left(\frac{x-M}{(1+\sin(x-\alpha))\cdot\sigma}\right)^2} \quad (4.24)$$

where  $\alpha$  represent the asymmetric skewness of the Gaussian. A second test changed the assumed background to a second (or third) degree polynomial, and used the original (symmetric) Gaussian for the signal. The variation to the fits are demonstrated in Fig. 4.27. The systematic difference between symmetric versus asymmetric Gaussian signal form is less than 2%. A larger uncertainty is found from the background function. The final systematic error is calculated by taking the greater error of the two polynomials in the South or North MPC. The systematic error results for the South or North MPC are shown in Fig. 4.28; final values are shown in Fig. 4.29. The yield extraction systematic error is a type-A systematic error.

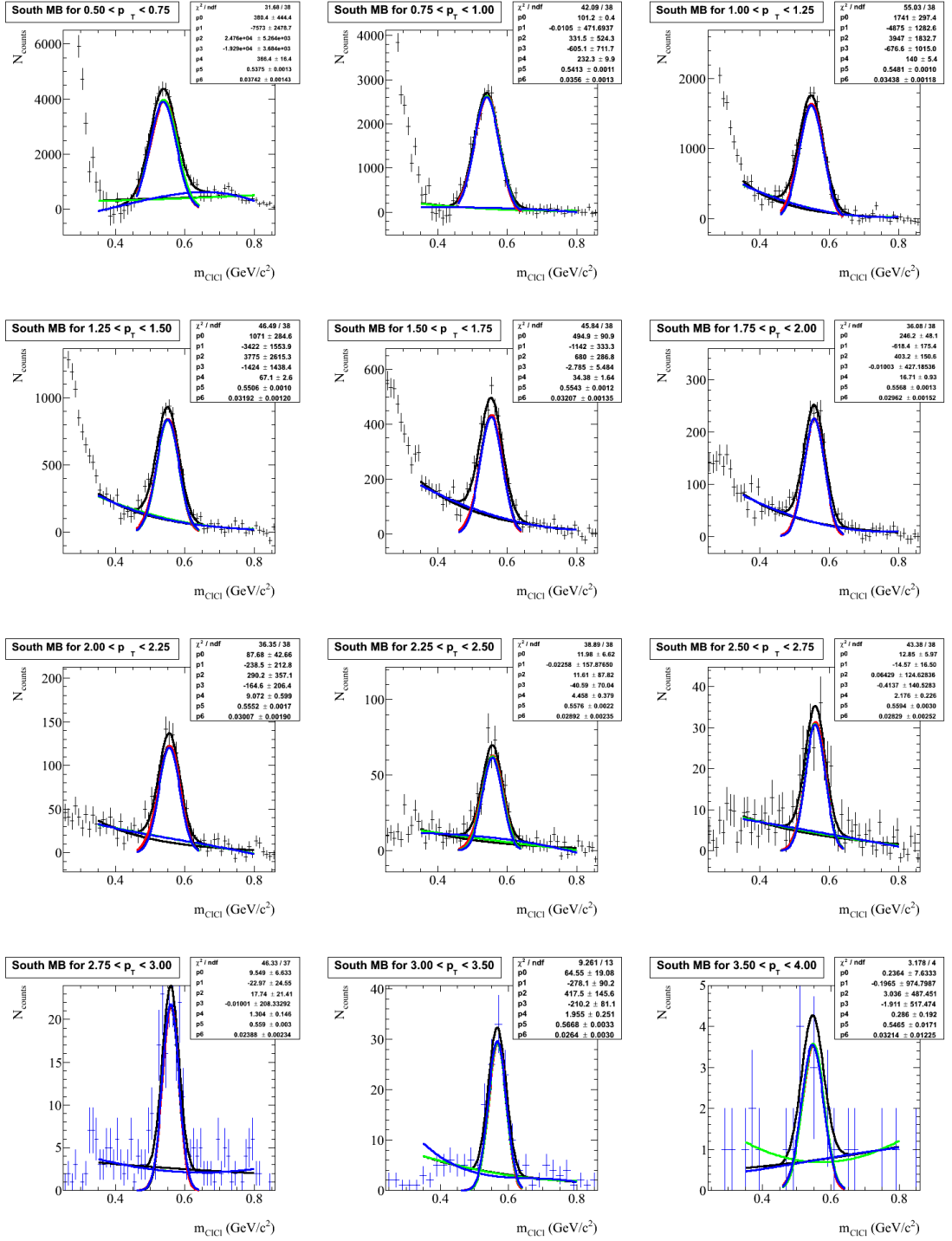


Figure 4.27: Varying the fits to the background for the Minimum Bias triggered dataset in the South MPC. The black fit is the original exponential background function fit. The red (partially hidden) is for changing the signal fit to an asymmetric Gaussian. The green (blue) is for changing the background fit to a 2nd (3rd) order polynomial.

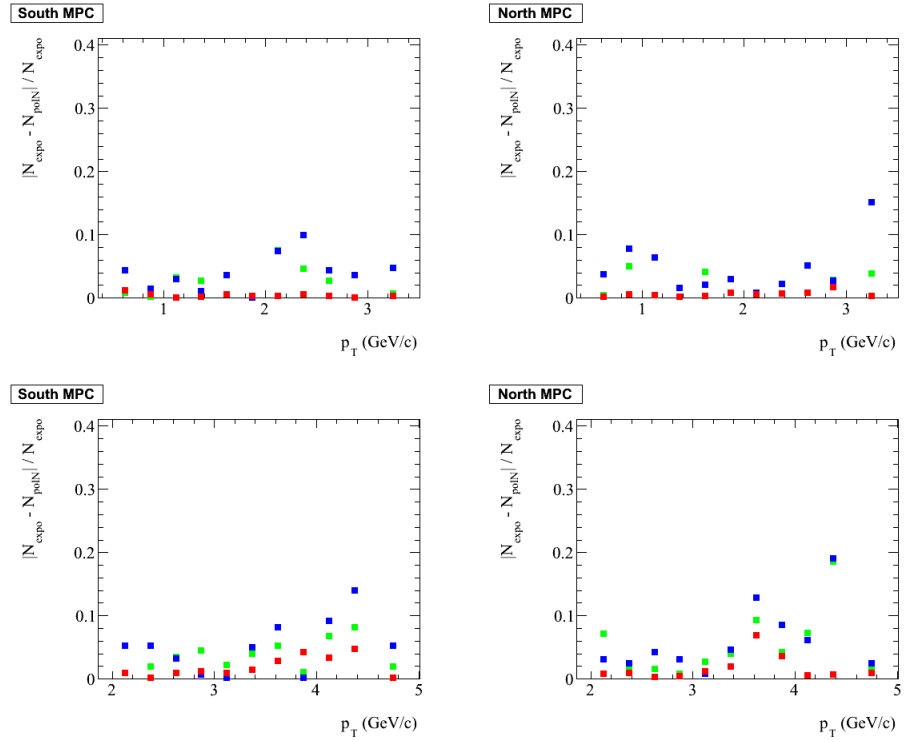


Figure 4.28: The systematic error on varying the background + signal fit. The red is for changing the signal fit to an asymmetric Gaussian. The green (blue) is for changing the background fit to a 2nd (3rd) order polynomial. The top row is for Minimum Bias triggered data, the bottom row is for  $4 \times 4B$  triggered data.

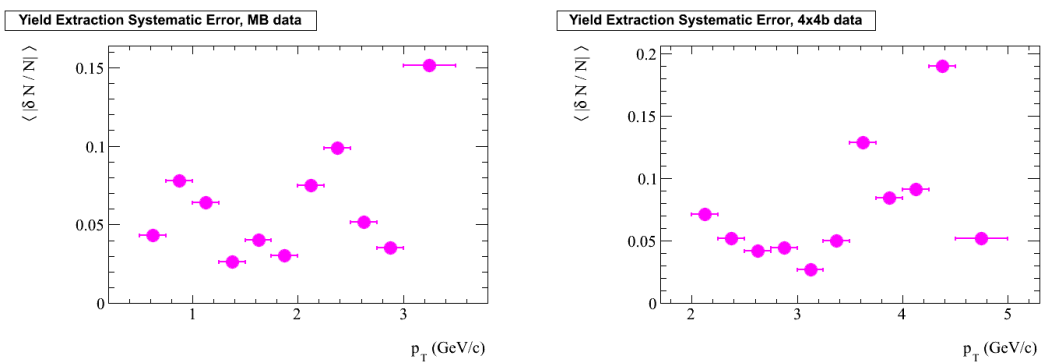


Figure 4.29: The systematic error on the measured invariant yield.

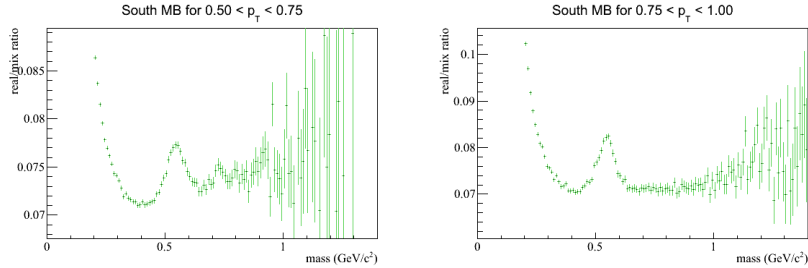


Figure 4.30: The real/mixed event ratios for the two lowest  $p_T$  bins in the South MPC. The uncorrelated flat region to fit for determining scaled mixed event subtraction is varied for this systematic.

#### 4.6.3 Mixed Event Subtraction

To procure quality  $\eta$  meson yields at low  $p_T$ , the mixed event subtraction technique is used. To subtract off the mixed event distribution, must first be normalized to the real event distribution. This is done by dividing the real distribution by the mixed-event distribution, and fitting a flat region away from the  $\eta$  meson peak with a constant. The value of this constant is used to scale the mixed event distribution to the real event distribution. Figure 4.30 demonstrates the real-mixed event ratio in the lowest  $p_T$  bins. Note that in these particular  $p_T$  bins, it is difficult to determine where to fit a flat region with a constant in the uncorrelated regions around the  $\eta$  meson region in the real to mixed event ratio. A systematic study is done to determine the extracted  $\eta$  meson yield error based on the fit region chosen. The largest yield difference in each  $p_T$  bin from the South or North MPC is used as the systematic error for the particular bin. The final values are shown in Fig. 4.31. Note that the effect is very small in bins above 1.0 GeV/ $c$ . The mixed event subtraction systematic error is a type-A systematic error, and is added linearly to the yield extraction systematic error.

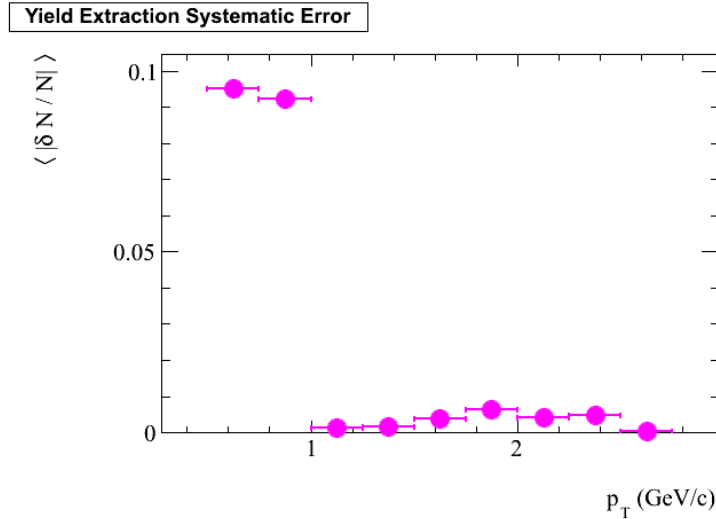


Figure 4.31: The systematic error on the mixed event subtraction.

#### 4.6.4 GEANT

To estimate something missing in using the GEANT framework for calculating the reconstruction efficiency, 100 million  $p + p$  Pythia events were generated and passed through the GEANT framework. The cross section was calculated for this “Pythia Trigger”, with the Reconstruction efficiency used being the same that used for the Minimum Bias reconstruction efficiency. The reconstructed Pythia cross section versus the generated Pythia cross section is given in Fig. 4.32. A fit across the difference of the two gives a systematic error of 6%. The reconstruction efficiency systematic error is a type B systematic error.

#### 4.6.5 $\eta$ meson 4×4B trigger efficiency

In order to use the 4×4id efficiencies to calculate  $\epsilon_{4\times 4B}^\eta$ , the threshold settings of the 4×4id efficiencies must reproduce the  $\epsilon_{4\times 4B}^{cl}$  first. The cluster efficiency is defined as

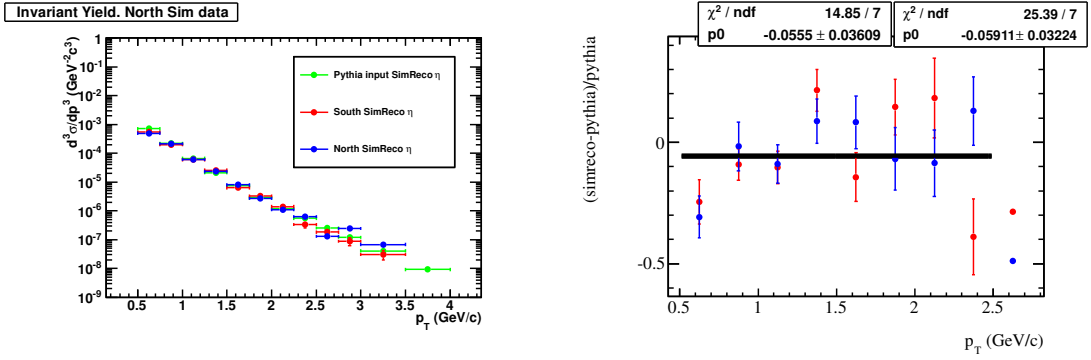


Figure 4.32: . Calculation of the cross section using Pythia simulations. The left panel shows the cross section as measured from Pythia (green points), and after the Pythia is passed through the GEANT framework and measured just like in the Minimum Bias triggered dataset (red and blue points). The right panel shows the difference between the generated and reconstructed Pythia cross sections.

$$\epsilon_{4 \times 4B}^{cl}(p_T) = \frac{N_{4 \times 4b \wedge MB}^l(p_T)}{N_{MB}^\eta(p_T)} \quad (4.25)$$

Using reconstructed  $p + p$  events from Pythia simulations, the cluster trigger efficiency is reproduced using a cluster efficiency variation of Eq. 4.18

$$\epsilon_{4 \times 4B}^{cl}(p_T^{reco}, \Theta) = \frac{\Sigma [N^{reco}(p_T^{reco}) \times \Theta(\theta_{cl, 4 \times 4id=(i,j,k,l)}(ADC)]}{\Sigma [N^{reco}(p_T)]} \quad (4.26)$$

and varying the threshold turn-on in Eq. 4.19

$$\theta(ADC) = \begin{cases} 1 & [ADC_{4x4id,i} > \epsilon_{4x4id} = \epsilon_{thresh}], 0.6 < \epsilon_{thresh} < 0.75 \\ 0 & [ADC_{4x4id,i} < \epsilon_{4x4id} = \epsilon_{thresh}], 0.6 < \epsilon_{thresh} < 0.75 \end{cases} \quad (4.27)$$

The  $4 \times 4$ id turn-on threshold,  $\epsilon_{thresh}$  was adjusted between  $0.6 < \epsilon_{thresh}$  and  $\epsilon < 0.75$ , and the cluster trigger efficiency was calculated using these Pythia simulations and

compared to the real cluster efficiency. The value that worked best was  $\epsilon_{thresh} = 0.65$ , with a possible low (high) limit on the threshold of  $\epsilon_{thresh} = 0.60$  (0.75) to account for variational differences in each MPC. The systematic error is calculated by comparing the optimal  $\epsilon_{thresh} = 0.65$ , with the low and high threshold limits of  $\epsilon_{thresh} = 0.60$  and  $\epsilon_{thresh} = 0.75$ , respectively. These  $4 \times 4B$  versus Pythia cluster efficiencies are shown in Fig 4.33, and their ratios are shown Fig. 4.34. It can be seen in the ratio plots that the Minimum Bias and Pythia efficiencies agree well for  $E_{cl} > 30$  GeV, but it is difficult to establish agreement between methods below  $E_{cl} < 30$  GeV. This leads to a higher systematic error at lower  $p_T$  values. The values of  $\epsilon_{4 \times 4B}^\eta$  for the different  $\epsilon_{thresh}$  values is shown in Fig. 4.35. The final systematic error is calculated by taking the greater error of the low and high threshold values with respect optimal threshold value in the South and North MPC. The systematic error for the South and North MPC for the different thresholds is also shown in Fig. 4.35. The final systematic error is shown in Fig. 4.36. The  $4 \times 4B$  trigger efficiency systematic error is a type-A systematic error.

#### 4.6.6 BBC cross section

The efficiency of the BBC in detecting inelastic collisions is  $\epsilon_{BBC} = 0.545$  (see Section 4.5). The systematic of the BBC to detect inelastic collisions is a global systematic and is 9.7% [90]. This is a type-C systematic error.

### 4.7 Bin Shift Correction

The cross section is calculated using the  $\eta$  meson yields from Section 4.3, the corrections from Section 4.4, and the Luminosity from Section 4.5. One additional

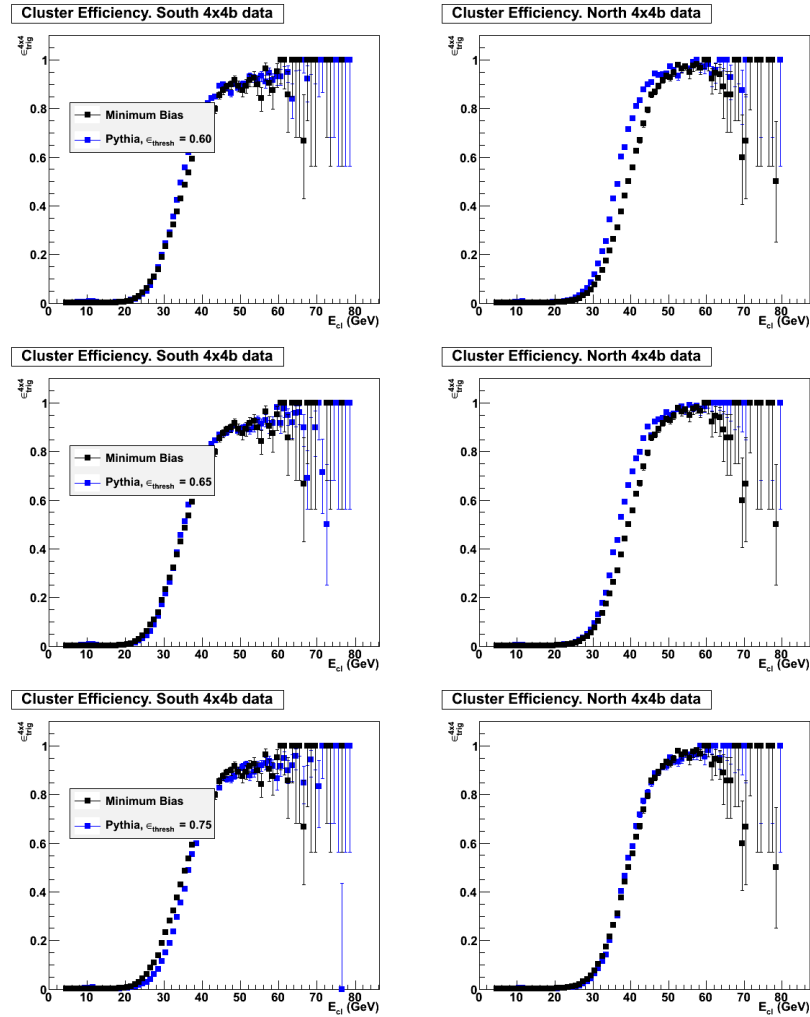


Figure 4.33: The  $4 \times 4B$  versus Pythia cluster efficiency varying  $\epsilon_{thresh}$ .  $\epsilon_{thresh} = 0.6$ ,  $\epsilon_{thresh} = 0.65$ ,  $\epsilon_{thresh} = 0.75$  is represented by the top, middle, and bottom row, respectively

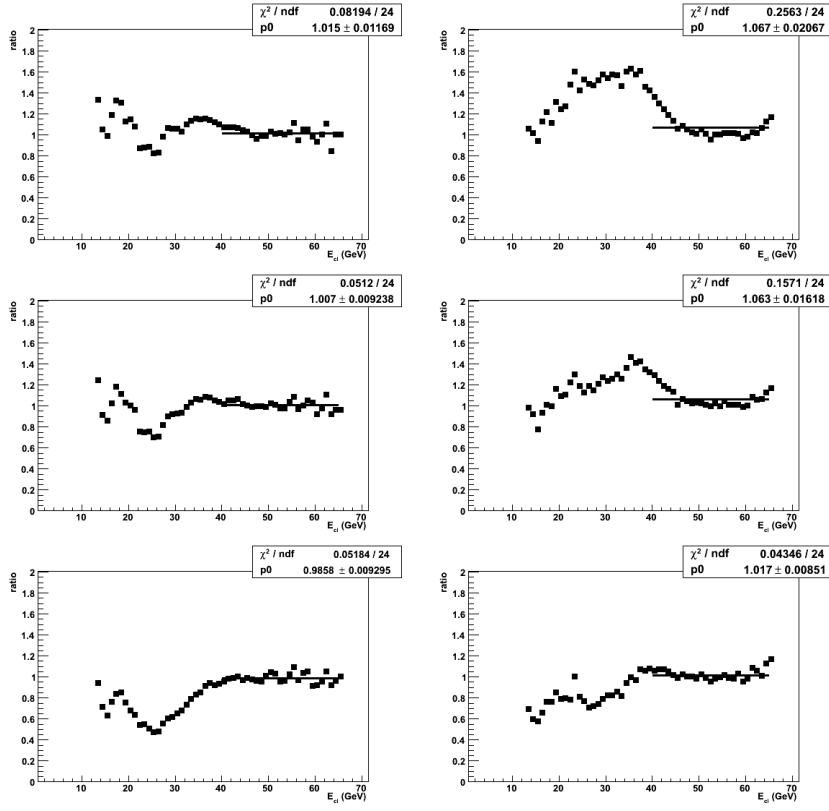


Figure 4.34: The  $4 \times 4$ B versus Pythia cluster efficiency ratios varying  $\epsilon_{thresh}$ .  $\epsilon_{thresh}n=0.6$ ,  $\epsilon_{thresh}=0.65$ ,  $\epsilon_{thresh}=0.75$  is represented by the top, middle, and bottom row, respectively

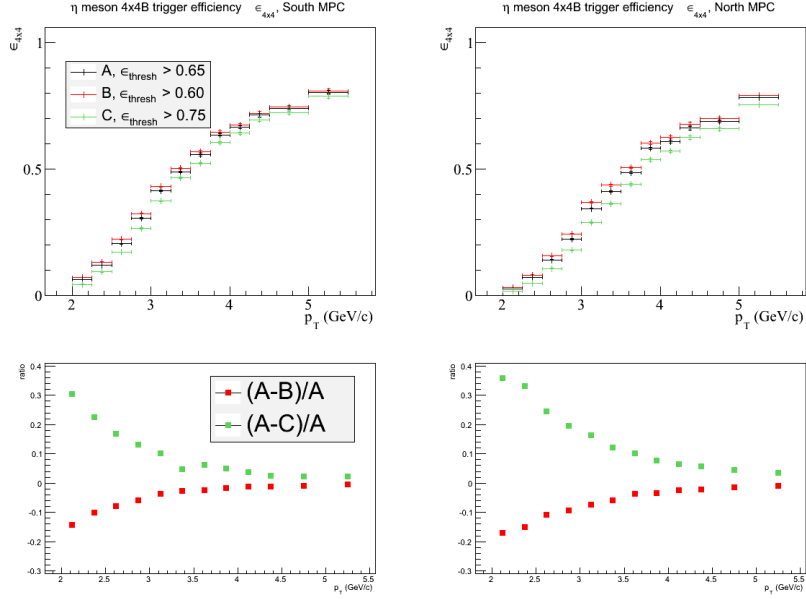


Figure 4.35:  $\epsilon_{4 \times 4B}^\eta$  calculated using  $\epsilon_{thresh}$  is shown in the top row.  $\epsilon_{thresh} = 0.65$ ,  $\epsilon_{thresh} = 0.60$ ,  $\epsilon_{thresh} = 0.75$  is shown by black, red, and blue points, respectively. The bottom row shows the systematic error on varying  $\epsilon_{thresh}$ .

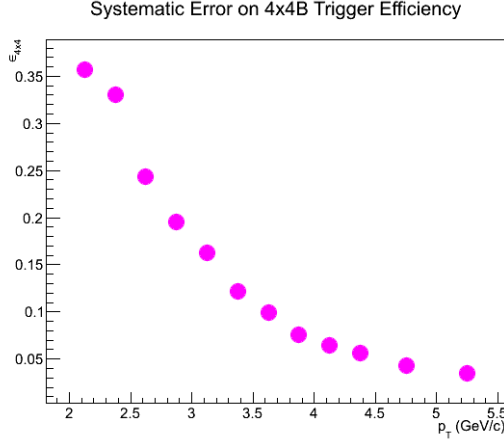


Figure 4.36: The final systematic error on  $\epsilon_{4 \times 4B}^\eta$ .

correction must be applied to the cross section. A bin shift correction is used to account for the difference between the true bin center and the mid-point of a  $p_T$  bin. The cross section is fit with an exponential function,  $f(x)$ , and is applied as a scale  $\sigma_{binshift} = \sigma / C_{up-down}$  for each  $p_T$  bin

$$C_{up-down} = \frac{f(\frac{p_{low} + p_{high}}{2})}{1/(p_{high} - p_{low}) \int_{p_{low}}^{p_{high}} f(x) dx} \quad (4.28)$$

The correction values for bins with  $p_T$  widths of 0.25 GeV/c is 0.95. The values of correction for bins with  $p_T$  widths of 0.50 GeV/c is 0.87.

## 4.8 Results

The measured cross section of  $\eta$  mesons in the South and North MPC for the Minimum Bias and  $4 \times 4B$  triggered datasets are shown in Fig. 4.37, with a comparison to simulated cross section results derived from 10 billion Pythia events. The ratio of the South MPC to the North MPC and their T-test distribution is shown in Fig. 4.38. The combined South and North cross section for both triggers, along with NLO pQCD calculation provided by Marco Stratmann [91] is displayed in Fig. 4.39. Comparison of each

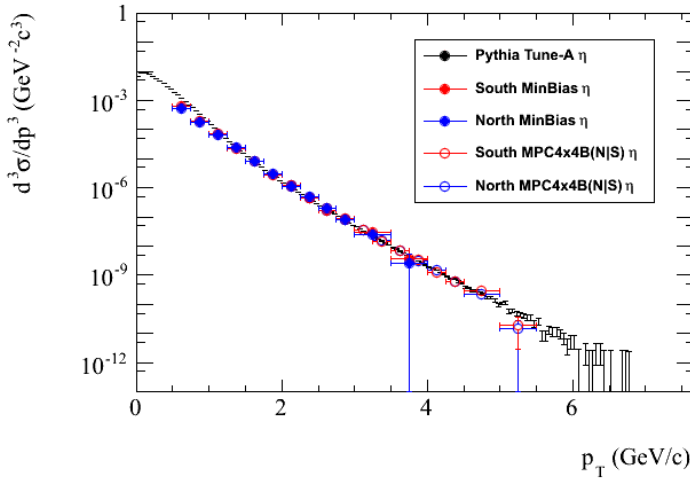


Figure 4.37: The Cross section of  $\eta$  mesons,  $3.0 < |\eta| < 3.8$ . Black(Red) points are from the South(North) MPC. The finely binned points are the cross section procured from 10 billion Pythia Tune-A events

of the Minimum Bias and  $4 \times 4B$  cross sections with each other is given in Fig. 4.40. For Minimum Bias and  $4 \times 4B$  points from  $2.0 < p_T < 3.5$  GeV/ $c$  the, points are comparable within the systematic uncertainty. Figure 4.41 compares the Cross Section Values with those from the NLO pQCD calculation. From this figure, some initial observations are made: The highest  $p_T$  points in the Minimum Bias trigger ( $3.0 < p_T < 4.0$  GeV/ $c$ ) have already been removed due to low statistics, and the systematic error on the  $4 \times 4B$  cross section points from  $2.0 < p_T < 3.0$  GeV/ $c$  is primarily due to uncertainty in the  $\epsilon_{4 \times 4B}^\eta$  efficiency calculation(see Section 4.6.5), while from  $3.0 < p_T < 5.5$  GeV/ $c$  it is primarily due to uncertainty in the Energy Scale (see Section 4.6.1).

The values of the yields, corrections, and errors are given in Appendix A in Tables A.3 and A.4. Final interpretation of the results is reserved for Chapter 6.

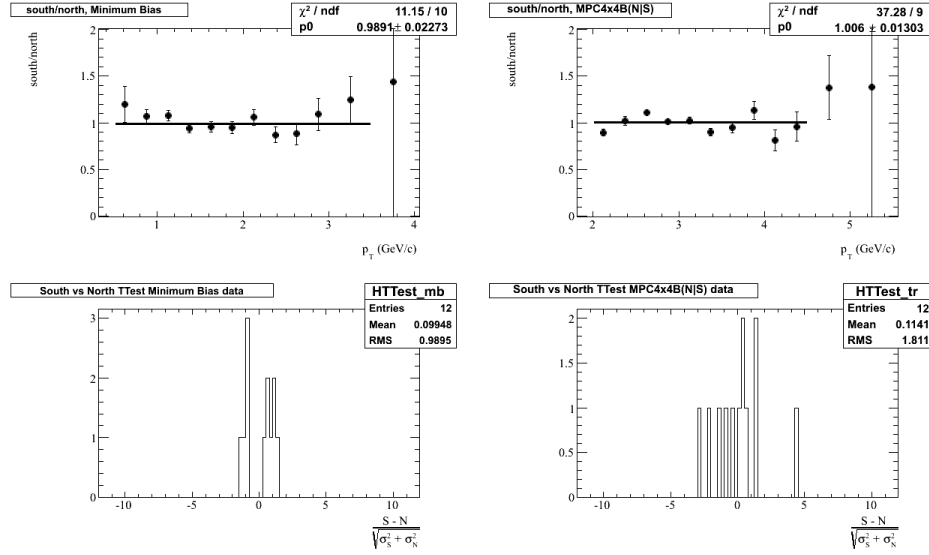


Figure 4.38: The ratios and T-test of the South and North MPC of  $\eta$  meson cross section from Fig. 4.37

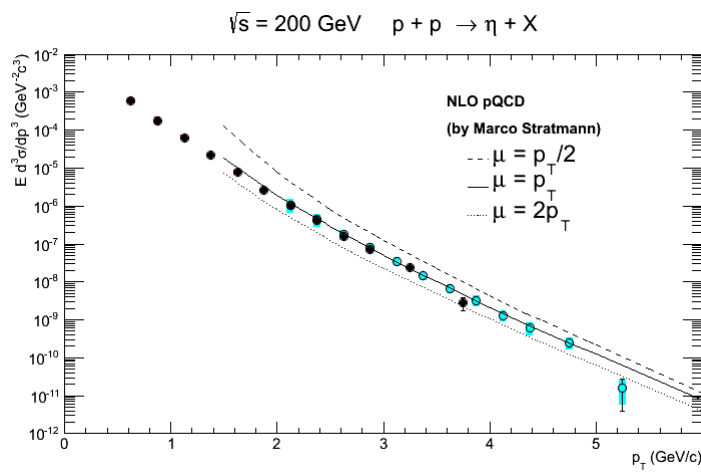


Figure 4.39: The  $\eta$  meson cross section. The systematic errors are shown as red(blue) bands around the cross section value for Minimum Bias ( $4 \times 4B$ ) cross section points. The red bands are small enough to be hidden behind the points. The black curves represent the NLO pQCD calculation provided by Marco Stratmann [91] for factorization scales  $\mu = p_T$  (solid),  $\mu = p_T/2$  (dashed), and  $\mu = 2p_T$  (dotted).

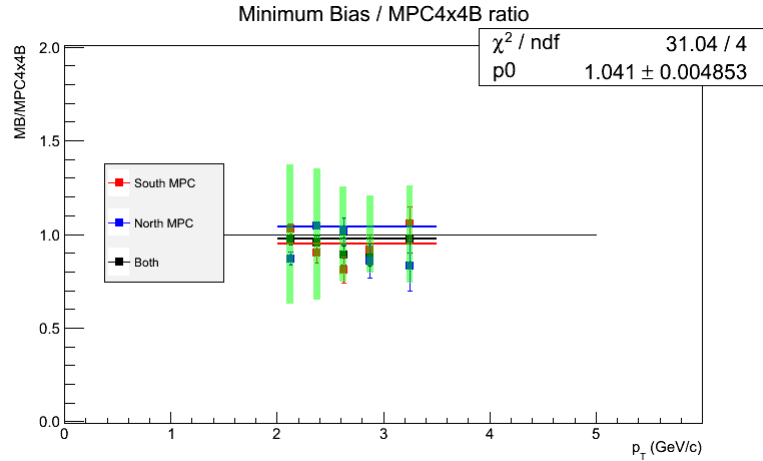


Figure 4.40: The Minimum Bias and  $4 \times 4$ B cross section comparison. The red (blue) points represent the ratio of the Minimum Bias to  $4 \times 4$ B cross section for the South (North) MPC, and black is the combined comparison. The green bands represent the systematic error from the Yield extraction and  $4 \times 4$ B trigger efficiency outlined in Sections 4.6.2 and 4.6.5. The cross section agree very well in the overlap region.

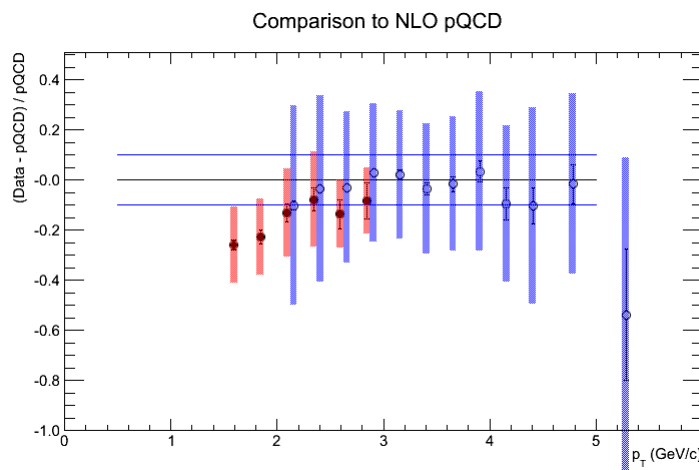


Figure 4.41: The comparison of the cross section points to NLO pQCD,  $\mu = p_T$ . The red (blue) error bands represent the systematic error on the Minimum Bias ( $4 \times 4$ B) cross section points. The NLO pQCD shows good agreement with the measured cross section within systematic error.

## Chapter 5

# The measurement of $\eta$ meson $A_N$

In polarized  $p^\uparrow + p$ , the cross section of hadrons is modified in azimuth, with respect to the polarization direction. In transversely polarized beams, the beams are polarized perpendicular to the beam momentum and are aligned vertically (along the  $y$ -direction) within the PHENIX coordinate system. To first order the azimuthally dependent cross section can be written as

$$\frac{d\sigma}{d\Omega} = \left( \frac{d\sigma}{d\Omega} \right)_0 (1 + P_y \cdot A_N \cdot \cos \phi) \quad (5.1)$$

where  $\left( \frac{d\sigma}{d\Omega} \right)_0$  is the unpolarized differential cross section,  $P_y$  is the vertical beam polarization, and  $A_N$  is the analyzing power. The azimuthal angle,  $\phi$ , is defined such that  $\phi=0$  is along the positive  $x$ -direction. Thus, the measured single spin asymmetries are a result of polarized scattering processes that have an analyzing power<sup>1</sup>,  $A_N$ . This dependence can be measured as

$$P_y \cdot A_N \cdot \cos \phi = \epsilon(\phi) \quad (5.2)$$

---

<sup>1</sup>More formally, the analyzing power is introduced in the scattering amplitude and density matrices formalism due to the non-zero polarization. See [92]

where  $\epsilon(\phi)$  is the measured raw asymmetry, which first order is an azimuthal cosine modulation. In the case where the transverse polarization known, the analyzing power,  $A_N$ , is the transverse single spin asymmetry.

The transverse single spin asymmetry,  $A_N$ , is determined using much of the same methodology as that was used for the cross section measurement in the previous chapter. Both measurements use the same RHIC 2008 dataset of  $p + p$  collisions at  $\sqrt{s} = 200$  GeV, the same Minimum Bias and  $4 \times 4B$  triggers, and the same  $\eta$  identification techniques. There are a few differences in the quality assurance checks, which will be defined in Section 5.4.

The  $A_N$  measurement takes advantage of the transversely polarized beams at RHIC,  $p^\uparrow + p^\uparrow$ . The spin direction of both beams alternates bunch to bunch, with four bunch patterns used in 2008, see Fig. 5.1. Varying the spin direction bunch-to-bunch and changing the fill pattern minimizes potential time-dependent and spin-dependent systematic errors, especially those related to the relative luminosity<sup>2</sup> and polarization.

To measure  $A_N$ , the polarization and spin information of only one beam is used, while the other beam's spin information is ignored, such that it is averaged over to a net polarization of zero. As one chooses which beam to use as ‘polarized’, two independent  $A_N$  measurements can be made: one utilizing the blue beam's polarization, and one utilizing the yellow beam's polarization. Effectively, as the South and North MPC detectors are independent with differing systematics, two independent measures of  $A_N$  are derived, suppressing the systematic uncertainty on the results. This is a significant advantage over the same measurements made by both the E704 and STAR, discussed in Section 2.4.

---

<sup>2</sup>Relative Luminosity is defined as  $\mathcal{R} = \frac{\mathcal{L}_\uparrow}{\mathcal{L}_\downarrow}$ . It describes the difference in the sampled number of inelastic collisions  $p^\uparrow + p$  versus  $p^\downarrow + p$ . Varying the spin direction bunch to bunch constrains  $\mathcal{R} \rightarrow 1$ .

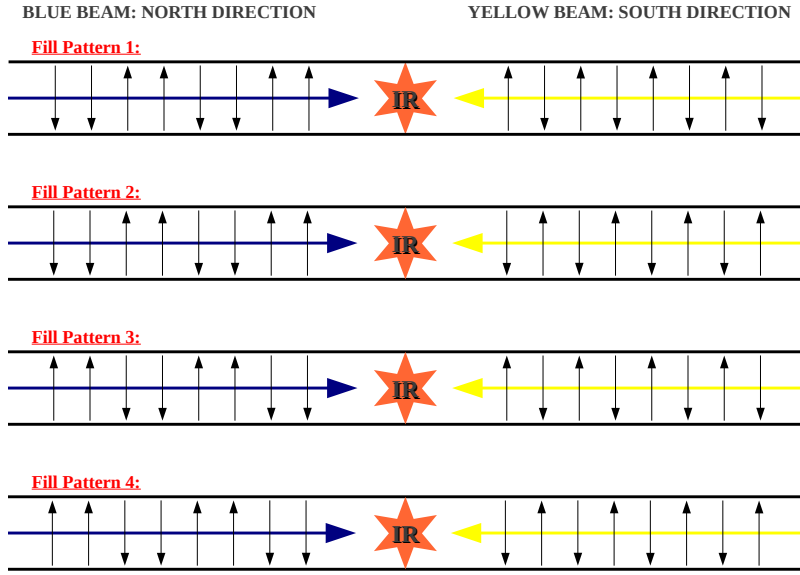


Figure 5.1: The four different fill patterns used at RHIC during the 2008 Run. The spin direction of the bunches in the blue beam changes every other bunch. The spin direction of the bunches in the yellow beam changes every bunch.

## 5.1 Kinematic Dependence of $A_N$

The measurement of  $A_N$  will be made as a function of  $p_T$  and  $x_F$ . The  $p_T$  dependence of  $A_N$  is made to check for twist-3 effects mentioned in Section 2.3.4. The  $x_F$  dependence of  $A_N$  is made because at forward rapidity, the collision involves a parton with high momentum fraction ( $x_1$ ) scattering with a parton with a low momentum fraction ( $x_2$ ).  $x_F$  is proportional approximately to the polarized parton momentum

$$x_F = 2 \frac{p_L}{\sqrt{s}} \approx 2 \frac{\langle z \rangle p_{jet}}{\sqrt{s}} \approx \langle z \rangle x_1 \quad (5.3)$$

The measurement is made for both forward going (positive)  $x_F$  and backward going (negative)  $x_F$ . Forward going  $x_F$  is related to the  $x_1$  of the parton from the polarized proton in the  $p^\uparrow + p$  collision, thus asymmetries dependent on interactions with this

parton directly access transverse spin effects. Backward going  $x_F$  is related the  $x_1$  of the parton from the unpolarized proton, thus asymmetries dependent on interactions with this parton are less dependent of any transverse spin effects and are expected to be  $x_F \approx 0$ .

The Minimum Bias triggered dataset allows the measurement of  $A_N$  as a function of  $p_T$  in the low  $p_T$  region of  $1.0 < p_T < 2$  GeV/ $c$ , which is extended to  $2.0 < p_T < 4.5$  GeV/ $c$  using the  $4 \times 4$ B triggered dataset. For the measurement of  $A_N$  as a function of  $x_F$  the Minimum Bias triggered dataset covers the region of  $0.2 < x_F < 0.4$ , and is extended to  $0.3 < x_F < 0.7$  using the  $4 \times 4$ B triggered dataset.

## 5.2 Formulae for Measuring $A_N$

The transverse single spin asymmetry,  $A_N$ , is measured in the MPC via:

$$A_N \cos(\phi) = \frac{1}{P_y} \epsilon(\phi) \quad (5.4)$$

where  $\epsilon(\phi)$  is the raw asymmetry, which to first order (see Eq. 5.2) has an azimuthal cosine modulation, and  $P_y$  is the vertical beam polarization. For this analysis,  $A_N$  is found by first measuring the raw asymmetry, fitting it with a cosine function, and then dividing by the average beam polarization. The amplitude of the cosine function divided by the beam polarization is  $A_N$ . The raw asymmetry can be measured several ways, see [93]. This analysis uses two methods. The first method is the so-called *square-root* formula

$$\epsilon_{sqrt}(\phi) = \frac{\sqrt{N^\uparrow(\phi) \cdot N^\downarrow(\phi + \pi)} - \sqrt{N^\downarrow(\phi) \cdot N^\uparrow(\phi + \pi)}}{\sqrt{N^\uparrow(\phi) \cdot N^\downarrow(\phi + \pi)} + \sqrt{N^\downarrow(\phi) \cdot N^\uparrow(\phi + \pi)}} \quad (5.5)$$

which uses the geometric mean of the yields  $N$  from two azimuthal regions on opposite sides of the MPC ( $\phi$  and  $\phi+\pi$ ) and two polarization directions (up –  $\uparrow$  and down –  $\downarrow$ ). When there is little loss of acceptance, particularly dead areas in azimuthal space, this method is advantageous as relative luminosity effects can be ignored.

A second method is the *polarization* formula

$$\epsilon_{pol}(\phi) = \frac{N^{\uparrow}(\phi) - N^{\downarrow}(\phi)}{N^{\uparrow}(\phi) + N^{\downarrow}(\phi)} \quad (5.6)$$

which uses two different polarization yields (up -  $\uparrow$  and down -  $\downarrow$ ) in one azimuthal region. This method is preferred if the acceptance is not homogeneous, but relative luminosity effects must be taken into account.

To measure the cosine modulation of  $A_N$ , the MPC is divided into twelve azimuthal bins, and spin dependent  $\eta$  meson yields are obtained for each bin. These yields are procured over the entire RHIC 2008 run, integrating over all 47 RHIC fills. The asymmetry is then simply calculated from Eqs. 5.5 and 5.6. Note that the square-root asymmetry (Eq. 5.5) leads to six points, since bins on opposite sides of the MPC are folded into each other, while the polarization (Eq. 5.6) asymmetry retains the original twelve bins, as the calculation is calculated bin by bin. The resultant asymmetries are then fit with a cosine function. As mentioned, the amplitude of the cosine function, divided by the fill-by-fill mean beam polarization (see Section 5.3) gives the value of  $A_N$ .

### 5.3 Beam Polarization

The beam polarization is found by taking the luminosity weighted average of the polarizations of the 47 RHIC fills used

$$P_{tot} = \frac{\sum_{fill} L_{fill} \cdot P_{fill}}{\sum_{fill} L_{fill}} \quad (5.7)$$

For the 2008 run at RHIC, the average transverse beam polarization of the blue (yellow) beam was  $49.0 \pm 1.7\%$  ( $42.0 \pm 1.5\%$ ).

The beams are transversely polarized in the vertical  $y$ -direction. A study performed using the local polarimeter (see Section 3.1.6), showed that the blue beam was off-vertical by  $\phi_{blue} = 0.24 \pm 0.03(\text{stat.})^{+0.111}_{-0.069}(\text{syst.})$  radians during the 2008 RHIC run [94]. This is taken into account for the  $A_N$  measurements using the blue beam by adjusting blue beam measurements by  $\phi = \phi_{meas} + \phi_{blue}$ .

## 5.4 Quality Assurance

### 5.4.1 Warnmap

The same basic warnmap used for cross section measurement, mentioned in Section 4.1.1 is used for the  $A_N$  measurement. However, due to the nature of the asymmetry measurements, the towers previously removed due to the noisy driver board are now allowed. As the  $\eta$  meson yields are extracted above  $p_T > 1.0$  GeV/ $c$ , and since efficiency corrections are not needed in the asymmetry calculation, these towers have a suppressed effect on the yield extraction and can be used in the calculation of the asymmetry. This is advantageous as removing them would cause additional acceptance issues in the asymmetry calculation using Eq. 5.5. The final warnmaps are shown in Figs. 5.2 and 5.3.

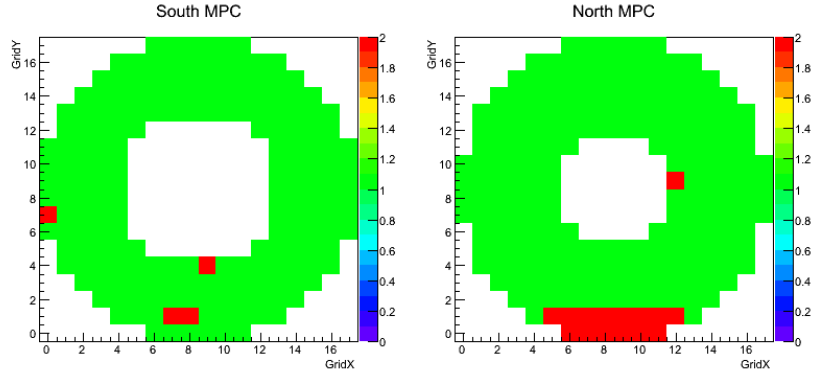


Figure 5.2: Warnmap used for Minimum Bias triggered dataset for the  $A_N$  measurement. The left (right) panel shows the South (North) MPC warnmap. Clusters which have their primary tower position in red are removed from the analysis.

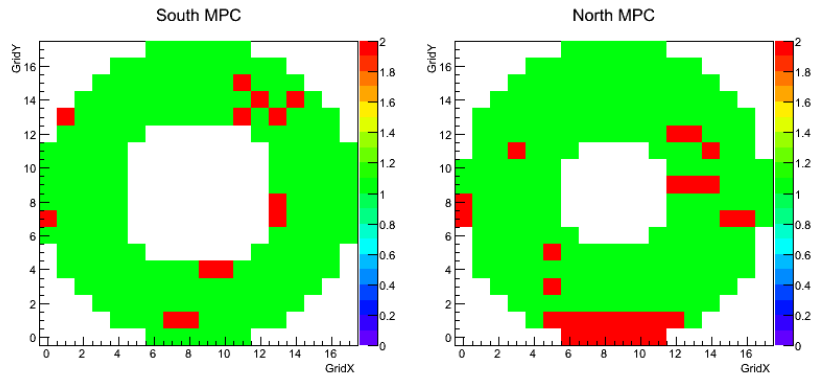


Figure 5.3: Warnmap used for  $4 \times 4B$  triggered dataset for the  $A_N$  measurement. The left (right) panel shows the South (North) MPC warnmap. Clusters which have their primary tower position in red are not used in this analysis.

### 5.4.2 Run Spin Information Quality Assurance

The run QA is the same as discussed in Section 4.1.2. A few additional runs are removed due to problems with the spin or polarization information recorded at run time. Runs with bad spin information are removed from the  $A_N$  measurement, but not the cross section measurement. Four runs were removed due to the bunches in the beam being radially polarized. Eight runs were removed due to having no official polarization. Sixteen runs were removed due to errors in retrieving the spin information from the PHENIX database. Out of the original 266 (254) PHENIX runs recorded, a total of 234 (223) runs are used for the Minimum Bias ( $4 \times 4B$ )  $A_N$  measurement.

## 5.5 Yield Extraction and Correction for Background Sources

To extract the  $\eta$  meson yields, an invariant mass spectra from all photon pairs is formed, independent of spin direction and  $\phi$ , and binned in  $x_F$  (or  $p_T$ ). The invariant mass spectra are then fit with a function with signal and background components (similar to Eq. 4.6), see Fig. 5.4.

$$F(x) = F(x, a, \gamma, \mu, \beta) + g_\eta(x, N_\eta, M_\eta, \sigma_\eta) + g_\omega(x, N_\omega, M_\omega, \sigma_\omega) \quad (5.8)$$

where  $a$ ,  $\gamma$ ,  $\mu$ , and  $\beta$  are fit parameters for the background Gamma Distribution Function,  $M_\eta$  and  $\sigma_\eta$  are the mass value and width, respectively of the  $\eta$  meson peak, and  $M_\omega$  and  $\sigma_\omega$  are the mass value and width, respectively of the  $\omega$  meson<sup>3</sup> peak at higher

---

<sup>3</sup>see upcoming Section 5.5.2 for a discussion of the presence of the  $\omega$  meson

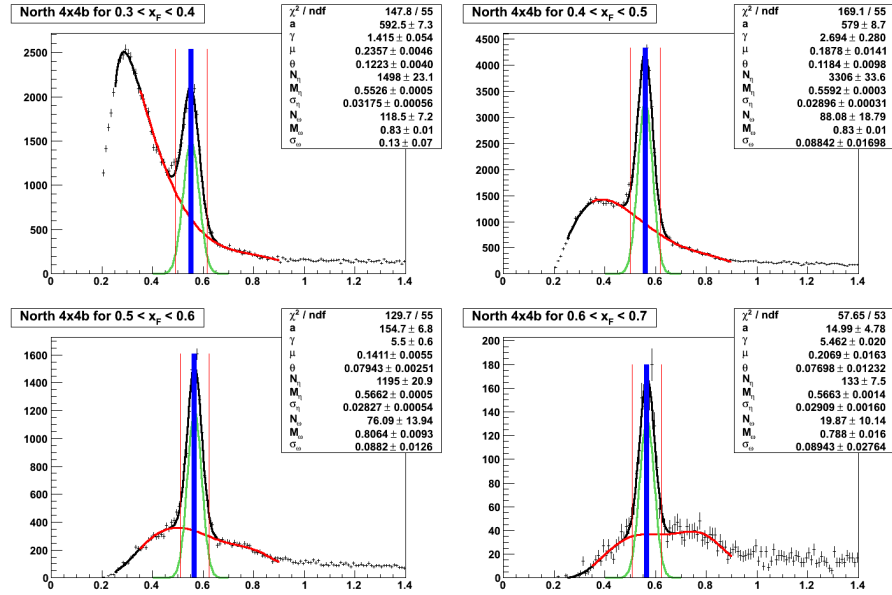


Figure 5.4: Extraction of  $\eta$  meson mass range for each  $x_F$  bin. The vertical red lines establish the  $\eta$  meson peak,  $M_\eta \pm 2\sigma_\eta$ .

invariant mass than the  $\eta$  meson.

The spin dependent and  $\phi$  dependent invariant mass spectra are then formed, with the spin and  $\phi$  dependent yields determined by integrating the invariant mass spectrum between  $M \pm 2\sigma$ , such that  $N^{\uparrow(\downarrow)}(\phi_i) = N_{M \pm 2\sigma}$ .

The South MPC spin dependent invariant mass spectra for  $0.4 < x_F < 0.5$ , binned in  $\phi$  are shown in Fig. 5.5. In these figures, the Yellow beam is vertically polarized. The yield extracted from each spectrum is obtained by integrating between the vertical red lines,  $N^{\uparrow}(\phi_i) = N_{M \pm 2\sigma}$ .

### 5.5.1 Asymmetry in the Background Regions

Once the spin and  $\phi$  dependent yields are obtained, the asymmetry in the  $\eta$  meson peak region can be calculated,  $A_N^{\text{peak}}$ . Since there remains a background under the  $\eta$  mass region, however, the final measurement of  $A_N$  must be corrected for dilution due

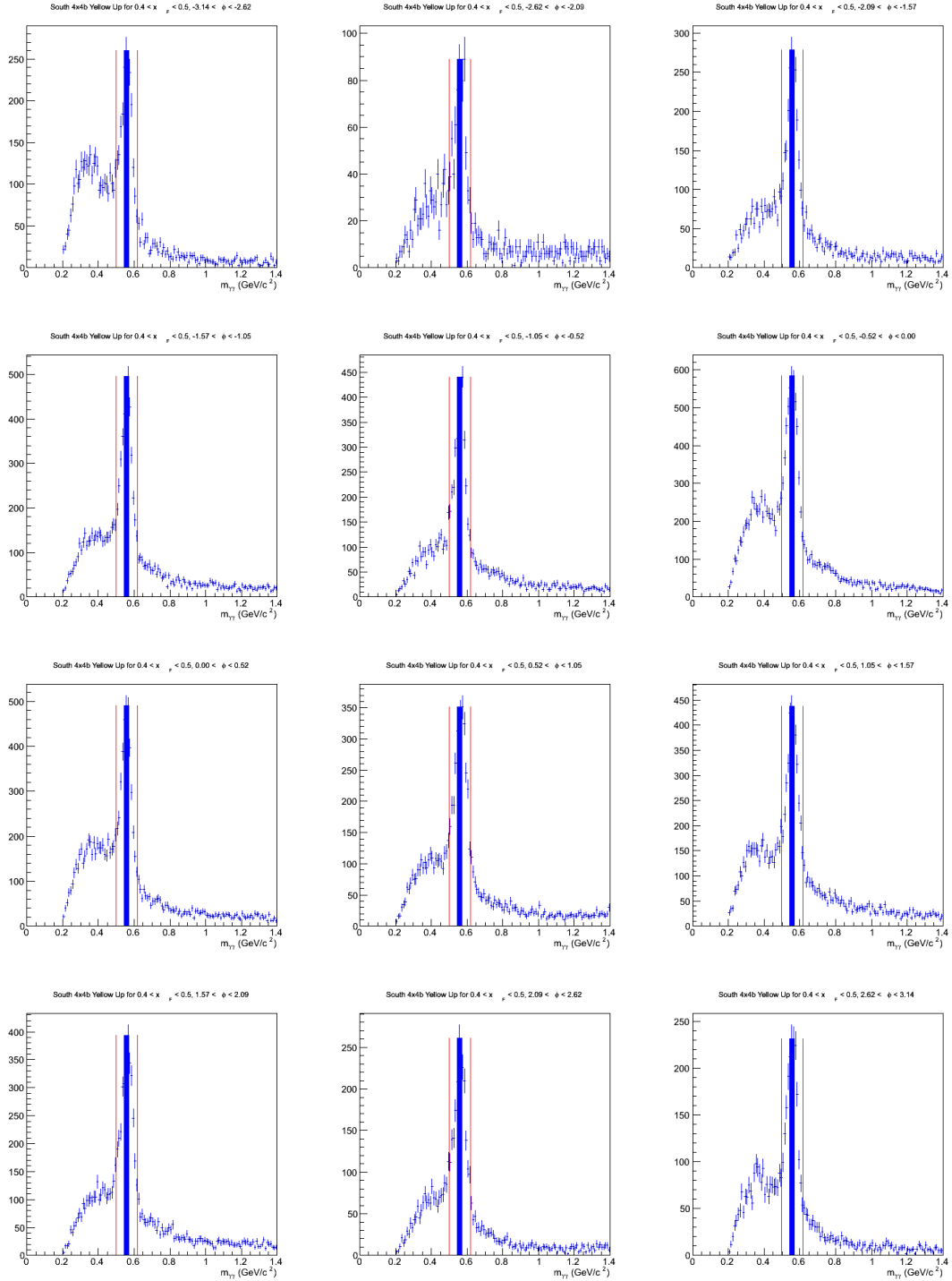


Figure 5.5: The North MPC spin dependent invariant mass spectra for  $0.4 < x_F < 0.5$ , binned in  $\phi$  for positive Yellow beam polarization. The yield is extracted from each spectra by integrating between the vertical red lines,  $N^\uparrow(\phi_i) = N_{M \pm 2\sigma}$

	$0.3 < x_F < 0.4$	$0.4 < x_F < 0.5$	$0.5 < x_F < 0.6$	$0.6 < x_F < 0.7$
South 4x4b(N S)	0.45	0.36	0.37	0.38
North 4x4b(N S)	0.44	0.34	0.33	0.34
	$0.2 < x_F < 0.3$	$0.3 < x_F < 0.4$		
South Minbias	0.71	0.56		
North Minbias	0.67	0.45		

Table 5.1:  $r$  values for the various  $x_F$  bins.

to this background. This correction to the asymmetry is obtained from the asymmetry measured from a combined mass region from the left ( $-5\sigma < m_{inv} < -3\sigma$  GeV/ $c^2$ ) and right ( $3\sigma < m_{inv} < 5\sigma$  GeV/ $c^2$ ) of the  $\eta$  meson mass peak, as shown in Fig. 5.6. The final background corrected  $\eta$  meson asymmetry is defined as

$$A_N^\eta = \frac{A_N^{peak} - r A_N^{bg}}{1 - r} \quad (5.9)$$

where  $r = \frac{N_{BG}}{N_{BG} + N_\eta}$  in the  $\eta$  peak region,  $A_N^{peak}$  is the measured asymmetry the peak region, and  $A_N^{bg}$  is the measured asymmetry of the background. The  $r$  values are found from the spin-independent mass spectra fits (Fig. 5.4) using Eq. 5.8. The integral of  $(F + g_\omega)$  represents  $N_{BG}$  in the  $\eta$  mass region, and the integral of  $g_\eta$  in the  $\eta$  mass region yields  $N_\eta$ . The  $\eta$  mass region is defined as  $2\sigma$  around the mean peak position. The values of  $r$  are given in Table 5.1.

This background correction must be made to the  $A_N$  because the background under the  $\eta$  meson peak may be made of particles that have a different asymmetry to the signal from the  $\eta$  meson. For example the asymmetry measured from neutral pions have been shown to be non-zero, as discussed in Section 2.3. To understand the make up of the background, a simulation study is done, which is discussed in Section 5.5.2..

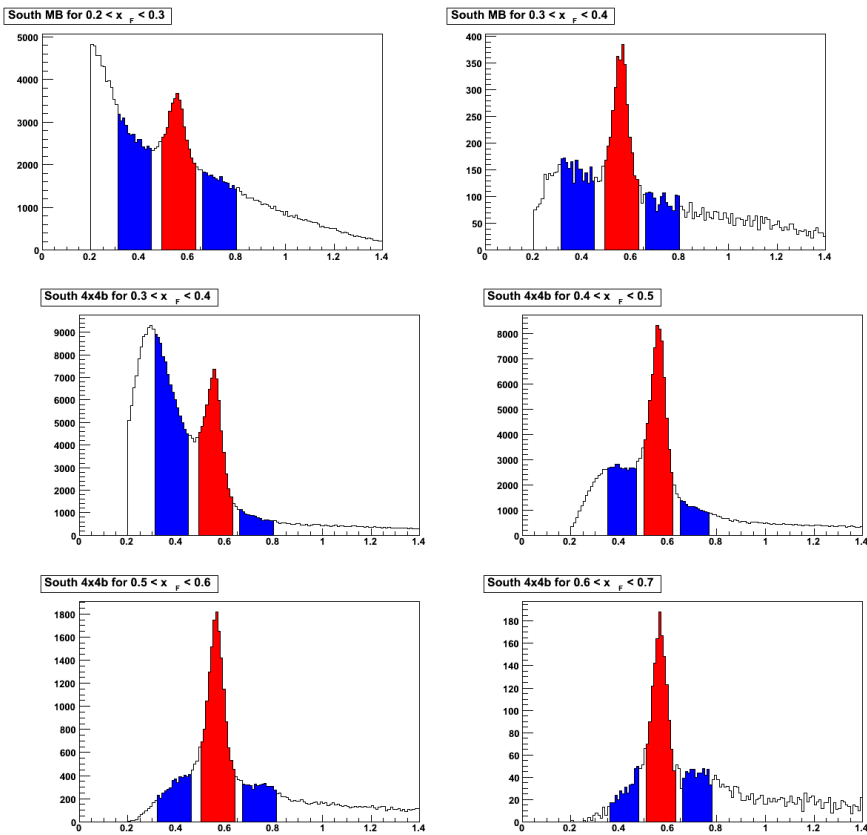


Figure 5.6: Invariant mass spectra for the South MPC, illustrating the  $\eta$  meson peak region (red), as well as the side band regions (blue) for each  $x_F$  bin in the Minimum Bias (top row) and 4×4B triggered dataset (center, bottom row).

### 5.5.2 Simulation Studies of Correlated Background

In order to understand the components of correlated background under the  $\eta$  meson peak, a simulation study was performed. Inelastic  $p+p$  collisions at  $\sqrt{s} = 200$  GeV were simulated using Pythia [86] events passed through a full GEANT [87] description of the PHENIX detector. Only Pythia Events with at least one cluster  $E_{cl} = 15$  GeV were passed through the GEANT software to simulate the  $4 \times 4B$  trigger. The goal of this simulation study was to understand what particles contribute to the invariant mass pairs in the  $4 \times 4B$  triggered dataset by identifying the dominant and the first contributing (if necessary) particle type(s) that contribute to the cluster. The parent particle (from Pythia) is then traced to each cluster. Identifying the particles which contribute to clusters is necessary because we expect a portion of the background to be due to a correlated jet background comprising photons from  $\pi^0$ s.

For a contributing particle to be considered in a cluster, it must deposit at least 50% of its energy in the cluster, and the amount of deposited energy must be greater than 1.0 GeV. If this criterion is met for a contributing particle, these clusters are identified as follows:

- Merged  $\pi^0$ . The dominant and contributing particle have the same parent, a  $\pi^0$ . Thus, this is a merged  $\pi^0$
- $\pi^0 + \text{something}$ . The dominant particle is a photon from a  $\pi^0$ , the contributing particle has a different parent. Usually ( $> 90\%$ ), the contributing particle is a photon with a separate  $\pi^0$  parent.
- Something merged. The dominant particle parent is not from a  $\pi^0$ . Usually ( $> 90\%$ ), the contributing particle is a photon with a separate  $\pi^0$  parent.

If the contributing particle does not meet the criterion mentioned above, only the dominant particle parent is considered

- Single  $\pi^0$  meson. The cluster is a photon from a  $\pi^0$ .
- $\eta$  meson. The cluster is a photon from an  $\eta$  meson.
- $\omega$  meson. The cluster is a photon from a  $\omega$  meson.
- direct photon.
- charged pions.
- electron.
- (anti)proton.
- (anti)neutron.
- some other particle.

Figure 5.7 shows the result of the study. The total distribution (red) includes contribution from all types of original cluster parent. Both clusters forming an invariant mass pair are checked for each parent type. The combinatorial background is dominated by single photons from  $\pi^0$  (magenta). Photons, electrons, protons, neutrons, and other particles contribute very little in comparison to the combinatorial background, and charged pions (purple) produce a small linear contribution. Merging  $\pi^0$  (cyan and forest green) have a combined moderate effect at low invariant mass, similarly photons decaying from the  $\omega$  meson (indigo) have an effect at high invariant mass, above the  $\eta$  meson range. With this in mind, the need for the background correction to the asymmetries of the  $\eta$  meson becomes obvious, since pions (di- $\gamma$  and merged  $\pi^0$  mesons and charged pions) are expected to have a zero to finite asymmetry, and the  $\omega$  contribution could also have a

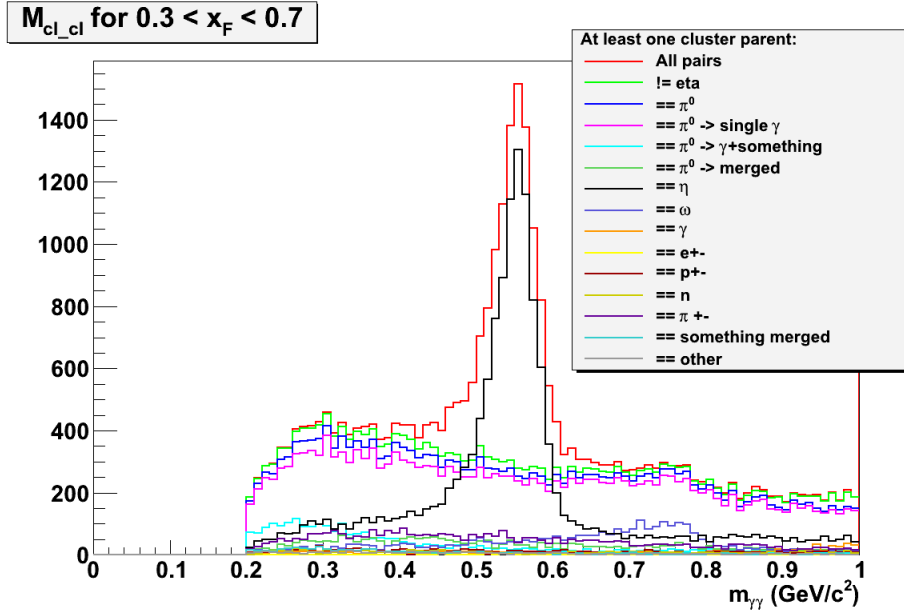


Figure 5.7: Decomposition of cluster parents contributing to the invariant mass distribution in the  $\eta$  mass range. Note that the blue line representing  $\pi^0$  parents is the sum of the magenta, cyan, and forest green curves.

finite asymmetry. From this study, both are expected to contribute to the background under the  $\eta$  mass peak.

## 5.6 Obtaining the Asymmetry

The final step to determine the raw asymmetries is to fit the  $\phi$ -dependence with a cosine function for both the  $\epsilon_{pol}$  and  $\epsilon_{sqrt}$  asymmetries. Two cosine-function fits are performed for each of the azimuthal distributions, one being a pure cosine function ( $\phi_0 = 0$ ), and the other using a free phase  $\varphi_0$

$$f(\varphi) = a \cdot \cos(\varphi + \varphi_0) \quad (5.10)$$

The free phase is added to check for deviations of the beam polarization from the vertical direction. A similar study found that the blue beam was off vertical by 0.24 radians,

mentioned in Section 5.3. For the polarization method, an additional constant term is added to account for relative luminosity effects that could deviate from  $\mathcal{R} = 1$ .

$$f(\varphi) = b_{r.l.} + a \cdot \cos(\varphi + \varphi_0) \quad (5.11)$$

### 5.6.1 Asymmetry in the $\eta$ Meson Peak Region

The calculated  $\epsilon_{sqrt}$  asymmetries in the  $\eta$ -peak region as a function of  $\phi$  are shown in Fig. 5.8 (5.9) for the South (North) MPC for each  $x_F$  bin. The left (right) column shows the results for negative (positive)  $x_F$ . The red curves show the result of a pure cosine fit ( $\phi_0 = 0$ ) as defined in Eq. 5.10. Figure 5.10 (5.11) show the  $\epsilon_{pol}$  asymmetry fits for the South (North) MPC. These data (as discussed in Section 5.2) have more points owing to the “folding” nature of the  $\epsilon_{sqrt}$  method. The blue curve represents the fits used using Eq. 5.11 for each  $x_F$  bin.

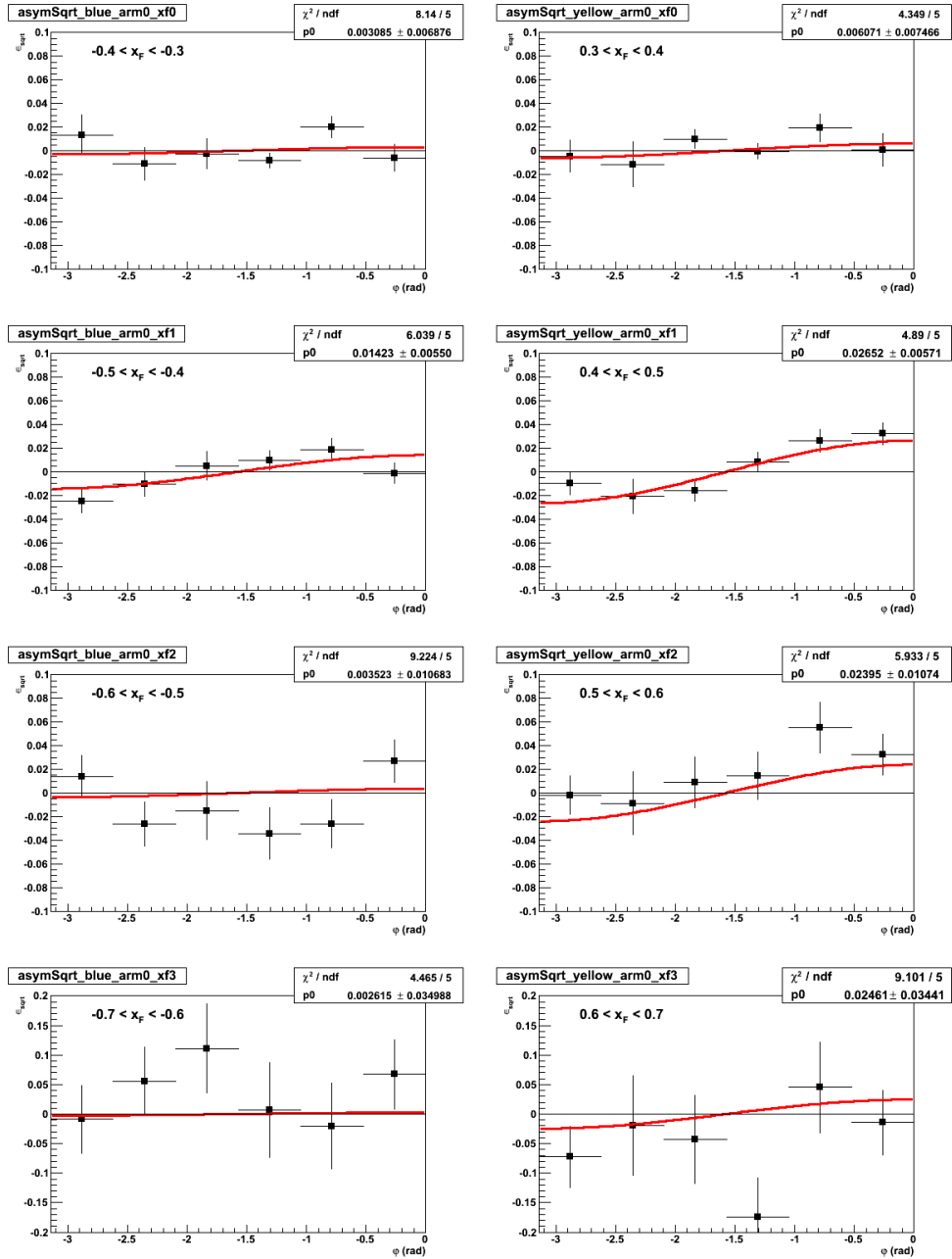


Figure 5.8:  $\epsilon_{\text{sqrt}}$  asymmetries for South MPC, in the  $\eta$  peak region. The left (right) column is negative (positive)  $x_F$ .

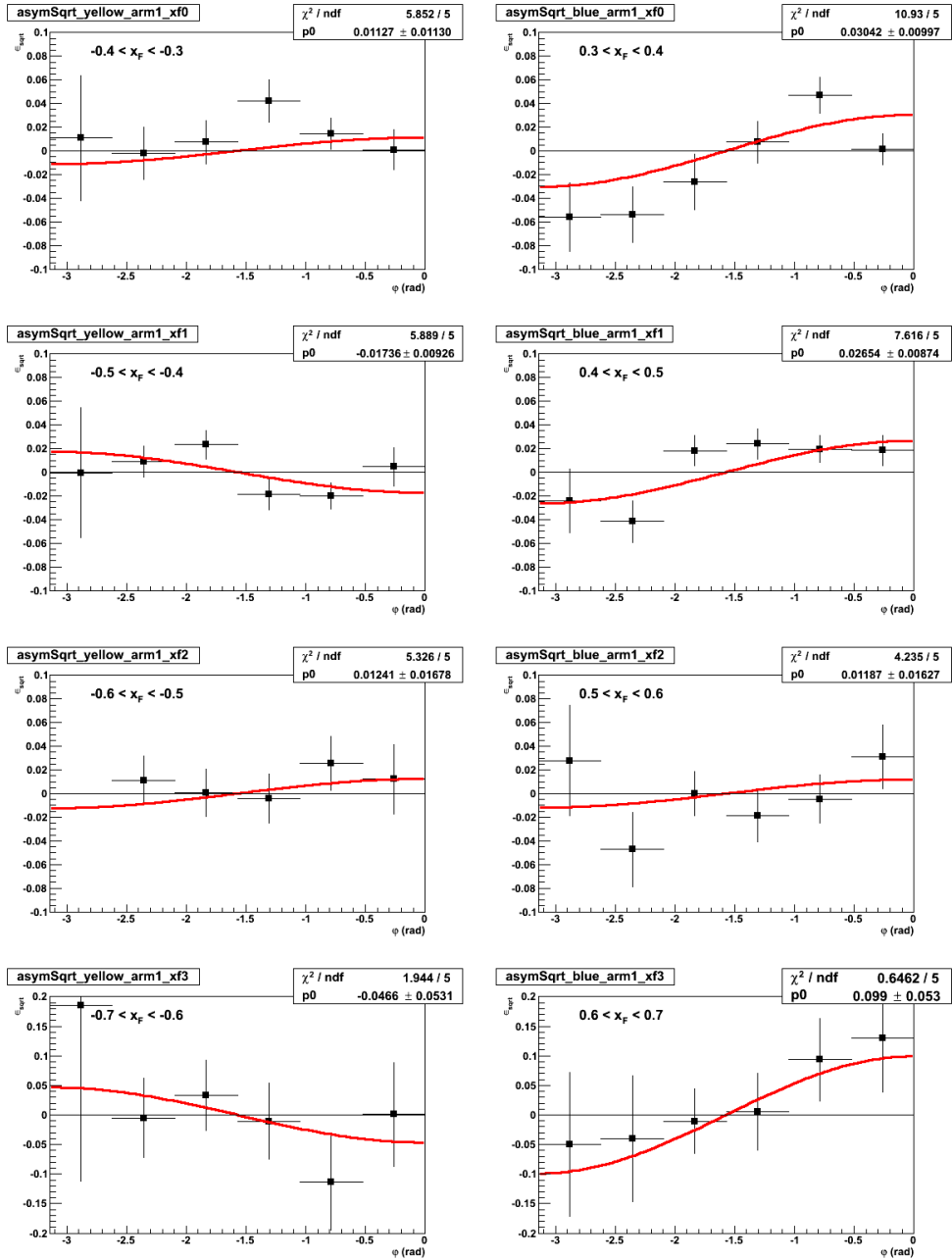


Figure 5.9:  $\epsilon_{sqrt}$  asymmetries for North MPC, in the  $\eta$  peak region. The left (right) column is negative (positive)  $x_F$ .

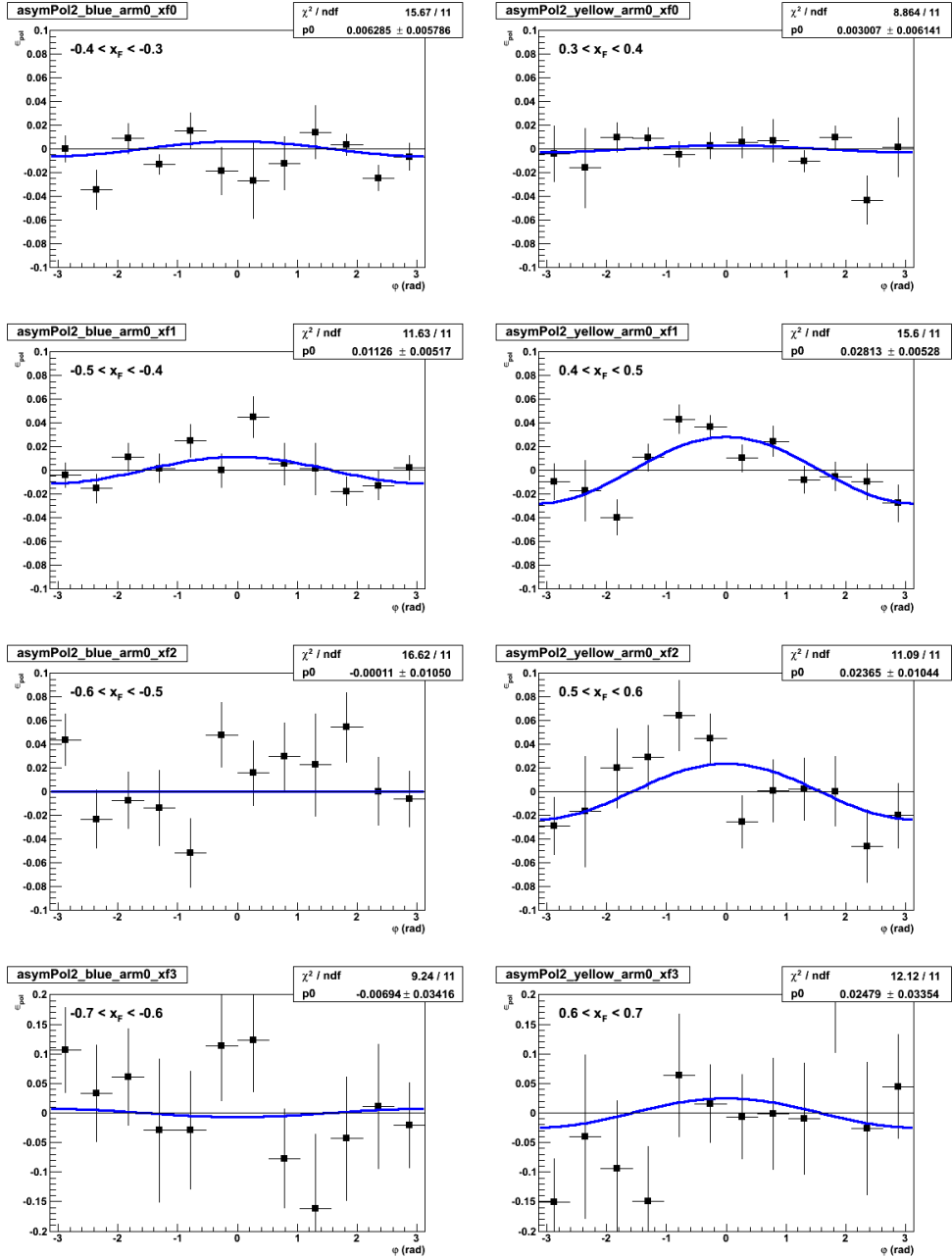


Figure 5.10:  $\epsilon_{pol}$  asymmetries for South MPC, in the  $\eta$  peak region. The left (right) column is negative (positive)  $x_F$ .

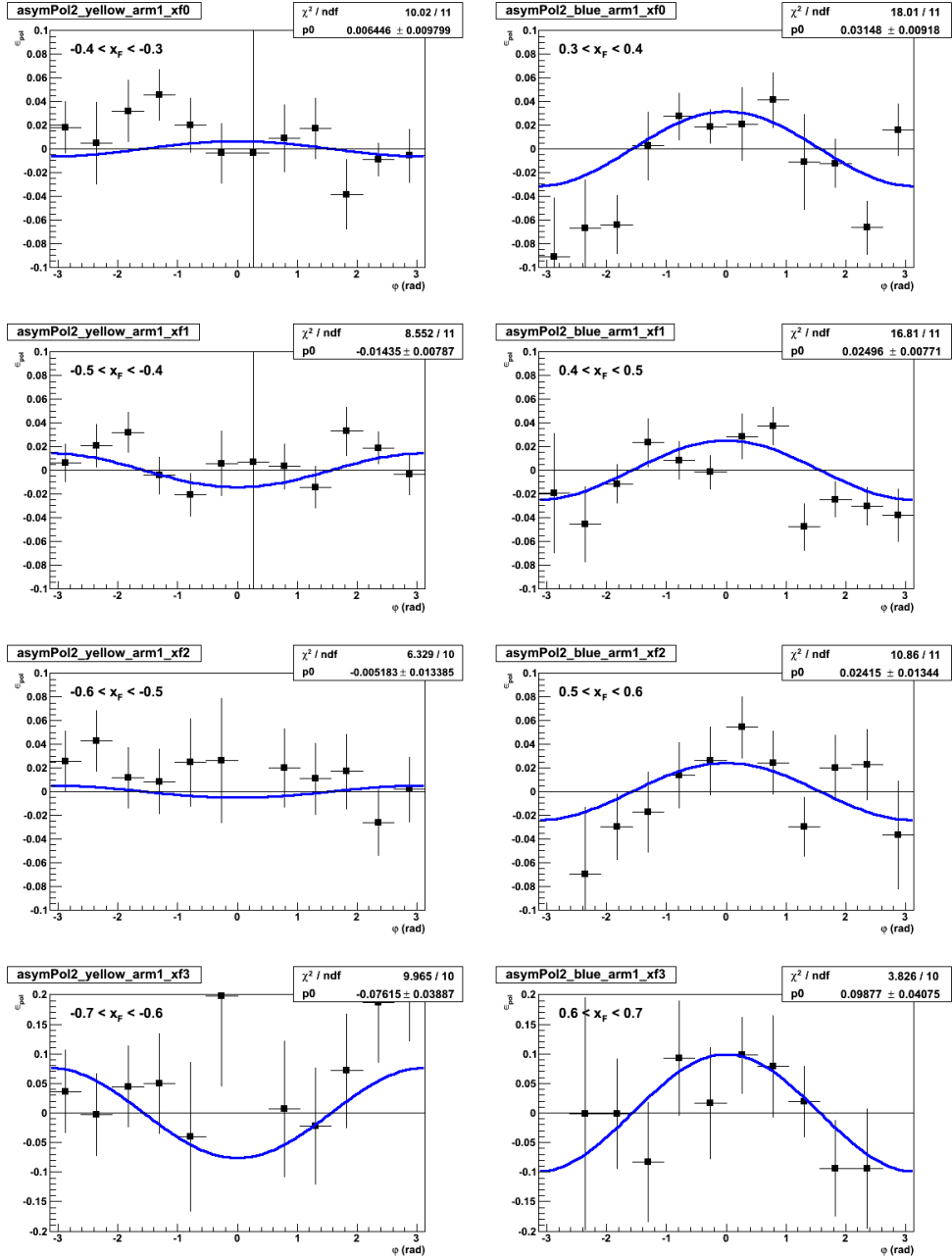


Figure 5.11:  $\epsilon_{pol}$  asymmetries for North MPC, in the  $\eta$  peak region. The left (right) column is negative (positive)  $x_F$ .

The fit parameters, extracted from Figs. 5.8 - 5.11, are summarized in Figs. 5.12 (South MPC) and 5.13 (North MPC). The top-left panel shows the value of the square-root (red) and polarization (green) asymmetries, fit both with (open symbols) and without (closed) a free phase  $\varphi_0$ . The points all agree within the shown statistical uncertainties. The right two figures are the values of the phase shifts  $\varphi_0$ , which across positive and negative  $x_F$  are averaged to within  $1\sigma$  of  $\phi=0$ —indication that our yellow beam is vertically polarized, and that the blue beam offset is set correctly to  $\phi_{blue}=0.24$  (see Section 5.3). The error bars are larger in the negative  $x_F$  values, as the asymmetry there is expected to be zero, so the free phase cannot be determined to a good accuracy.

The bottom-left panel shows a fit to the constant terms of the  $\epsilon_{pol}$  asymmetry fit from Eq. 5.11. The value of this fit gives the global value of the relative luminosity over the entire  $x_F$  range. The constant term is fit separately for negative and positive  $x_F$ , because they are calculated using the different beams. In the South (North) MPC, the negative points correspond to the blue (yellow) beam, and the positive points correspond to the yellow (blue) beam. The plots show a slight non-zero deviation on the order of 0.1%. This global value is subtracted from the azimuthal distributions, and the amplitude distributions are fit again without  $b_{r.l.}, \varphi_0$ .

Figure 5.14 shows the values of the final data fits of the asymmetries. Only the asymmetries with a fixed phase  $\varphi = 0^\circ$  are shown. The red points show the raw asymmetry for the  $\epsilon_{sqrt}$  asymmetries, and the green points show the  $\epsilon_{pol}$  asymmetries with individual relative luminosity terms for each  $x_F$  bin (Eq. 5.11 with  $\phi_0=0$ ). The blue points are for the  $\epsilon_{pol}$  asymmetries corrected for the global relative luminosity from each beam, determined from the fit above. These latter points are fit with Eq. 5.10 and  $\phi_0=0$ . The  $\epsilon_{pol}$  fit methods do not agree precisely as the relative luminosity components

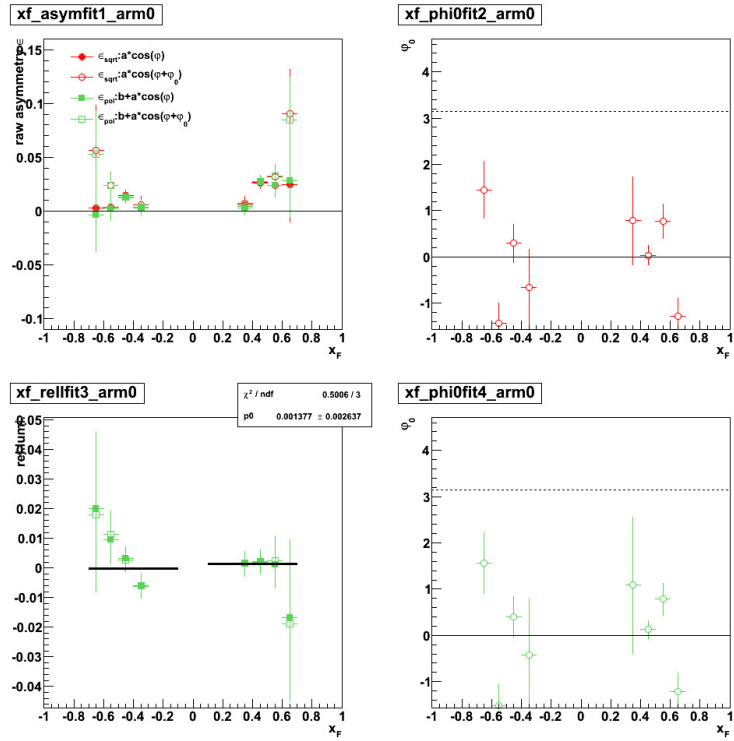


Figure 5.12: Plots summarizing the free phase fits from Eqs. 5.10 and 5.11 for the South MPC. See text for details.

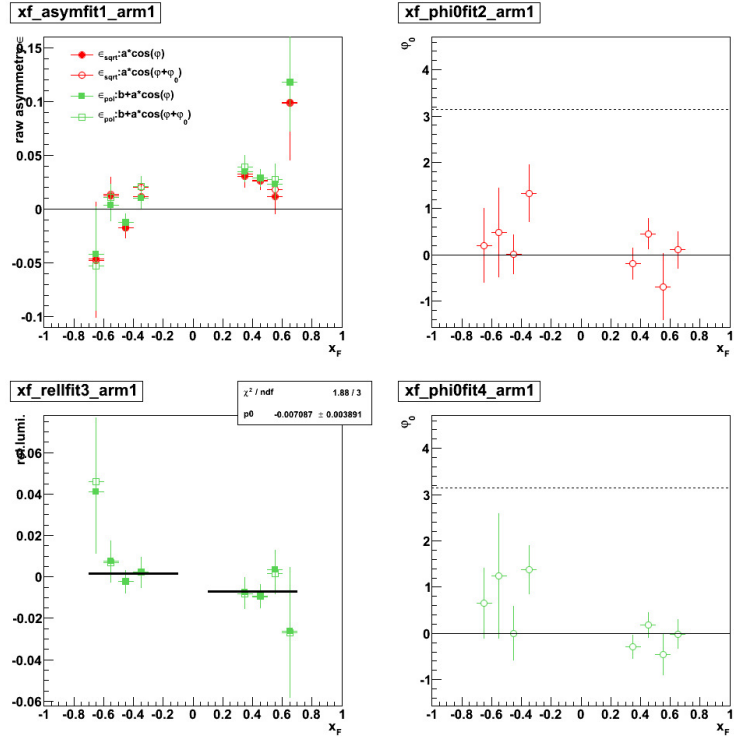


Figure 5.13: Plots summarizing the free phase fits from Eqs. 5.10 and 5.11 for the North MPC. See text for details.

effectively vary bin to bin in the fit, but should be constant across  $x_F$  for a given beam.

In general, there is good agreement between the methods. A systematic uncertainty was found to exist in separate  $\epsilon_{pol}$  asymmetry calculations made on even versus odd bunch crossings, and for the four different fill patterns (see Fig. 5.1). This is treated as a systematic error on the final asymmetry, discussed in Section 5.8.2.

For the central value of the measurement of  $A_N$ , the  $\epsilon_{sqrt}$  asymmetry is used. The bottom panels in Fig. 5.14 use Eq. 5.4 to calculate  $A_N^{peak}$  using  $\epsilon_{sqrt}$  and the values of  $P_{beam}$  given in Section 5.3. For the negative  $x_F$  bins, the blue (yellow) polarization value is used for the South (North) MPC, and for the positive  $x_F$  bins, the yellow (blue) polarization value is used for the South (North) MPC.

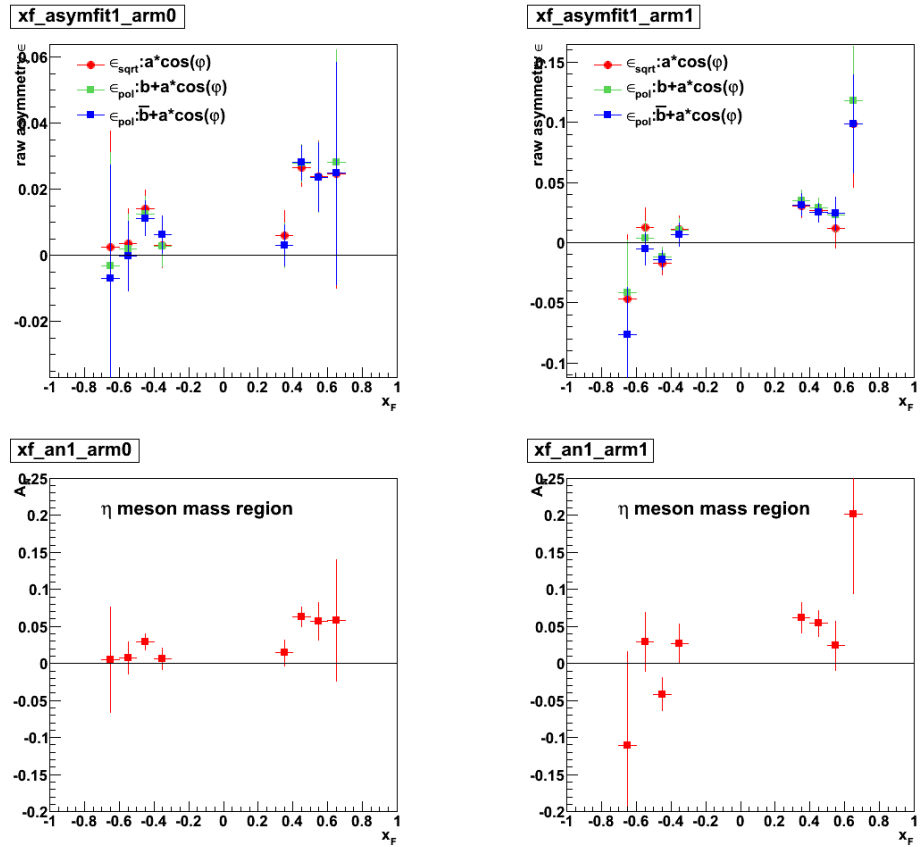


Figure 5.14: Asymmetries in the  $\eta$  mass region. The left (right) column is for the South (North) MPC. The top figure displays the raw asymmetry, and the square-root asymmetry (red points) in these figures are used to calculate  $A_N^{peak}$ , which is displayed in the bottom figure

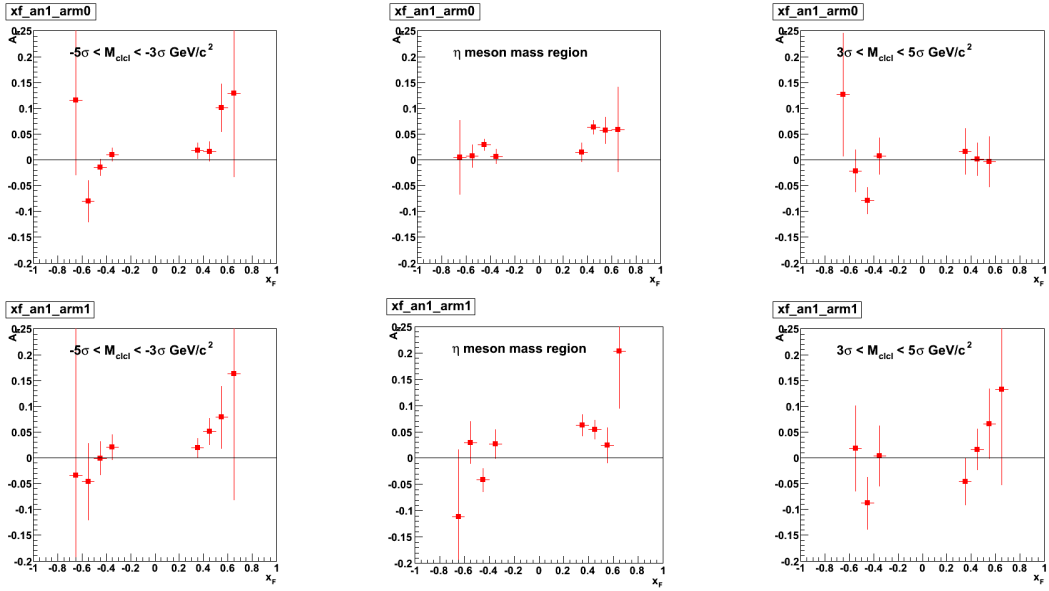


Figure 5.15:  $x_F$  Asymmetries in the different invariant mass regions. The top (bottom) row is for the South (North) MPC

### 5.6.2 Calculation of Background Asymmetry

The values of  $A_N^{peak}$  given in Fig. 5.14 must be corrected for background distribution discussed in Section 5.5.1. Figure 5.15 shows  $A_N$  in the invariant mass regions  $-5\sigma < M_{clcl} < -3\sigma$  GeV/ $c^2$  ( $A_N^{left}$ ), the  $\eta$  mass region ( $A_N^{peak}$ ), and  $3\sigma < M_{clcl} < 5\sigma$  GeV/ $c^2$  ( $A_N^{right}$ ). To find the value of  $A_N^{bg}$  in Eq. 5.9 the weighted mean of  $A_N^{left}$  and  $A_N^{right}$  is calculated for each  $x_F$  bin. Figure 5.16 shows the value of  $A_N^{bg}$  for each MPC. The red circle symbols represent the combined  $A_N^{bg}$ . The blue points to the immediate left and immediate right of each red symbol represent  $A_N^{left}$  and  $A_N^{right}$ , respectively.

### 5.6.3 Background Corrected $A_N$

Only a small fraction of the background asymmetry  $A_N^{bg}$  is subtracted from the peak asymmetry as the yield of “signal”  $\eta$  mesons outnumber the combinatorial background pedestal. The fraction, determined in Section 5.5.1 and shown in Table 5.1

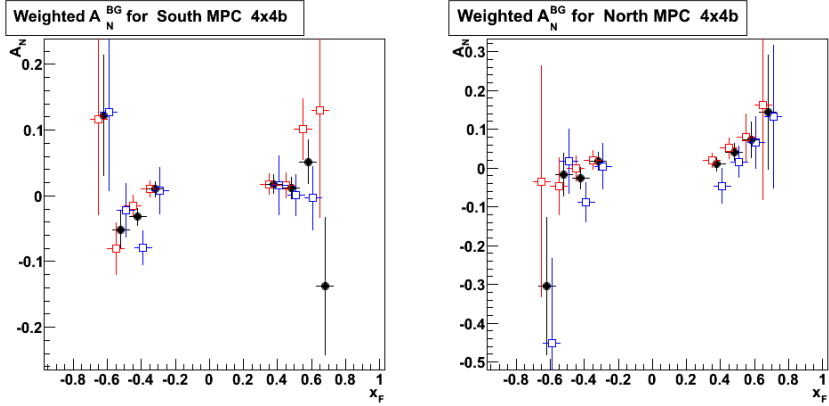


Figure 5.16: The measured background asymmetry,  $A_N^{bg}$ , shown as black points. The left (right) plot is for the South (North) MPC. Red (blue) symbols depict the  $A_N^{left}$  ( $A_N^{right}$ ) individual asymmetries.

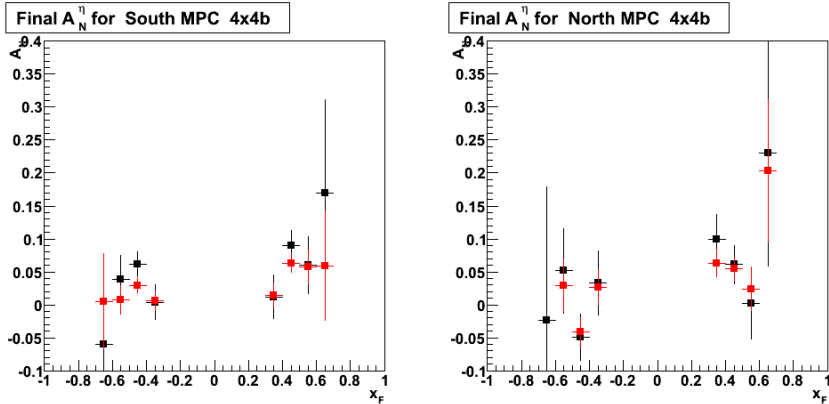


Figure 5.17: The background corrected values of  $A_N^\eta$  for the  $4 \times 4$ B triggered dataset. The left (right) plot is for the South (North) MPC. See text for details.

is used to derive the true  $\eta$  meson asymmetry (Eq. 5.9). Final corrected,  $A_N^\eta$  are shown in Figure 5.17 as black symbols. Red symbols depict the uncorrected  $A_N^{peak}$  asymmetry, diluted by the background. The asymmetry values for the different invariant mass regions are given in Tables B.1 and B.2 in the Appendix.

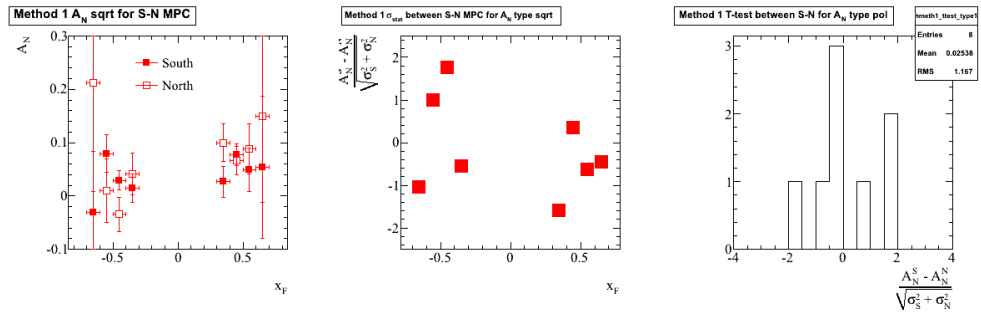


Figure 5.18: Statistical uncertainty checks between the South and North MPC in the  $4 \times 4B$  triggered dataset. In the left panel, the closed (open) points represent the South(North) MPC. The center panel calculate the statistical uncertainty between the North and South  $A_N$  values, and the right panel is the distribution of these values

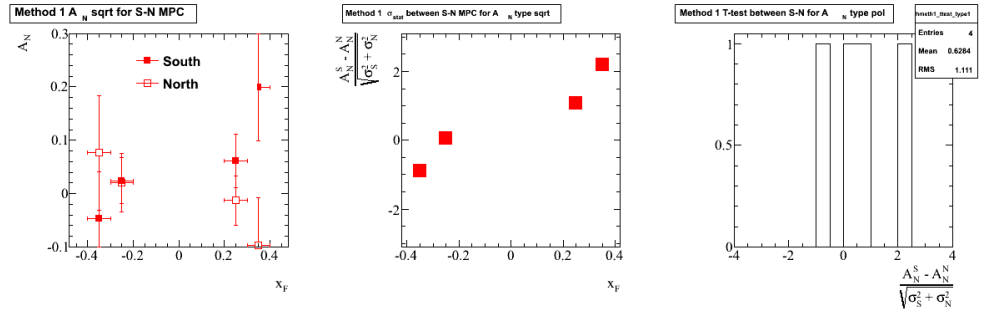


Figure 5.19: Statistical uncertainty checks between the South and North MPC in the Minimum Bias triggered dataset. In the left panel, the closed (open) points represent the South(North) MPC. The center panel calculate the statistical uncertainty between the North and South  $A_N$  values, and the right panel is the distribution of these values

#### 5.6.4 Comparison of South and North MPC $A_N$

The weighted mean of the South and North MPC  $A_N^\eta$  gives the final  $x_F$  dependence of  $A_N$ . The left panel in Fig. 5.18 shows the values of the South and North MPC. The center plot shows the statistical uncertainty between the South and North, while the right plot shows the T-test distribution of all these uncertainties.

The procedure to procure  $A_N$  from the Minimum Bias triggered dataset is the same as that in the  $4 \times 4B$  dataset. Figure 5.19 shows similar distributions for the Minimum Bias asymmetries, as shown for the  $4 \times 4B$  triggered dataset.

The combined South and North  $A_N$  is shown in Fig. 5.32, where the open

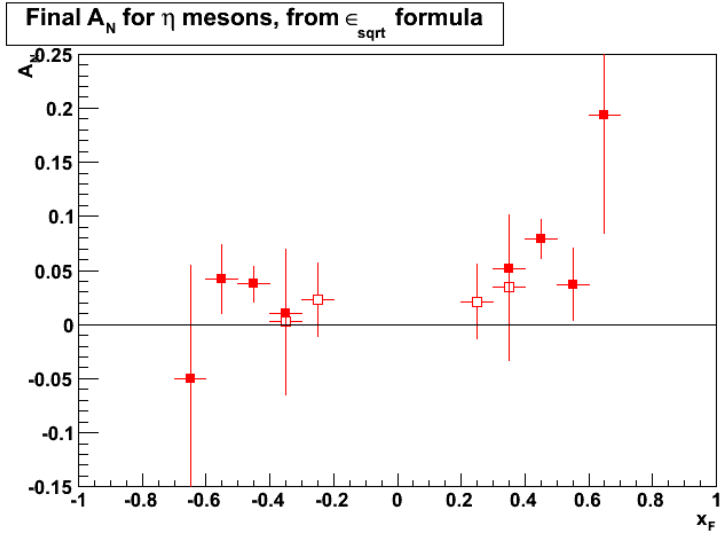


Figure 5.20: The combined South and North MPC  $A_N$  measured as a function of  $x_F$ . The open points are from the Minimum Bias triggered dataset, and the closed points are from the 4×4B triggered dataset.

(closed) points represent the measurement procured from the Minimum Bias (4×4B) triggered dataset. In the  $0.3 < |x_F| < 0.4$  bins, the difference between the Minimum Bias and 4×4B points is less than  $1\sigma$  (stat.). Also the these points (measured at the same  $x_F$ ) are less than 1% correlated based on the rejection factor between the datasets (see Section 4.5), and will be combined for the final results.

## 5.7 $p_T$ Dependence of Asymmetries

The procedure to obtain  $A_N$  as a function of  $x_F$  was demonstrated in Section 5.6. Similarly, one can find the  $p_T$  dependence of the asymmetries. The procedure is the same as for  $x_F$ , so only the final result is shown (Fig. 5.21), with other figures summarized in Appendix C. The  $p_T$  dependence of the asymmetries is calculated for positive (forward going) and negative  $x_F$  values separately.

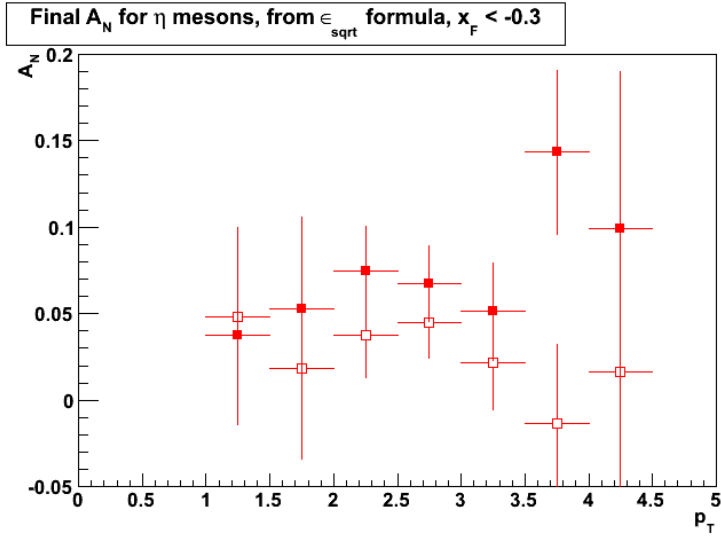


Figure 5.21: The combined South and North asymmetries per  $p_T$  bin. The closed (open) points are for forward (backward) going  $|x_F| > 0.2$  ( $|x_F| < -0.2$ ). The points from  $1.0 < p_T < 2.0$  GeV/ $c$  ( $2.0 < p_T < 4.5$  GeV/ $c$ ) are from the Minimum Bias ( $4 \times 4B$ ) triggered dataset

## 5.8 Cross-checks and Systematics

The results shown so far use functional forms, parameters and cuts which were optimized, but are known not to be perfect. To assess the effect on the data yields and asymmetries, these parameters are systematically changed (within reasonable limits) to test their sensitivity on the final results. These comprise data cross checks and systematic uncertainties.

### 5.8.1 Systematic Uncertainty on the Fitting of the Background

The first check investigates whether there is a systematic uncertainty in the fitting of the background with Eq. 5.8. For this a study was performed using different assumed background functions in the fit: a second and third order polynomial. Figure 5.22 shows an example the result of different background functions in the fit. The systematic error was found by taking the difference of the final  $A_N$  from the  $F + g_\omega$  background fit with the greater error of the 2nd and 3rd polynomial fit, see Fig. 5.22.

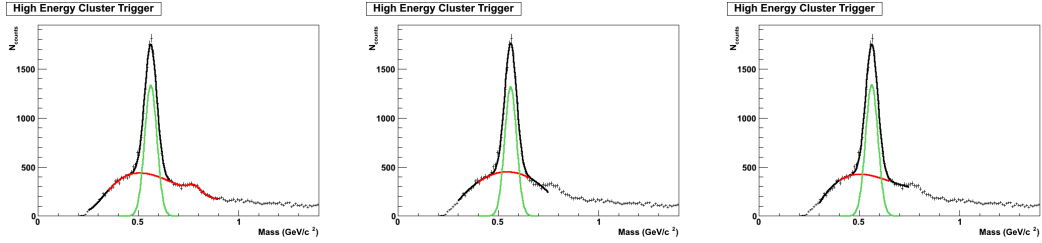


Figure 5.22: Invariant mass spectra fit with different assumed background functions for  $0.5 < x_F < 0.6$  in the South MPC. The far left panel shows the Gamma distribution (default analysis), the center (far right) panel shows a 2nd (3rd) order polynomial.

The systematic error is shown in the left panel in Fig. 5.28 (5.29) for  $x_F$  ( $p_T$ ) dependent  $A_N$ .

### 5.8.2 Systematic Uncertainty from Even-Odd Bunch Crossings

To check for systematic effects due to even or odd bunch crossings, asymmetry calculations were done separately for the even and odd bunch crossings for the four different fill patterns. Figures 5.23 and 5.24 show the raw asymmetries for the South and North MPC, respectively. Figure 5.24 for the North MPC shows a clear discrepancy between the  $\epsilon_{pol}$  and  $\epsilon_{sqrt}$  asymmetries, which is likely due to the relative luminosity difference between the blue and yellow beam. Due to this difference, the final results use only the  $\epsilon_{sqrt}$  asymmetry formula to calculate  $A_N$ , since it is independent of the relative luminosity.

To ensure that the effect is due to the relative luminosity, a systematic error is calculated based on the differences of the even-odd sqrt asymmetries for each fill pattern.

$$\delta A_N^{pattern} = \frac{p_0}{2} (1 - P(\chi^2_{p_0=0})) \quad (5.12)$$

where  $p_0$  is determined from a constant fit across same signed  $x_F$  to  $A_N^{odd} - A_N^{even}$  with uncertainties  $\sqrt{\sigma_{odd}^2 + \sigma_{even}^2}$ .  $P(\chi^2_{p_0=0})$  is the probability of having  $\chi^2$  by setting  $p_0 = 0$ .

This is necessary so that when  $p_0 - 0$  is small,  $1 - P(\chi^2_{p_0=0})$  approaches zero, negating any statistical fluctuations in the uncertainty.

$\delta A_N^{pattern}$  is calculated for each of the four fill patterns for each arm, and weighted together to find the final systematic error. The center panels in figures 5.25 and 5.26 demonstrate how the constant fit is applied to  $A_N^{odd} - A_N^{even}$ . Figure 5.27 shows the  $\delta A_N^{patt}$  values. The combined weighted values of the patterns and arms for  $\delta A_N^{\Delta patt}$  is small, and is given in Figure 5.28. Similarly, the  $\delta A_N^{\Delta patt}$  was calculated for the  $p_T$  dependent asymmetries and is shown in Fig. 5.29.

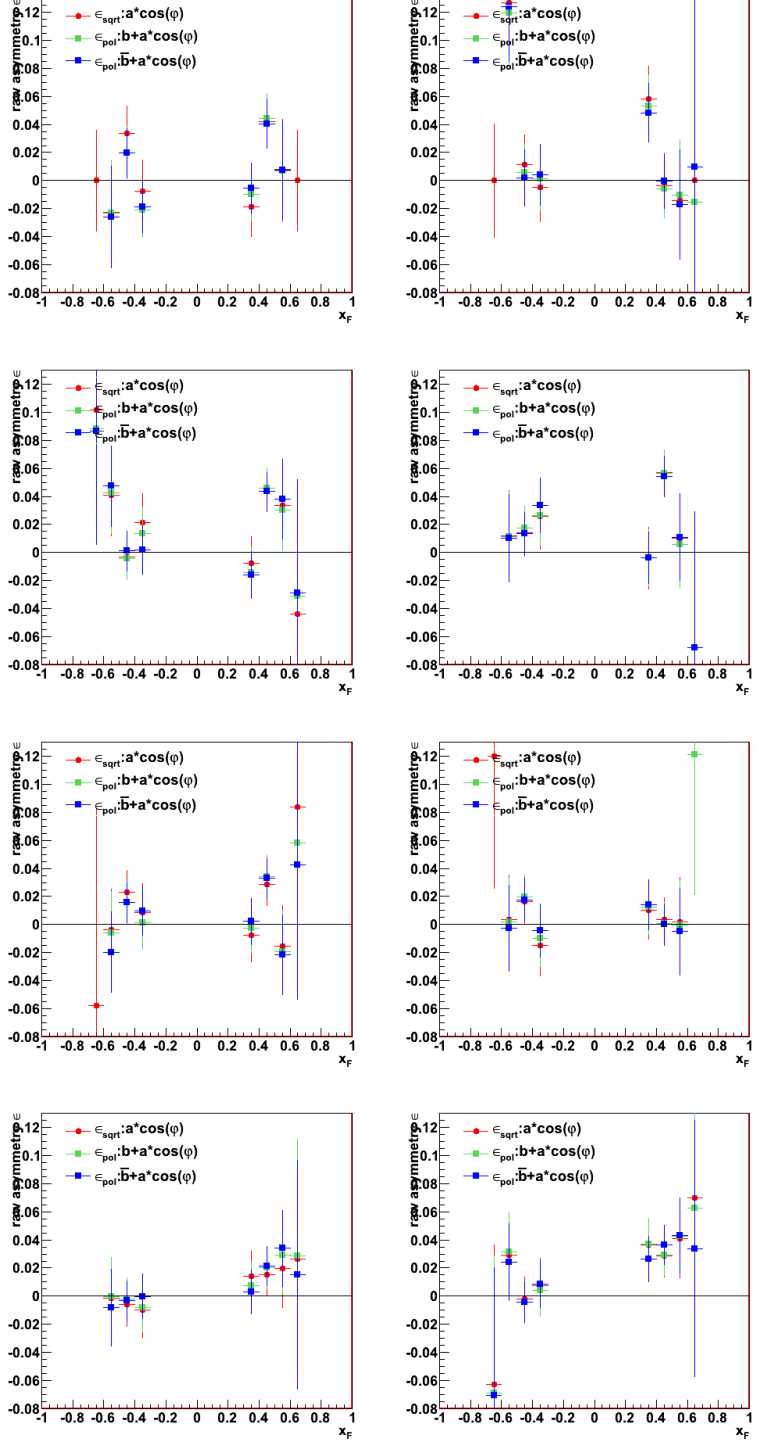


Figure 5.23: The fill pattern even-odd comparison for the South MPC. The columns top to bottom are the raw asymmetries for the fill patterns 1-4, respectively. The left (right) column are the raw asymmetries for even (odd) bunch crossings.

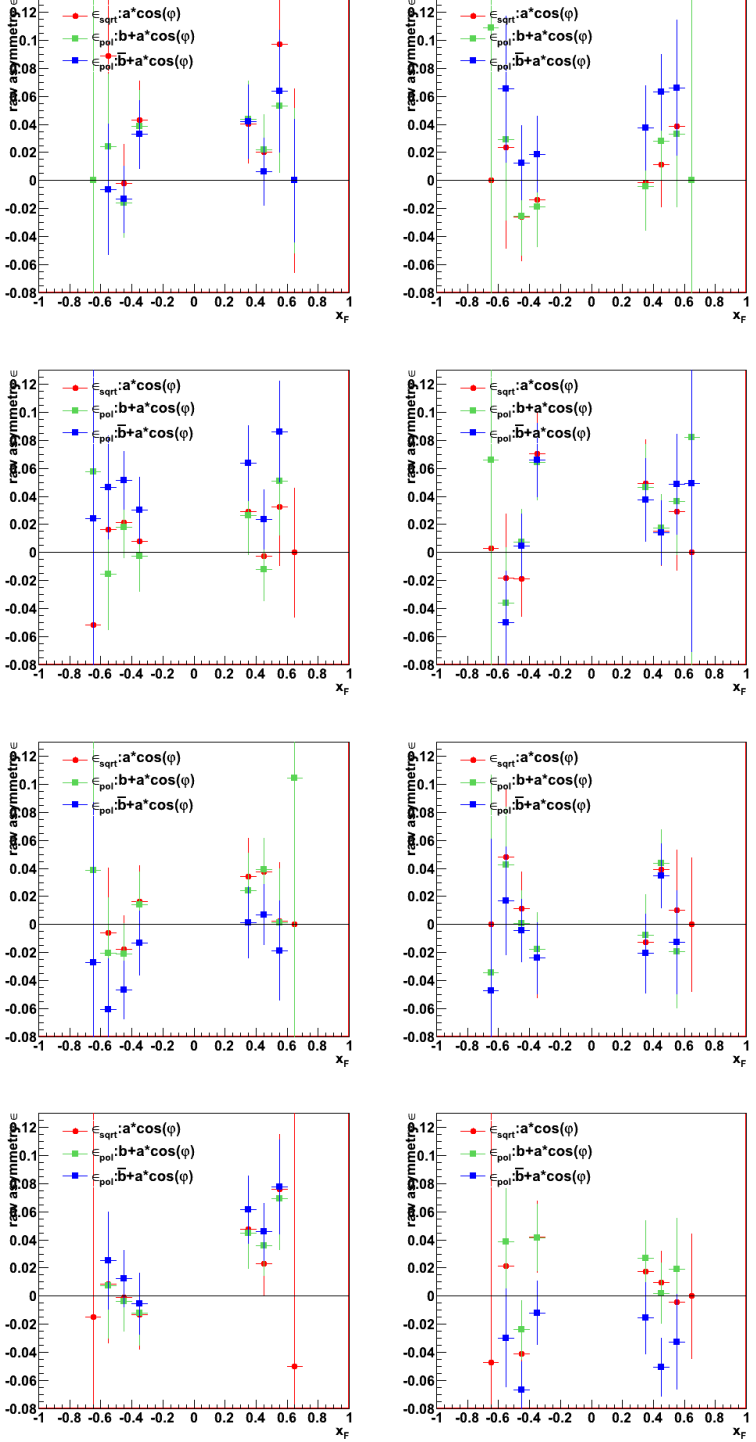


Figure 5.24: The fill pattern even-odd comparison for the North MPC. The columns top to bottom are the raw asymmetries for the fill patterns 1-4, respectively. The left (right) column are the raw asymmetries for even (odd) bunch crossings.

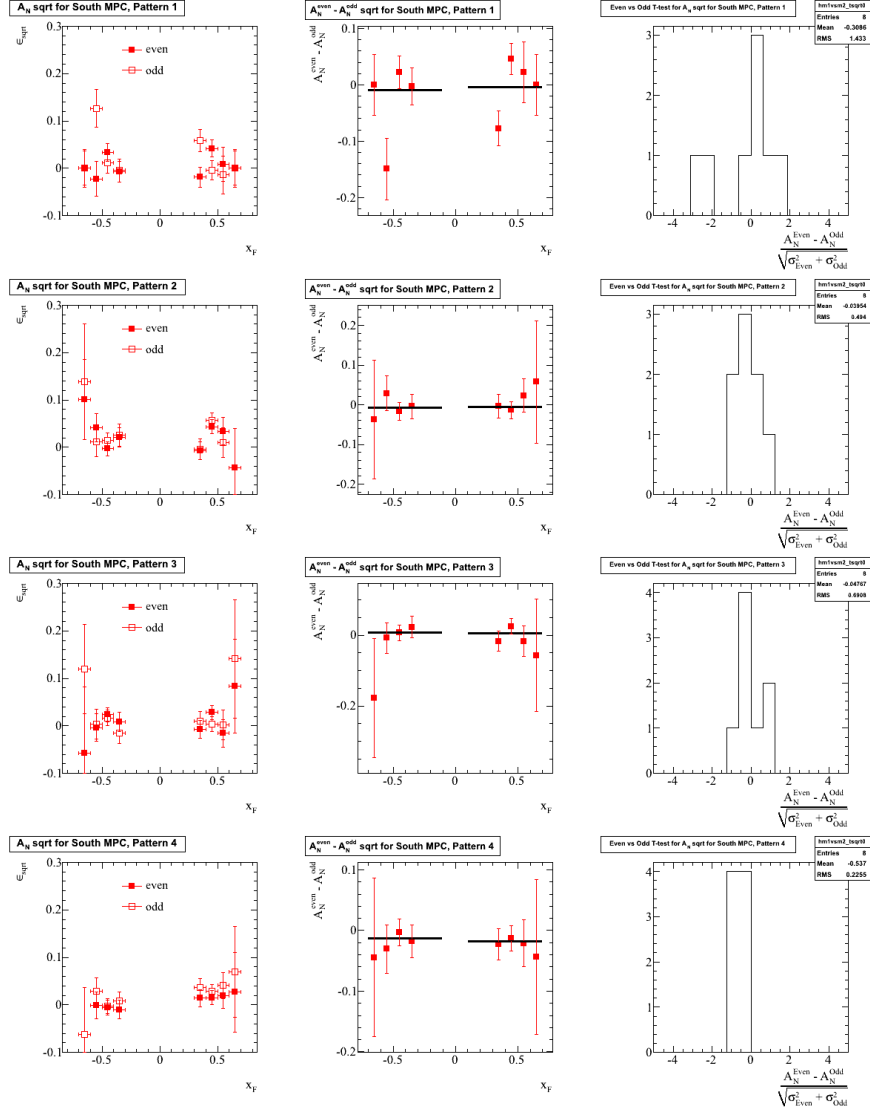


Figure 5.25: The fill pattern systematic calculations for the South MPC. The left column has closed (open) points for the even (odd) fill patterns. The middle column shows the constant  $p_0$  fits to the  $A_N^{\text{odd}} - A_N^{\text{even}}$  values, where  $p_0$  from the fits is used to calculate  $\delta A_N$ . Note that there are separate fits to negative and positive  $x_F$ . The right column is the T-test for  $A_N^{\text{odd}} - A_N^{\text{even}}$ .

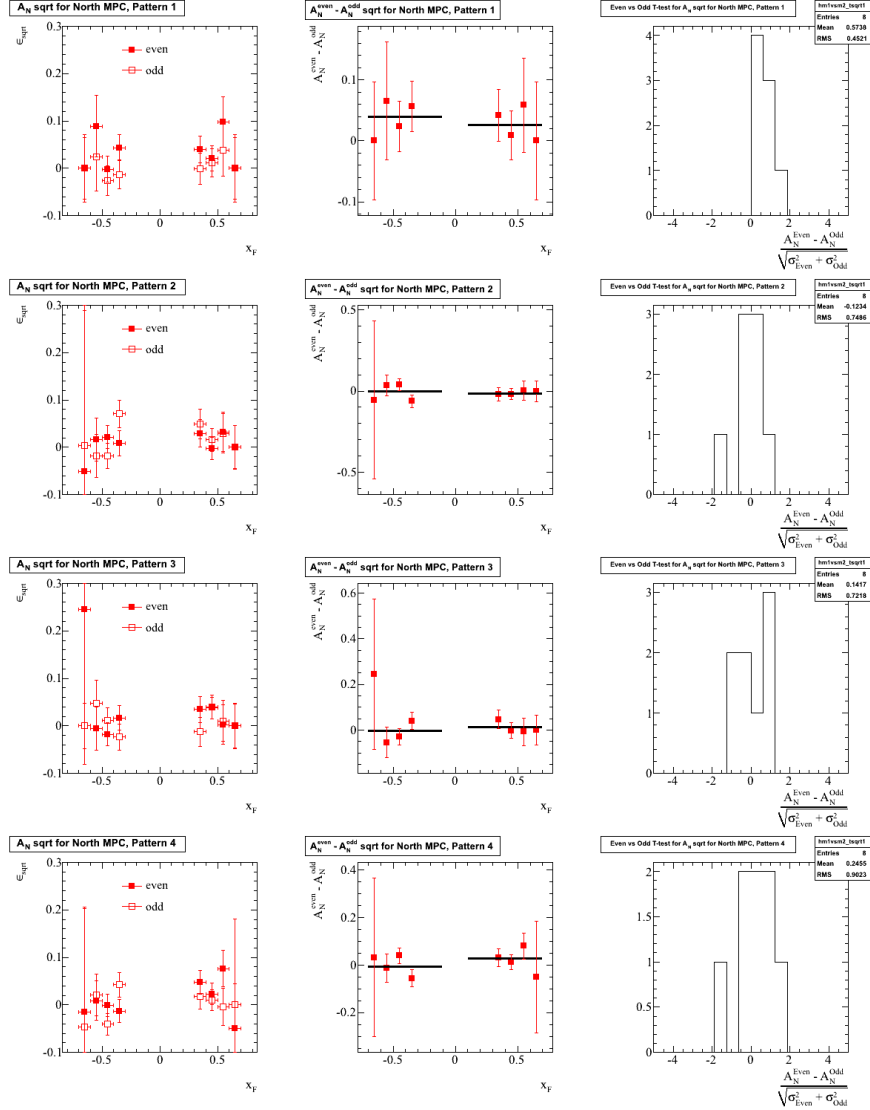


Figure 5.26: The systematic calculations for the North MPC. The left column has closed (open) points for the even (odd) fill patterns. The middle column shows the constant  $p_0$  fits to the  $A_N^{\text{odd}} - A_N^{\text{even}}$  values, where  $p_0$  from the fits is used to calculate  $\delta A_N$ . Note that there are separate fits to negative and positive  $x_F$ . The right column is the T-test for  $A_N^{\text{odd}} - A_N^{\text{even}}$ .

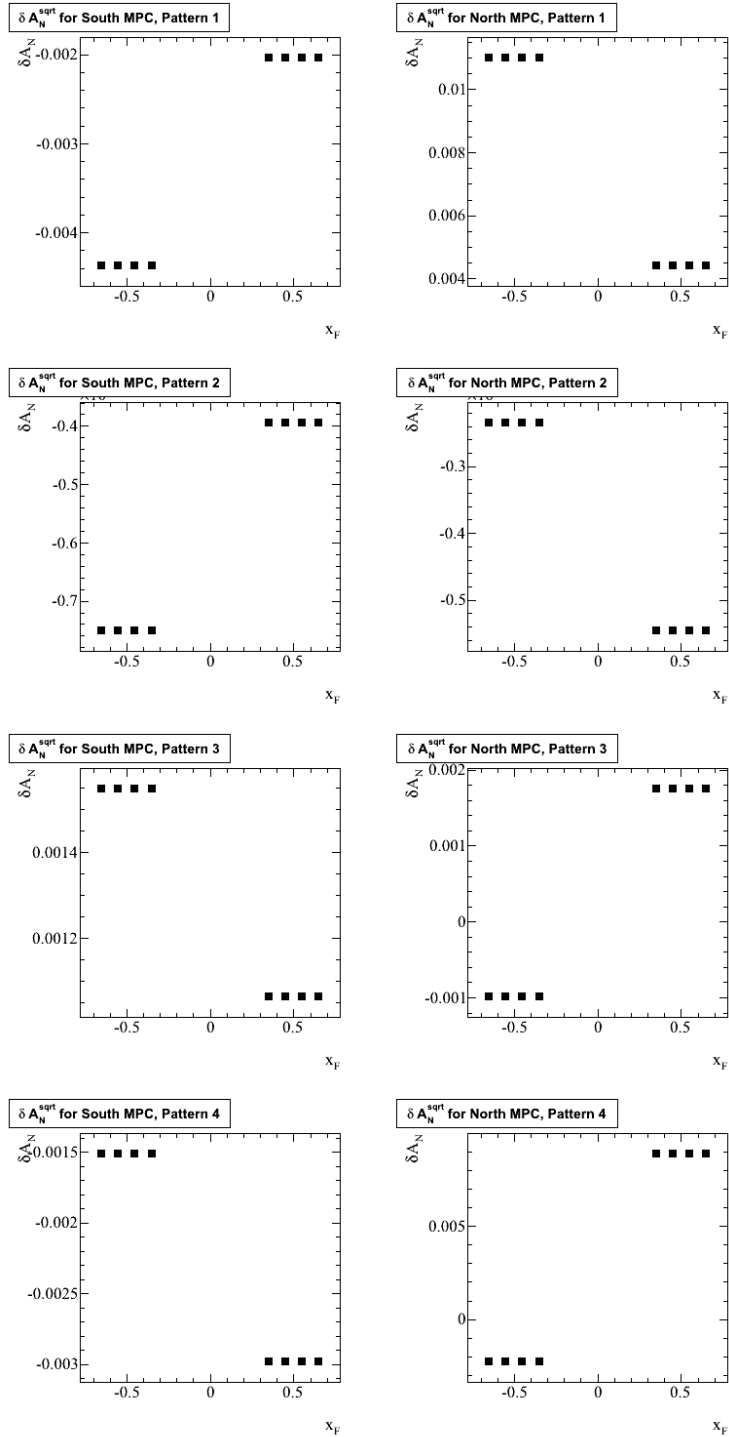


Figure 5.27: The  $\delta A_N$  values for the different fill patterns. The left (right) panel shows the South (North) MPC.

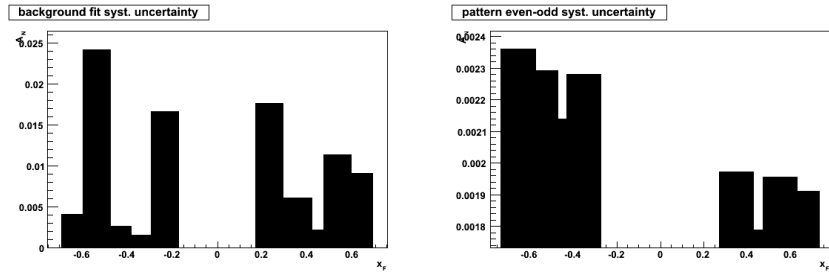


Figure 5.28: The absolute systematic uncertainties for the  $x_F$  dependent  $A_N$ . The left panel shows the systematic uncertainties in the background function fit. The right panel shows the systematic uncertainties between the even-odd bunch crossings weighted together.

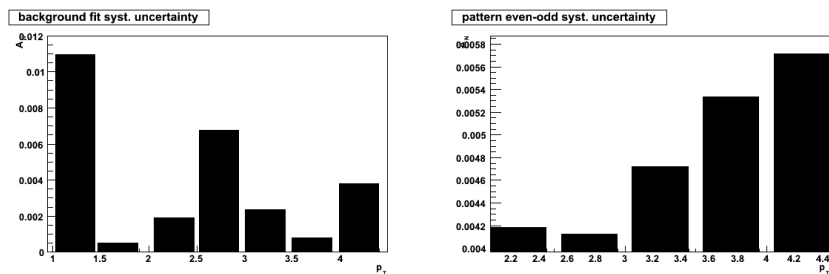


Figure 5.29: The absolute systematic uncertainties for the  $p_T$  dependent asymmetries. The left panel shows the systematic uncertainties in the background function fit. The right panel shows the systematic uncertainties between the even-odd bunch crossings weighted together.

### 5.8.3 Bunch Shuffling

To check for systematic effects, bunch shuffling was done. For each fill, bunch polarizations are randomly assigned and  $A_N^{b.s.}$  is calculated, and divided by the error,  $\sigma_{A_N}$ , on the real results. This procedure is repeated 5000 times. If there are no systematic effects, the distribution of these  $A_N^{b.s.}/\sigma_{A_N}$  should be Gaussian with a mean of zero, and a width of one. Fig. 5.30 shows the bunch shuffling done using the  $\epsilon_{sqrt}$  formula in the  $\eta$  mass region for  $x_F$  dependent asymmetries in the North MPC. The results are consistent with no systematic effects.

Figure 5.31 show the bunch shuffling using the  $\epsilon_{pol}$  formula in the  $\eta$  mass region for  $x_F$  dependent asymmetries in the North MPC. The North MPC results show a systematic in using the polarization formula, with all of the Gaussian widths greater than 1. This is likely related to the even-odd relative luminosity effect discussed in Section 5.8.2. This systematic effect is avoided by using the square-root asymmetry for the final results.

See Appendix E for all of the other bunch shuffling plots pertaining to the South and North MPC,  $\epsilon_{sqrt}$  and  $\epsilon_{pol}$ , and for the Minimum Bias and 4×4B triggered datasets.

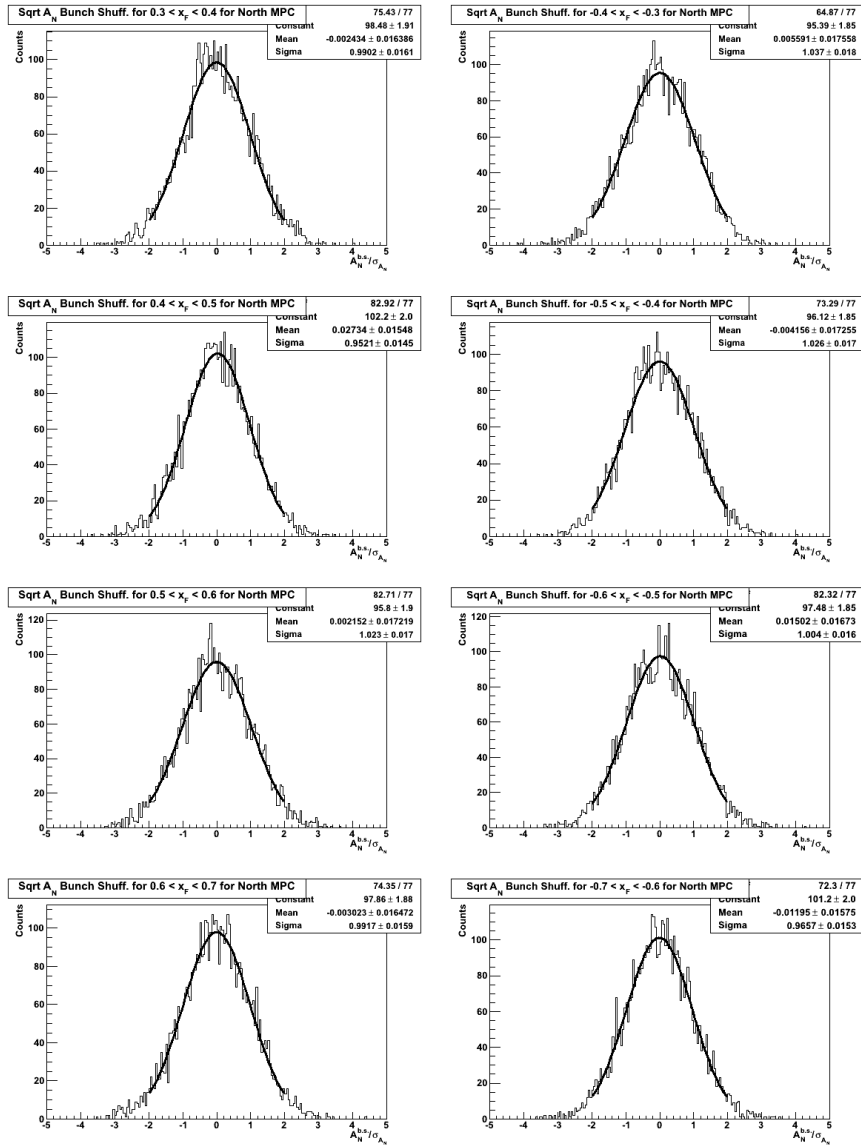


Figure 5.30: The  $x_F$  bunch shuffling results for 4×4B triggered dataset using the North MPC using  $\epsilon_{sqrt}$  formula.

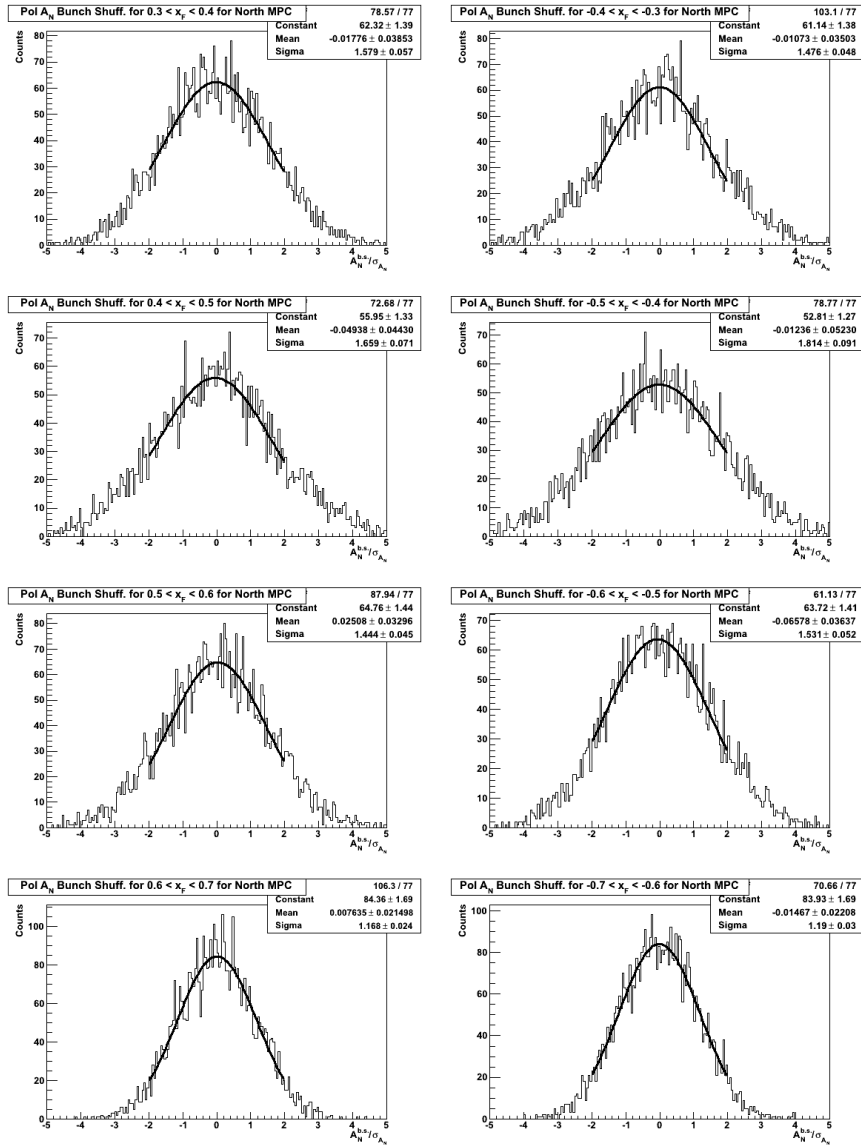


Figure 5.31: The  $x_F$  bunch shuffling results for 4×4B data using the North MPC using  $\epsilon_{pol}$  formula.

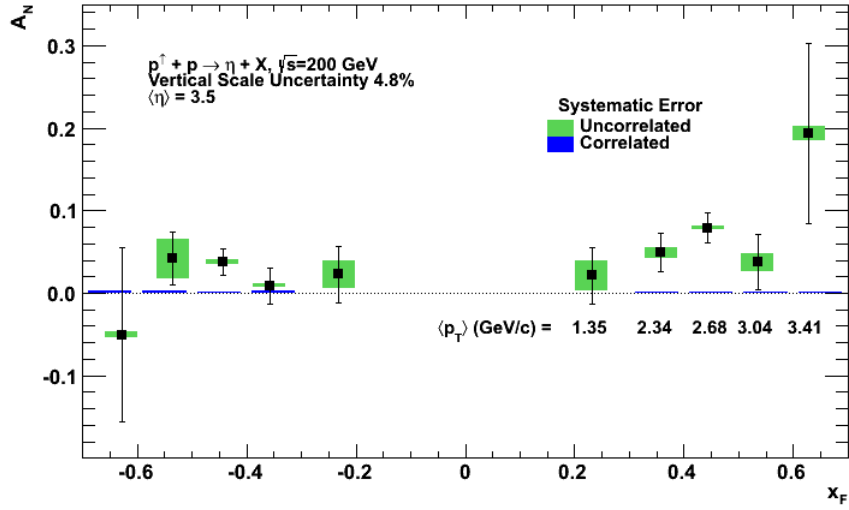


Figure 5.32: The final  $x_F$  dependence of  $A_N$ . The green bands around the points are the background variation systematic error, the blue bars pertain to the even-odd effect systematic error. The mean  $p_T$  is given for each respective  $x_F$  point below the positive  $x_F$  point (which is the same for negative  $x_F$  points).

## 5.9 Final Asymmetry

Figure 5.32 shows the  $x_F$  dependence of  $A_N$ . Figure 5.33 shows the  $p_T$  dependence of  $A_N$ . The uncorrelated systematic from using different fit functions to the background in Section 5.8 is shown as green bands on the points. The correlated systematic for the even-odd pattern crossing effect discussed in 5.8.2 is shown as blue bars graph under the points. The final values of the points are given in Table B.3 in the Appendix. Discussion of these results will be given in Chapter 6.

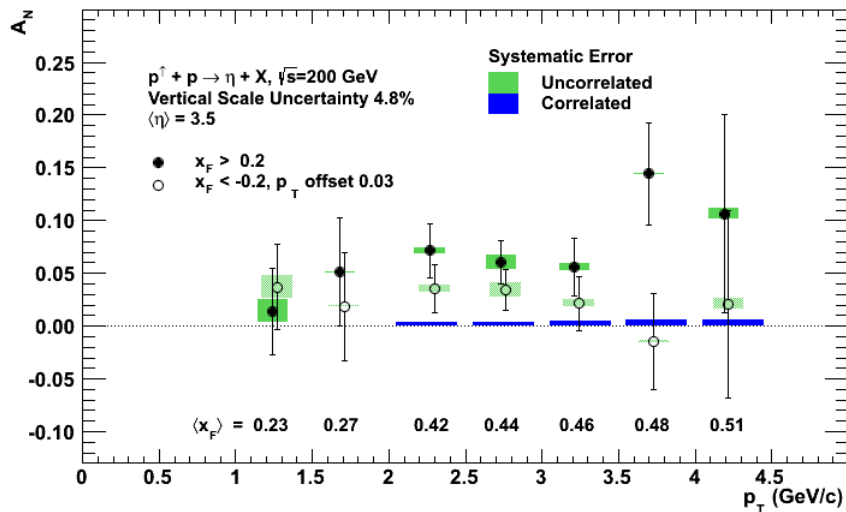


Figure 5.33: The final  $p_T$  dependence of the asymmetries. The green bands around the points are the background variation systematic error, the blue bars pertain to the even-odd effect systematic error. The mean  $x_F$  is given for each respective  $p_T$  point on the bottom part of the figure.

# Chapter 6

## Results and Discussion

This chapter summarizes and discusses the results made in this work: the  $\eta$  mesons invariant cross section, and the transverse single-spin asymmetry,  $\eta$  meson  $A_N$ .

### 6.1 Cross section of $\eta$ mesons at forward rapidity

The invariant cross section of  $\eta$  mesons is shown in Figure 6.1 as a function of transverse momentum, measured between  $0.5 < p_T < 5.5$  GeV/ $c$  within a pseudorapidity range of  $3.0 < |\eta| < 3.8$ . The results are compared to a NLO pQCD calculation [91], over the same pseudorapidity region as the measurement. The lower panel shows the comparison between the measured cross section and the NLO pQCD. At large momenta ( $p_T > 1.5$  GeV/ $c$ ), the NLO pQCD calculation is in very good agreement with the measured cross section. At low momentum  $p_T < 2.0$  GeV/ $c$ , the agreement becomes less clear, which is likely due to non-perturbative effects present at low  $p_T$ , as discussed Section 2.1.2.

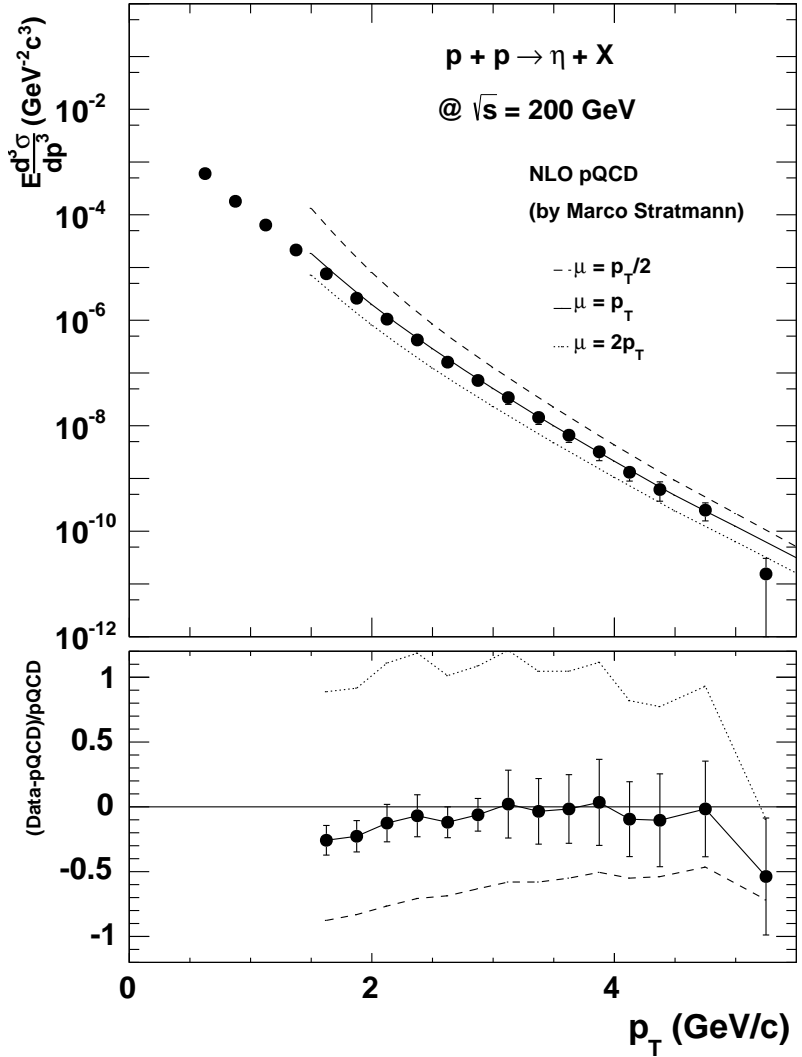


Figure 6.1: The cross section of inclusive  $\eta$  mesons produced from  $p + p$  collisions at  $\sqrt{s} = 200$  GeV at forward rapidity. The top panel shows the measured cross section versus transverse momentum ( $p_T$ ), compared to the NLO pQCD calculation [91]. The bottom panel shows the difference between the measured cross section and The NLO pQCD calculation. The error bars represent the sum of the Statistical and Systematic Errors.

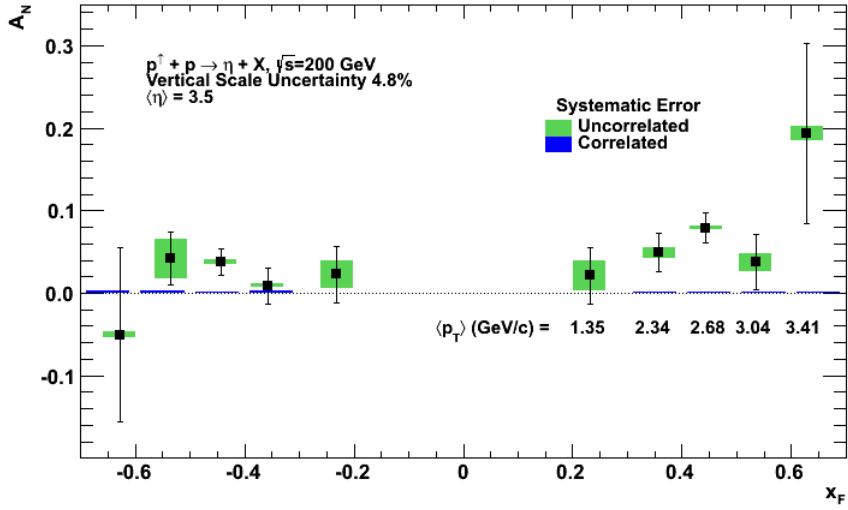


Figure 6.2: The  $x_F$  dependence of  $A_N$ . The green bands around the points are the background variation systematic error, the blue bars pertain to the even-odd effect systematic error. The mean  $p_T$  is given for each respective  $x_F$  point below the positive  $x_F$  point (which are the same for negative  $x_F$  points).

## 6.2 $A_N$ of $\eta$ mesons as a function of $x_F$

The final  $x_F$  dependent  $A_N$  asymmetry is shown in Fig. 6.2. The average pseudorapidity of the measured  $\eta$  mesons is  $\langle\eta\rangle=3.5$ . For  $A_N$  measured at forward  $x_F$  ( $x_F > 0$ ), a clear, rising non-zero asymmetry is seen, while  $A_N$  for backward  $x_F$  ( $x_F < 0$ ) is flat and consistent with zero when averaged over  $x_F$ . The uncorrelated systematic from using different fit functions to the background in Section 5.8 is shown as green bands around the points. The correlated systematic for the even-odd pattern crossing effect, discussed in Section 5.8.2, is shown as a blue band under the points. The mean  $p_T$  is given for each respective  $x_F$  point below the positive  $x_F$  point, which are the same for negative  $x_F$  points. The final values of the points are given in Table B.3 in Appendix B.

For the forward going  $x_F$ , there is a clear non-zero asymmetry ranging from 5% to 20%. At forward rapidity,  $x_F$  is proportional to the polarized parton momentum

from the relation

$$x_F = 2 \frac{p_L}{\sqrt{s}} \approx 2 \frac{\langle z \rangle p_{jet}}{\sqrt{s}} \approx \langle z \rangle x_1 \quad (6.1)$$

This suggest that non zero asymmetries could arise from a partonic function dependent on  $x$  that is only partially dependent on the collision energy. An underlying  $x$ -dependent Sivers or Collins function (see Section 2.3) could provide a possible explanation of these asymmetries. For backward going  $x_F$ , the points are consistent with zero within statistical uncertainty across  $x_F$  as expected.

Figure 6.3 shows the measured  $\eta$  meson  $A_N$  in comparison to other related  $A_N$  measurements. The left panel shows a comparison between  $\eta$  meson and  $\pi^0$  meson  $A_N$  in the same  $x_F$  and pseudorapidity range at various collision energies. It is observed that  $\eta$  meson  $A_N$  is very similar to the  $\pi^0$  measurements made by the E704 and STAR experiments [12, 42], as well as by the PHENIX experiment using the MPC [43]. The right panel shows a comparison between the  $\eta$  and  $\pi^0$  mesons  $A_N$  measurement made by STAR [57] from the 2006 RHIC run, which had the same collision energy of  $\sqrt{s}=200$  GeV as in this work. The average pseudorapidity of the PHENIX result is  $\langle \eta \rangle = 3.5$ , while the average pseudorapidity of the STAR results is  $\langle \eta \rangle = 3.68$ . For  $x_F > 0.55$ , STAR concluded that their  $A_N^\eta$  is larger than their  $A_N^{\pi^0}$ . When compared to PHENIX, the STAR  $\pi^0$  meson  $A_N$  is consistent with this new  $\eta$  meson  $A_N$  measurement. For  $x_F > 0.55$ , the STAR  $\eta$  meson  $A_N$  is larger than this higher statistics PHENIX  $\eta$  meson  $A_N$  measurement, but these two results could still be consistent with each other within the statistical uncertainty. A future, higher statistic measurement will provide further insight into this relationship.

The purple curve in Fig. 6.3 uses calculations provided by Kanazawa and Koike

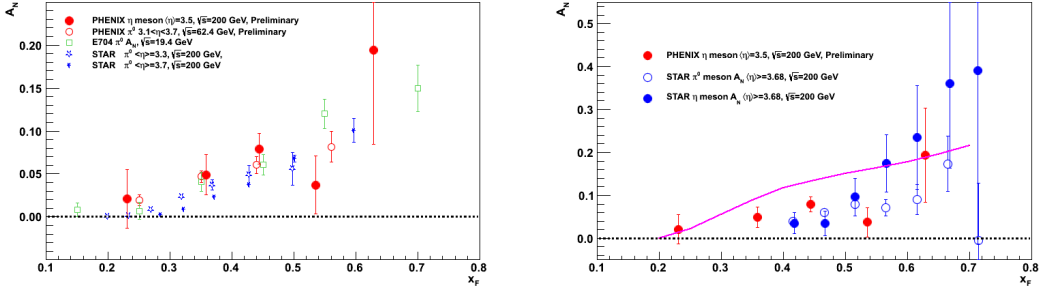


Figure 6.3: Comparison between the  $\eta$  meson  $A_N$  and other  $\pi^0$  and  $\eta$  meson  $A_N$  results. The left panel shows the comparison with previous  $\pi^0$  meson  $A_N$  results from PHENIX, STAR, and E704 in red, blue, and green points, respectively [43, 57, 12]. The right panel shows a comparison to the STAR results (blue points) from the 2006 RHIC run [57], and a twist-3 calculation (purple curve) provided by Kanazawa and Koike [95].

[95] based on [58] to determine whether the twist-3 framework could explain non-zero asymmetries. For  $0 < x_F < 0.5$ , the twist-3 framework is not likely to explain the asymmetries measured by both PHENIX and STAR—they are described solely by a convolution of the Sivers and Collins Effect. At higher  $x_F$  ( $x_F > 0.5$ ), twist-3 effects could play a role, but a definitive conclusion must wait for higher statistical precision measurement.

### 6.3 $A_N$ of $\eta$ mesons as a function of $p_T$

The final  $p_T$  dependent  $A_N$  asymmetry is shown in Fig. 6.4. The average pseudorapidity of measured  $\eta$  mesons is  $\langle\eta\rangle=3.5$ . For  $A_N$  measured at forward  $x_F$  ( $x_F > 0.2$ ), a clear non-zero asymmetry is seen, while  $A_N$  for backward  $x_F$  ( $x_F < -0.2$ ) is consistent with zero. The uncorrelated systematic from using different fit functions to the background is shown as green bands around the points. The correlated systematic for the even-odd pattern crossing effect is shown as a blue band graph under the points. The final values of the points are given in Table D.2 in Appendix D.

As mentioned in Section 2.3.4, it has been suggested by Kang [55] that in

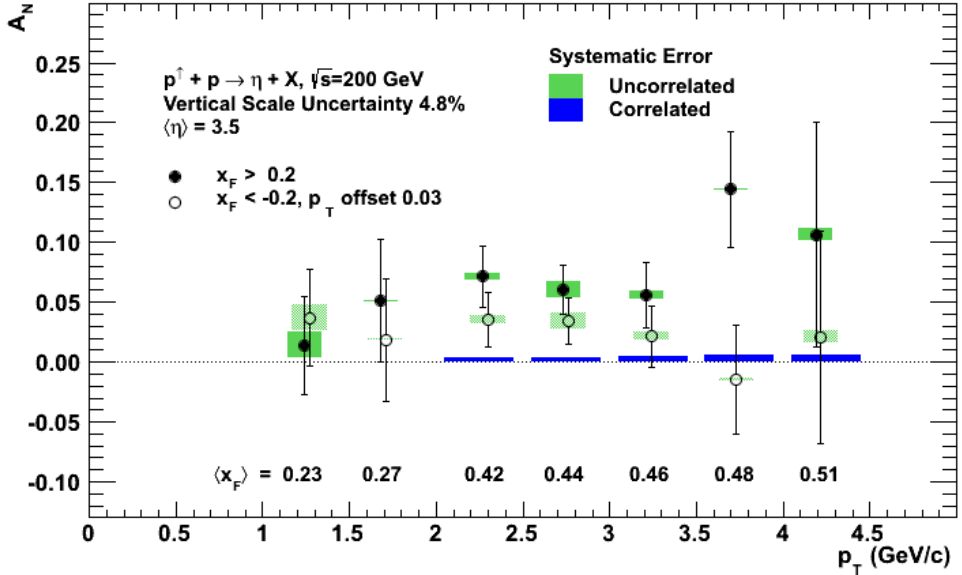


Figure 6.4: The  $p_T$  dependence of  $A_N$ . The green bands around the points are the background variation systematic error, the blue bars pertain to the even-odd effect systematic error. The mean  $x_F$  is given for each respective  $p_T$  point on the bottom part of the figure.

twist-3 descriptions, the  $p_T$  dependence should follow

$$A_N \approx \frac{\alpha}{p_T} - \frac{\alpha'}{p_T^3} + \dots \quad (6.2)$$

such that  $A_N$  should decrease at some high  $p_T$  value. While the asymmetry is non-zero, there is no indication that  $A_N$  is decreasing with increasing  $p_T$  within our current statistical uncertainty. Figure 6.5 uses calculations provided by Kanazawa and Koike [95] based on [58]. These calculations confirm no falloff in the twist-3 framework for  $A_N$  versus  $p_T$  for  $x_F$  values of  $0.2 < x_F < 0.7$ . Based on a discussion with Kanazawa and Koike, a future, higher statistical measurement could plot  $A_N$  versus  $p_T$  within a tighter  $x_F$  region of  $0.6 < x_F < 0.7$ , which may have an observable decrease in the asymmetry at high- $p_T$ .

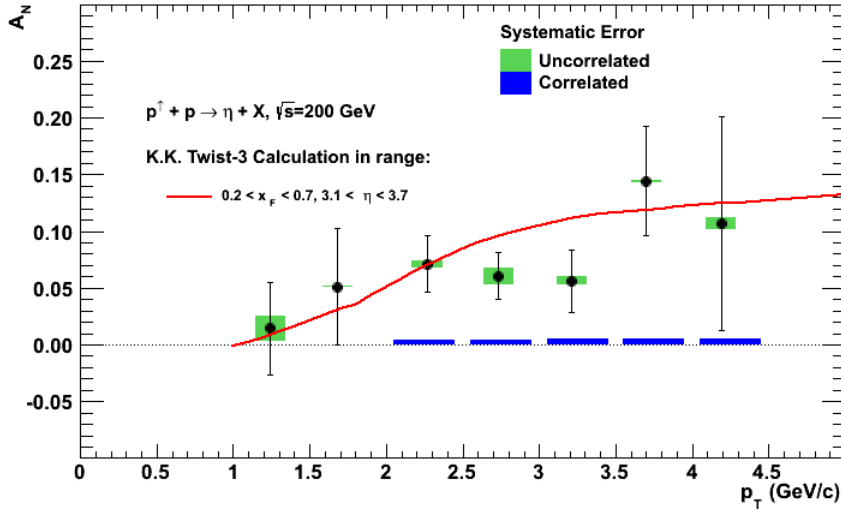


Figure 6.5: Comparison between the twist-3 prediction of  $\eta$   $A_N$  at forward  $x_F$  as a function of  $p_T$  and the measurement made in this analysis.

## 6.4 Outlook

In 2012, PHENIX recorded more transverse data, with a sampled integrated luminosity 2.5 times greater than 2008 run. A new trigger was also installed in the MPC that divides each MPC into six separate regions that fire independently, which is expected to greatly reduce correlated background under the  $\eta$  mesons signal region at high  $p_T$ . The new  $\eta$   $A_N$  measurement by the MPC in PHENIX will further enhance our understanding of the transverse single spin asymmetries, and their origins.

In addition, the MPC-EX detector [96] is expected to be installed in 2015, and will allow for separation of direct photons from decay photons. A measurement of the direct photon  $A_N$  is interesting, as they are exclusively sensitive to the Sivers Effect. Measurement of  $A_N$  of direct photons could assign a sign and magnitude to the Sivers Effect in pions and  $\eta$  meson  $A_N$ . A small (large) direct photon  $A_N$  would indicate a small (large) contribution of the Sivers Effect in pion and  $\eta$  meson  $A_N$ .

The  $\eta$  meson cross section measurement has the potential to be used in future

global analyses of the  $\eta$  meson fragmentation function, where it could enhance our understanding of the fragmentation process for  $u$  quarks,  $d$  quarks, and gluons into  $\eta$  mesons.

## Chapter 7

# Conclusions

By utilizing quality data taken by the MPC detector installed at forward rapidity in the PHENIX experiment at RHIC, the measurement of the invariant cross section as a function of  $p_T$  and the transverse single spin asymmetry  $A_N$  as a function of  $x_F$  and  $p_T$  has been measured for inclusive  $\eta$  mesons produced at forward rapidity ( $\langle\eta\rangle = 3.5$ ) from  $p^\uparrow + p$  collisions at center of mass energy of  $\sqrt{s} = 200$  GeV. Non-zero asymmetries measured at forward  $x_F$  have been observed for  $x_F$  dependent  $A_N$  that are consistent with previous  $\pi^0$  meson results within statistical uncertainties for  $x_F < 0.6$ , likely constraining  $A_N^\eta \approx A_N^{\pi^0}$ . At  $x_F > 0.6$ , twist-3 effects could play a role. A non-zero  $p_T$  dependence of  $A_N$  for  $0.2 < x_F < 0.7$  was observed, with no observable decrease at high  $p_T$ .

The NLO pQCD calcuation was found to be consistent the invariant cross section measurement at large momentum of  $p_T > 2.0$  GeV/ $c$ , and explored the perturbative QCD limit at low momenta ( $0 < p_T < 2.0$  GeV/ $c$ ). This high statistics, high precision measurement may provide insight into the fragmentation process of  $\eta$  mesons in future global analyses of the  $\eta$  fragmentation function.

## **Appendix A**

## **Tables For Cross Section**

## A.1 The Minimum Bias Measured Spectra, invariant yields, corrections, and cross sections For the South and North MPC

$\mathcal{L}_{MB} = 1.92 \times 10^{-2} \text{ pb}^{-1}$								
MPC	$p_T$ bin	InvYield	$\sigma_{InvY}$	$\epsilon_{reco}$	$\epsilon_{MB}$	bincorr	X-section	$\sigma_{xc}$
South	0.625	4.02e+04	1.90e+03	1.50e-02	0.760	0.96	6.14e-04	2.79e-05
North	0.625	2.51e+04	4.03e+03	1.12e-02	0.720	0.96	5.14e-04	7.93e-05
South	0.875	2.46e+04	1.46e+03	2.14e-02	0.760	0.96	1.88e-04	1.07e-05
North	0.875	1.80e+04	7.06e+02	1.67e-02	0.720	0.96	1.77e-04	6.65e-06
South	1.125	1.43e+04	5.68e+02	2.72e-02	0.760	0.96	6.70e-05	2.56e-06
North	1.125	1.05e+04	3.90e+02	2.18e-02	0.720	0.96	6.16e-05	2.19e-06
South	1.375	6.77e+03	2.64e+02	3.37e-02	0.760	0.96	2.10e-05	7.86e-07
North	1.375	5.63e+03	2.03e+02	2.68e-02	0.720	0.96	2.20e-05	7.61e-07
South	1.625	3.50e+03	1.49e+02	4.16e-02	0.760	0.96	7.44e-06	3.03e-07
North	1.625	2.84e+03	1.14e+02	3.22e-02	0.720	0.96	7.79e-06	3.01e-07
South	1.875	1.68e+03	8.92e+01	5.08e-02	0.760	0.96	2.53e-06	1.29e-07
North	1.875	1.37e+03	6.62e+01	3.90e-02	0.720	0.96	2.69e-06	1.25e-07
South	2.125	9.64e+02	5.51e+01	6.08e-02	0.760	0.96	1.07e-06	5.87e-08
North	2.125	6.97e+02	4.30e+01	4.64e-02	0.720	0.96	1.01e-06	6.01e-08
South	2.375	4.64e+02	3.38e+01	7.11e-02	0.760	0.96	3.94e-07	2.76e-08
North	2.375	4.13e+02	3.02e+01	5.53e-02	0.720	0.96	4.52e-07	3.17e-08
South	2.625	2.23e+02	2.17e+01	8.16e-02	0.760	0.96	1.49e-07	1.40e-08
North	2.625	1.90e+02	1.83e+01	6.21e-02	0.720	0.96	1.67e-07	1.55e-08
South	2.875	1.28e+02	1.34e+01	8.75e-02	0.760	0.96	7.29e-08	7.34e-09
North	2.875	9.01e+01	1.12e+01	6.67e-02	0.720	0.96	6.75e-08	8.09e-09
South	3.250	9.34e+01	1.15e+01	9.08e-02	0.760	0.85	2.56e-08	2.70e-09
North	3.250	5.50e+01	1.11e+01	6.72e-02	0.720	0.85	2.03e-08	3.52e-09
South	3.750	1.25e+01	6.17e+00	8.97e-02	0.760	0.85	3.02e-09	1.26e-09
North	3.750	6.26e+00	8.54e+00	6.51e-02	0.720	0.85	2.07e-09	2.41e-09

Table A.1: The invariant yield, reconstruction efficiency, bin shift correction, and invariant cross section for the South and North MPC

## A.2 The Minimum Bias cross section and systematic errors

$\mathcal{L}_{MB} = 1.92 \times 10^{-2} \text{ pb}^{-1}$								
$p_T \text{ bin}$	$X\text{-section}$	$\sigma_{xc}$	$s_{final}$	$s_{escale}$	$s_{yield+me}$	$s_{geant}$	$s_{global}$	$s_{all}$
0.625	6.03e-04	2.63e-05	1.098e-04	0.030	0.139	0.060	0.097	0.18
0.875	1.80e-04	5.65e-06	3.883e-05	0.067	0.170	0.060	0.097	0.22
1.125	6.39e-05	1.67e-06	9.906e-06	0.083	0.065	0.060	0.097	0.16
1.375	2.15e-05	5.47e-07	3.195e-06	0.091	0.028	0.060	0.097	0.15
1.625	7.61e-06	2.14e-07	1.153e-06	0.089	0.044	0.060	0.097	0.15
1.875	2.61e-06	8.98e-08	3.986e-07	0.094	0.037	0.060	0.097	0.15
2.125	1.04e-06	4.20e-08	1.845e-07	0.110	0.079	0.060	0.097	0.18
2.375	4.19e-07	2.08e-08	7.979e-08	0.111	0.104	0.060	0.097	0.19
2.625	1.57e-07	1.04e-08	2.134e-08	0.123	0.051	0.060	0.097	0.14
2.875	7.04e-08	5.44e-09	9.339e-09	0.150	0.036	0.060	0.097	0.13
3.250	2.36e-08	2.14e-09	4.741e-09	0.167	0.152	0.060	0.097	0.20
3.750	2.81e-09	1.12e-09	3.666e-09	0.218	1.296	0.060	0.097	1.30

Table A.2: The Minimum Bias cross section and systematic errors.

### A.3 The $4 \times 4B$ measured spectra, invariant yields, corrections, and cross sections For the South and North MPC

$\mathcal{L}_{4 \times 4B} = 6.65 \text{ pb}^{-1}$								
MPC	$p_T$ bin	InvYield	$\sigma_{InvY}$	$\epsilon_{reco}$	$\epsilon_{4 \times 4B}$	bincorr	X-section	$\sigma_{xc}$
South	2.125	9.54e+03	2.25e+02	0.015	0.100	0.97	1.04e-06	2.46e-08
North	2.125	3.09e+03	1.02e+02	0.011	0.038	0.97	1.17e-06	3.86e-08
South	2.375	1.33e+04	2.10e+02	0.021	0.138	0.97	4.39e-07	6.94e-09
North	2.375	5.41e+03	2.46e+02	0.017	0.074	0.97	4.32e-07	1.97e-08
South	2.625	1.41e+04	2.03e+02	0.027	0.190	0.97	1.84e-07	2.64e-09
North	2.625	6.39e+03	1.32e+02	0.022	0.132	0.97	1.64e-07	3.39e-09
South	2.875	1.14e+04	1.81e+02	0.034	0.260	0.97	7.94e-08	1.26e-09
North	2.875	5.97e+03	1.26e+02	0.027	0.202	0.97	7.85e-08	1.66e-09
South	3.125	7.76e+03	1.84e+02	0.042	0.346	0.97	3.45e-08	8.18e-10
North	3.125	4.34e+03	1.22e+02	0.032	0.285	0.97	3.37e-08	9.44e-10
South	3.375	4.18e+03	1.28e+02	0.051	0.435	0.97	1.39e-08	4.22e-10
North	3.375	2.68e+03	1.03e+02	0.039	0.347	0.97	1.53e-08	5.89e-10
South	3.625	2.29e+03	8.31e+01	0.061	0.532	0.97	6.52e-09	2.37e-10
North	3.625	1.49e+03	7.92e+01	0.046	0.448	0.97	6.84e-09	3.64e-10
South	3.875	1.24e+03	6.02e+01	0.071	0.617	0.97	3.35e-09	1.63e-10
North	3.875	6.76e+02	5.06e+01	0.055	0.527	0.97	2.94e-09	2.20e-10
South	4.125	4.53e+02	4.02e+01	0.082	0.691	0.97	1.23e-09	1.09e-10
North	4.125	3.40e+02	3.68e+01	0.062	0.602	0.97	1.50e-09	1.62e-10
South	4.375	2.14e+02	2.25e+01	0.088	0.762	0.97	6.09e-10	6.42e-11
North	4.375	1.32e+02	1.71e+01	0.067	0.672	0.97	6.29e-10	8.18e-11
South	4.750	1.75e+02	2.01e+01	0.091	0.825	0.90	2.73e-10	3.13e-11
North	4.750	7.39e+01	1.87e+01	0.067	0.757	0.89	1.96e-10	4.95e-11
South	5.250	9.28e+00	8.85e+00	0.090	0.915	0.90	1.85e-11	1.77e-11
North	5.250	3.83e+00	4.45e+00	0.065	0.858	0.89	1.32e-11	1.53e-11

Table A.3: The invariant yield, reconstruction efficiency, bin shift correction, and invariant cross section for the South and North MPC

#### A.4 The $4 \times 4B$ cross section and systematic errors

$\mathcal{L}_{4 \times 4B} = 6.65 \text{ pb}^{-1}$										
$p_T \text{ bin}$	$X\text{-section}$	$\sigma_{xc}$	$s_{final}$	$s_{escale}$	$s_{yield}$	$s_{trig}$	$s_{geant}$	$s_{global}$	$s_{all}$	
2.125	1.08e-06	2.08e-08	4.294e-07	0.123	0.057	0.357	0.060	0.097	0.40	
2.375	4.38e-07	6.55e-09	1.630e-07	0.117	0.049	0.331	0.060	0.097	0.37	
2.625	1.77e-07	2.08e-09	5.321e-08	0.129	0.040	0.243	0.060	0.097	0.30	
2.875	7.91e-08	1.00e-09	2.179e-08	0.151	0.044	0.195	0.060	0.097	0.28	
3.125	3.42e-08	6.18e-10	8.733e-09	0.158	0.030	0.162	0.060	0.097	0.26	
3.375	1.43e-08	3.43e-10	3.745e-09	0.193	0.057	0.121	0.060	0.097	0.26	
3.625	6.61e-09	1.98e-10	1.769e-09	0.204	0.085	0.100	0.060	0.097	0.27	
3.875	3.20e-09	1.31e-10	1.019e-09	0.266	0.108	0.076	0.060	0.097	0.32	
4.125	1.31e-09	9.03e-11	4.083e-10	0.270	0.084	0.064	0.060	0.097	0.31	
4.375	6.17e-10	5.05e-11	2.413e-10	0.315	0.194	0.057	0.060	0.097	0.39	
4.750	2.51e-10	2.65e-11	9.028e-11	0.335	0.049	0.043	0.060	0.097	0.36	
5.250	1.55e-11	1.16e-11	9.689e-12	0.387	0.477	0.035	0.060	0.097	0.63	

Table A.4: The  $4 \times 4B$  cross section and systematic errors.

## Appendix B

### Tables For $A_N$ vs $x_F$

## B.1 $A_N$ vs $x_F$ Minimum Bias triggered dataset

$x_F$ bin	$A_N^{peak}$	$\sigma_{A_N^{peak}}$	$A_N^{left}$	$\sigma_{A_N^{left}}$	$A_N^{right}$	$\sigma_{A_N^{right}}$	$A_N^{bg}$	$\sigma_{A_N^{bg}}$	$A_N^\eta$	$\sigma_{A_N^\eta}$
South MPC										
-0.2 < $x_F$ < -0.3	0.0002	0.0128	-0.0169	0.0124	-0.0023	0.0173	-0.0119	0.0101	0.0243	0.0431
-0.3 < $x_F$ < -0.4	-0.0552	0.0458	-0.0647	0.0579	-0.0711	0.0749	-0.0671	0.0458	-0.0463	0.0869
0.2 < $x_F$ < 0.3	0.0051	0.0150	-0.0282	0.0144	-0.0131	0.0203	-0.0231	0.0118	0.0609	0.0502
0.3 < $x_F$ < 0.4	0.0944	0.0535	-0.1000	0.0673	0.0419	0.0868	-0.0467	0.0532	0.1996	0.1015
North MPC										
-0.2 < $x_F$ < -0.3	0.0154	0.0173	0.0050	0.0184	0.0248	0.0227	0.0129	0.0143	0.0199	0.0550
-0.3 < $x_F$ < -0.4	0.0518	0.0622	0.1461	0.0867	-0.2089	0.1101	0.0102	0.0681	0.0766	0.1072
0.2 < $x_F$ < 0.3	-0.0015	0.0147	-0.0133	0.0156	0.0326	0.0193	0.0049	0.0121	-0.0129	0.0466
0.3 < $x_F$ < 0.4	-0.0571	0.0525	0.0202	0.0747	-0.0034	0.0922	0.0109	0.0580	-0.0975	0.0905

Table B.1: The various  $A_N$  values for the Minimum Bias triggered dataset.

## B.2 $A_N$ vs $x_F$ for 4×4B triggered dataset

$x_F$ bin	$A_N^{peak}$	$\sigma_{A_N^{peak}}$	$A_N^{left}$	$\sigma_{A_N^{left}}$	$A_N^{right}$	$\sigma_{A_N^{right}}$	$A_N^{bg}$	$\sigma_{A_N^{bg}}$	$A_N^\eta$	$\sigma_{A_N^\eta}$
South MPC										
-0.3 < $x_F$ < -0.4	0.0063	0.0141	0.0103	0.0123	0.0077	0.0352	0.0100	0.0116	0.0035	0.0263
-0.4 < $x_F$ < -0.5	0.0292	0.0113	-0.0147	0.0159	-0.0788	0.0259	-0.0322	0.0135	0.0617	0.0187
-0.5 < $x_F$ < -0.6	0.0072	0.0219	-0.0804	0.0399	-0.0217	0.0408	-0.0517	0.0285	0.0384	0.0367
-0.6 < $x_F$ < -0.7	0.0054	0.0717	0.1158	0.1443	0.1266	0.1187	0.1222	0.0917	-0.0605	0.1235
0.3 < $x_F$ < 0.4	0.0145	0.0179	0.0179	0.0151	0.0162	0.0445	0.0177	0.0143	0.0121	0.0332
0.4 < $x_F$ < 0.5	0.0634	0.0137	0.0163	0.0188	0.0011	0.0317	0.0123	0.0162	0.0905	0.0226
0.5 < $x_F$ < 0.6	0.0573	0.0257	0.1012	0.0460	-0.0036	0.0484	0.0514	0.0334	0.0604	0.0431
0.6 < $x_F$ < 0.7	0.0589	0.0823	0.1294	0.1619	-0.3270	0.1368	-0.1370	0.1045	0.1693	0.1416
North MPC										
-0.3 < $x_F$ < -0.4	0.0270	0.0270	0.0203	0.0242	0.0041	0.0585	0.0179	0.0223	0.0334	0.0490
-0.4 < $x_F$ < -0.5	-0.0415	0.0222	-0.0007	0.0322	-0.0878	0.0506	-0.0258	0.0272	-0.0492	0.0355
-0.5 < $x_F$ < -0.6	0.0297	0.0401	-0.0463	0.0739	0.0183	0.0823	-0.0175	0.0550	0.0517	0.0642
-0.6 < $x_F$ < -0.7	-0.1115	0.1270	-0.0342	0.2971	-0.4513	0.2192	-0.3042	0.1764	-0.0230	0.2022
0.3 < $x_F$ < 0.4	0.0623	0.0204	0.0195	0.0184	-0.0463	0.0451	0.0101	0.0170	0.0996	0.0370
0.4 < $x_F$ < 0.5	0.0544	0.0179	0.0511	0.0260	0.0163	0.0398	0.0407	0.0217	0.0610	0.0286
0.5 < $x_F$ < 0.6	0.0243	0.0333	0.0786	0.0607	0.0661	0.0674	0.0730	0.0451	0.0016	0.0532
0.6 < $x_F$ < 0.7	0.2029	0.1080	0.1634	0.2449	0.1324	0.1844	0.1437	0.1473	0.2300	0.1715

Table B.2: The various  $A_N$  values for the 4×4B data.

### B.3 $A_N$ vs $x_F$ final

$x_F$	$A_N^\eta$	$\sigma_{A_N^\eta}$	$\sigma_{syst}$
-0.629	-0.0503	0.1054	0.0018
-0.535	0.0417	0.0319	0.0055
-0.444	0.0376	0.0165	0.0027
-0.358	0.0094	0.0219	0.0012
-0.231	0.0226	0.0339	0.0167
0.231	0.0212	0.0342	0.0177
0.358	0.0491	0.0232	0.0032
0.444	0.0792	0.0177	0.0022
0.535	0.0372	0.0335	0.0059
0.629	0.1939	0.1092	0.0281

Table B.3: The final  $x_F$  dependent  $A_N$  values.

## **Appendix C**

### **Plots for $A_N$ vs $p_T$**

Summary plots for procuring the  $p_T$  dependence of  $A_N$ . The procedure to obtain the plots is outlined in Section 5.6.

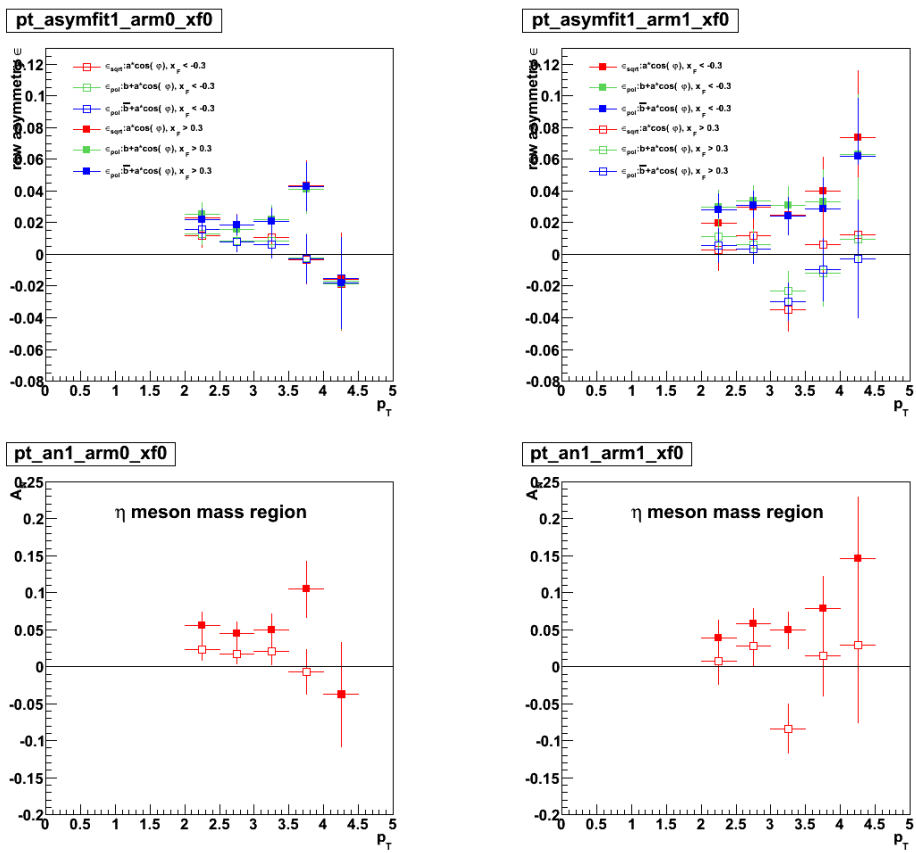


Figure C.1: Asymmetries in the  $\eta$  mass region. The left (right) is for the South (North) MPC. The top panels display the raw asymmetry, and the blue points in these figures are used to calculate  $A_N$ , shown in the bottom panels)

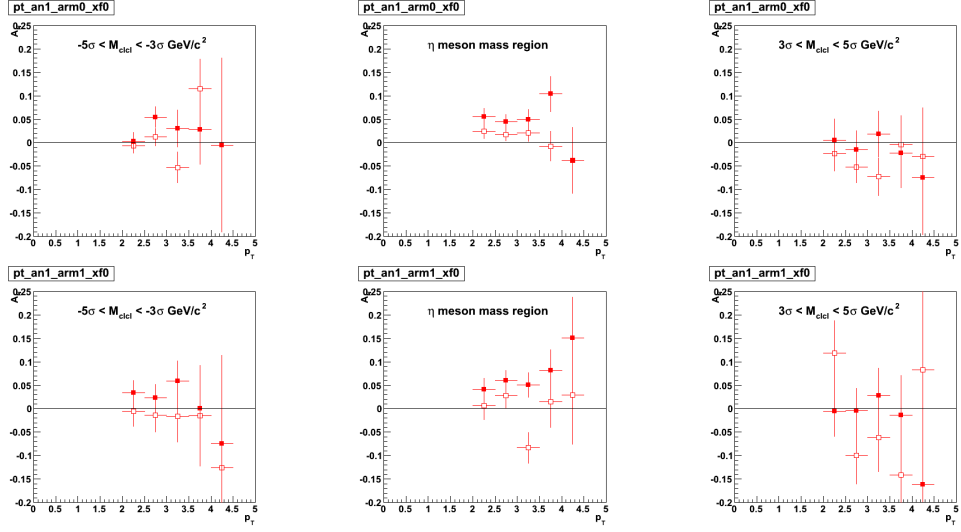


Figure C.2:  $p_T$  Asymmetries in the different invariant mass regions. The top (bottom) row is for the South (North) MPC

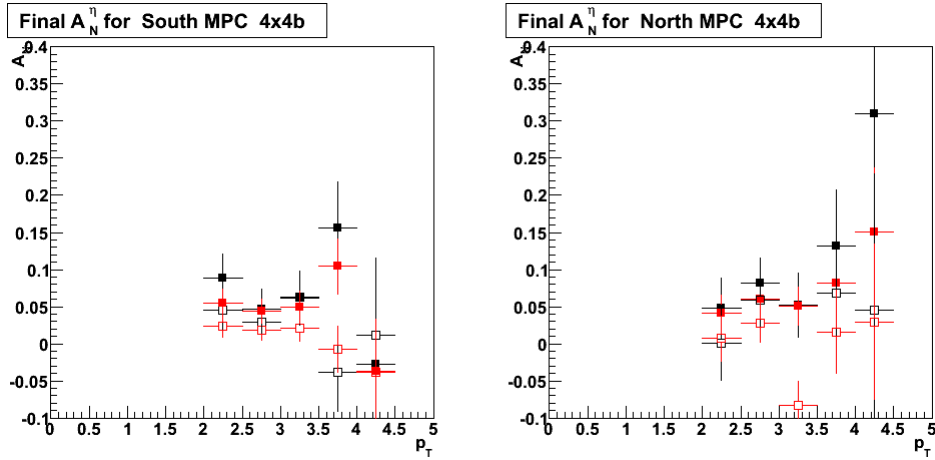


Figure C.3: The background corrected values of  $A_N^\eta$  for the  $4 \times 4B$  triggered dataset. The left (right) plot is for the South (North) MPC.

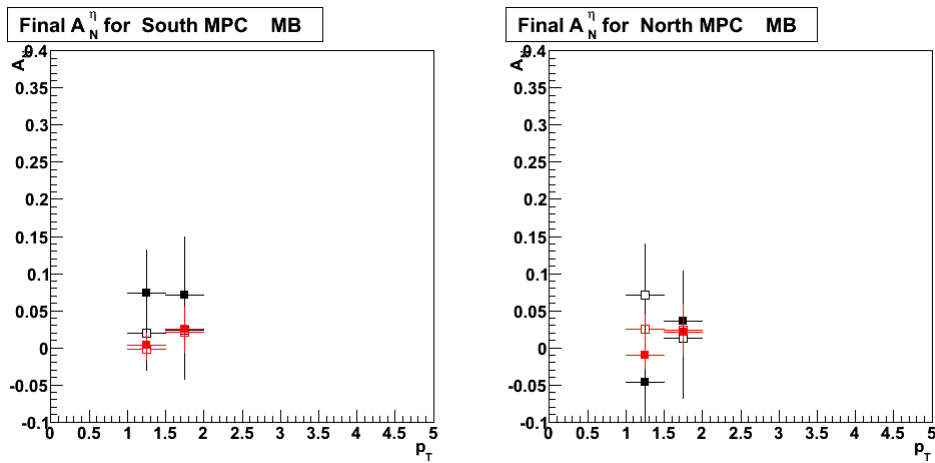


Figure C.4: The background corrected values of  $A_N^\eta$  for the Minimum Bias triggered dataset. The left (right) plot is for the South (North) MPC.

## Appendix D

### Tables for $A_N$ vs $p_T$

## D.1 $A_N$ vs $p_T$ South and North

$p_T$ bin	$A_N^{peak}$	$\sigma_{A_N^{peak}}$	$A_N^{left}$	$\sigma_{A_N^{left}}$	$A_N^{right}$	$\sigma_{A_N^{right}}$	$A_N^{bg}$	$\sigma_{A_N^{bg}}$	$A_N^\eta$	$\sigma_{A_N^\eta}$
South MPC, $x_F < -0.2$										
$1.0 < p_T < 1.5$	-0.0022	0.0140	-0.0140	0.0127	-0.0084	0.0180	-0.0121	0.0104	0.0191	0.0495
$1.5 < p_T < 2.0$	0.0214	0.0257	0.0077	0.0253	0.0502	0.0398	0.0199	0.0214	0.0234	0.0663
$2.0 < p_T < 2.5$	0.0234	0.0144	-0.0062	0.0158	-0.0235	0.0363	-0.0090	0.0145	0.0442	0.0255
$2.5 < p_T < 3.0$	0.0171	0.0130	0.0123	0.0185	-0.0525	0.0330	-0.0032	0.0162	0.0276	0.0215
$3.0 < p_T < 3.5$	0.0206	0.0178	-0.0526	0.0329	-0.0726	0.0402	-0.0606	0.0255	0.0612	0.0296
$3.5 < p_T < 4.0$	-0.0069	0.0304	0.1150	0.0636	-0.0042	0.0624	0.0543	0.0445	-0.0383	0.0513
$4.0 < p_T < 4.5$	-0.0368	0.0576	-0.3500	0.1531	-0.0287	0.1031	-0.1290	0.0855	0.0140	0.1010
North MPC, $x_F < -0.2$										
$1.0 < p_T < 1.5$	0.0249	0.0197	-0.0056	0.0213	0.0125	0.0246	0.0022	0.0161	0.0715	0.0687
$1.5 < p_T < 2.0$	0.0233	0.0352	0.0623	0.0391	-0.0240	0.0554	0.0336	0.0320	0.0122	0.0805
$2.0 < p_T < 2.5$	0.0070	0.0307	-0.0049	0.0328	0.1184	0.0689	0.0179	0.0296	0.0008	0.0509
$2.5 < p_T < 3.0$	0.0280	0.0261	-0.0142	0.0359	-0.0995	0.0609	-0.0361	0.0309	0.0591	0.0415
$3.0 < p_T < 3.5$	-0.0837	0.0328	-0.0162	0.0545	-0.0613	0.0729	-0.0324	0.0437	-0.1090	0.0535
$3.5 < p_T < 4.0$	0.0153	0.0551	-0.0151	0.1073	-0.1413	0.1072	-0.0783	0.0758	0.0678	0.0959
$4.0 < p_T < 4.5$	0.0295	0.1050	-0.1256	0.2360	0.0834	0.1878	0.0023	0.1470	0.0450	0.1853
South MPC, $x_F > 0.2$										
$1.0 < p_T < 1.5$	0.0039	0.0163	-0.0266	0.0148	-0.0327	0.0210	-0.0286	0.0121	0.0740	0.0576
$1.5 < p_T < 2.0$	0.0244	0.0301	-0.0039	0.0296	-0.0276	0.0466	-0.0108	0.0250	0.0714	0.0777
$2.0 < p_T < 2.5$	0.0552	0.0187	0.0025	0.0192	0.0049	0.0454	0.0029	0.0177	0.0889	0.0328
$2.5 < p_T < 3.0$	0.0444	0.0164	0.0544	0.0221	-0.0148	0.0405	0.0385	0.0194	0.0475	0.0269
$3.0 < p_T < 3.5$	0.0497	0.0221	0.0304	0.0392	0.0182	0.0486	0.0256	0.0305	0.0618	0.0365
$3.5 < p_T < 4.0$	0.1046	0.0376	0.0281	0.0745	-0.0218	0.0745	0.0032	0.0527	0.1565	0.0630
$4.0 < p_T < 4.5$	-0.0375	0.0704	-0.0052	0.1855	-0.0744	0.1215	-0.0536	0.1016	-0.0286	0.1227
North MPC, $x_F > 0.2$										
$1.0 < p_T < 1.5$	-0.0107	0.0166	-0.0207	0.0181	0.0435	0.0209	0.0067	0.0137	-0.0465	0.0580
$1.5 < p_T < 2.0$	0.0205	0.0300	0.0247	0.0333	-0.0297	0.0471	0.0066	0.0272	0.0353	0.0687
$2.0 < p_T < 2.5$	0.0393	0.0236	0.0343	0.0260	-0.0057	0.0537	0.0267	0.0234	0.0463	0.0391
$2.5 < p_T < 3.0$	0.0586	0.0201	0.0232	0.0281	-0.0040	0.0480	0.0163	0.0243	0.0791	0.0321
$3.0 < p_T < 3.5$	0.0491	0.0252	0.0593	0.0428	0.0281	0.0583	0.0484	0.0345	0.0495	0.0414
$3.5 < p_T < 4.0$	0.0792	0.0425	0.0008	0.0866	-0.0135	0.0839	-0.0065	0.0603	0.1273	0.0744
$4.0 < p_T < 4.5$	0.1460	0.0832	-0.0747	0.1890	-0.1617	0.1550	-0.1267	0.1198	0.3022	0.1477

Table D.1: The various  $A_N$  values for the  $p_T$  data.

## D.2 $A_N$ vs $p_T$ final

$p_T$ bin ( $x_F < -0.2$ )	$A_N^\eta$	$\sigma_{A_N^\eta}$	$\sigma_{syst}$
1.242	0.0370	0.0401	0.0110
1.682	0.0189	0.0512	0.0005
2.269	0.0355	0.0228	0.0032
2.733	0.0343	0.0191	0.0072
3.213	0.0214	0.0259	0.0034
3.700	-0.0147	0.0452	0.0009
4.188	0.0211	0.0887	0.0054
$p_T$ bin ( $x_F > 0.2$ )	$A_N^\eta$	$\sigma_{A_N^\eta}$	$\sigma_{syst}$
1.242	0.0143	0.0409	0.0110
1.682	0.0511	0.0514	0.0005
2.269	0.0713	0.0251	0.0032
2.733	0.0605	0.0206	0.0072
3.213	0.0564	0.0274	0.0034
3.700	0.1443	0.0480	0.0009
4.188	0.1066	0.0944	0.0054

Table D.2: The final  $p_T$  dependent  $A_N$  values.

## Appendix E

### Bunch shuffling plots

Plots demonstrating bunch shuffling (see Section 5.8.3) for Minimum Bias and 4×4B triggered dataset in the South and North MPC using both the  $\epsilon_{sqrt}$  and  $\epsilon_{pol}$  formulas.

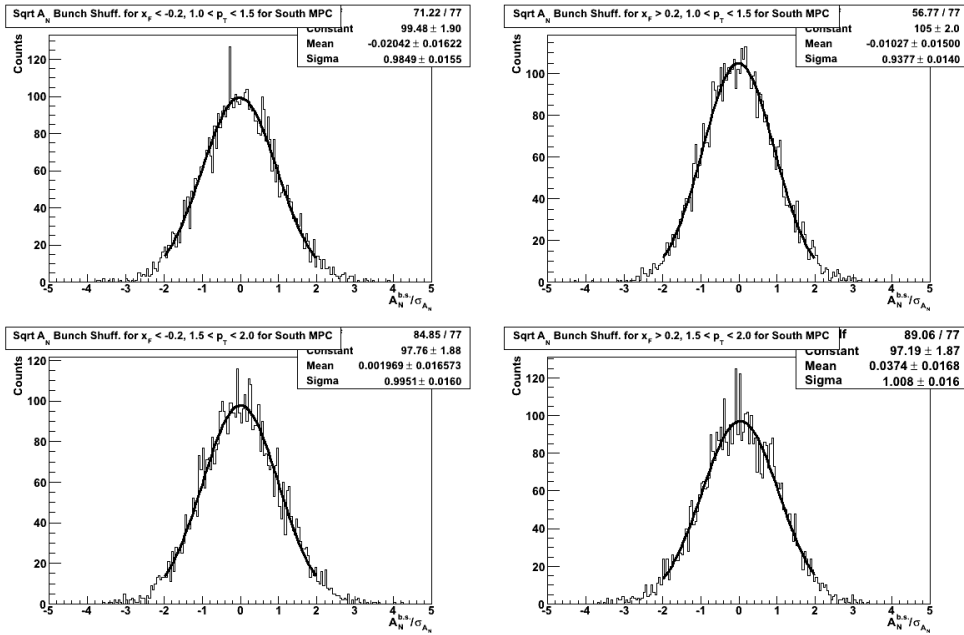


Figure E.1: The  $x_F$  bunch shuffling results for Minimum Bias triggered dataset using the South MPC using  $\epsilon_{sqrt}$  formula.

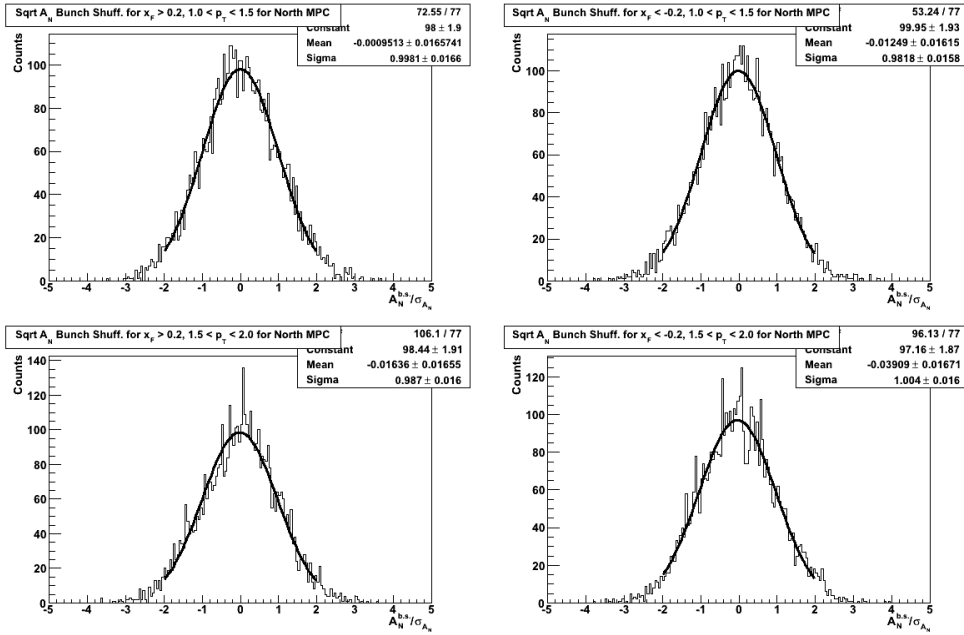


Figure E.2: The  $x_F$  bunch shuffling results for Minimum Bias triggered dataset using the North MPC using  $\epsilon_{sqrt}$  formula.

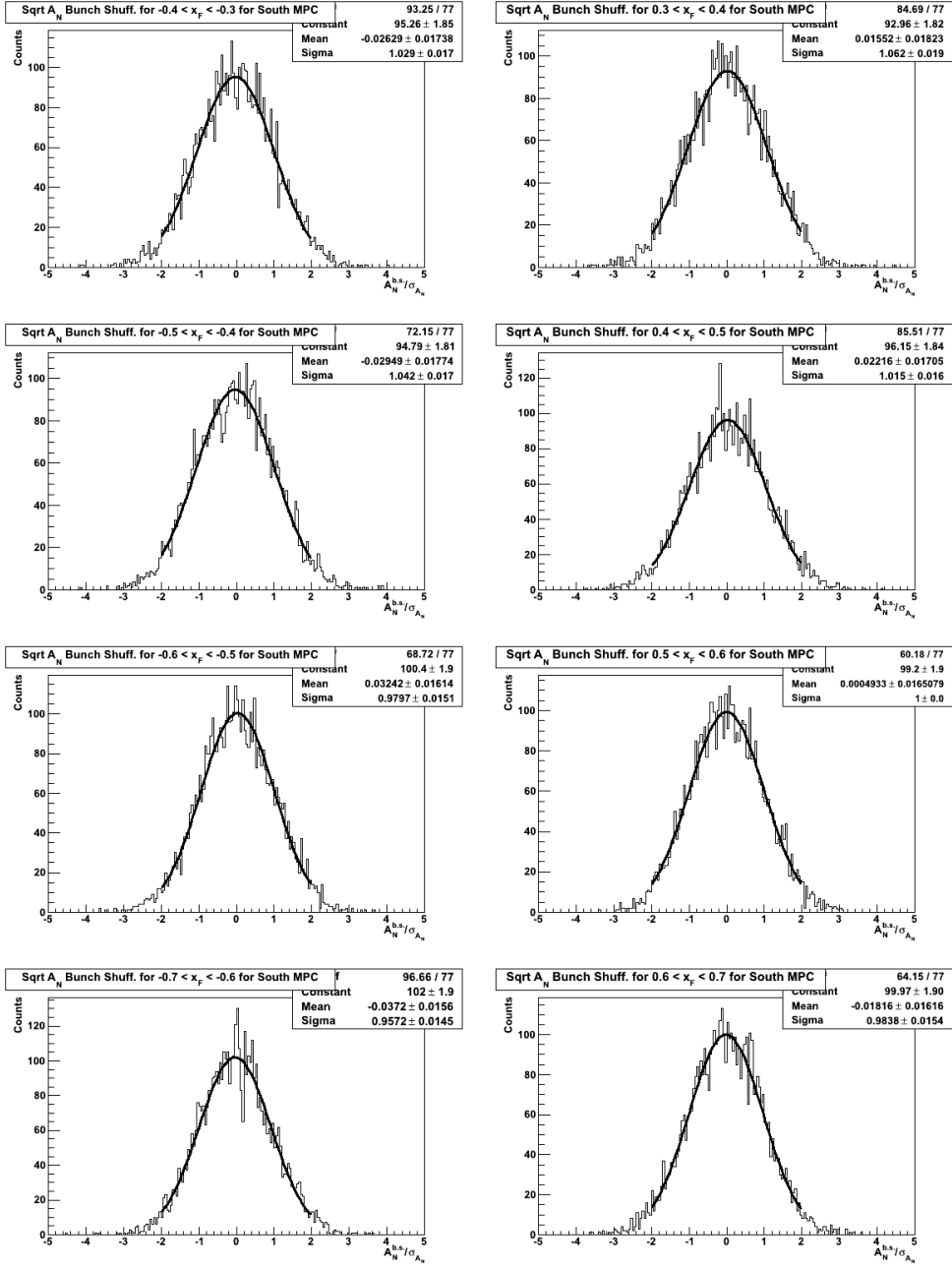


Figure E.3: The  $x_F$  bunch shuffling results for 4×4B triggered dataset using the South MPC using  $\epsilon_{\text{sqrt}}$  formula.

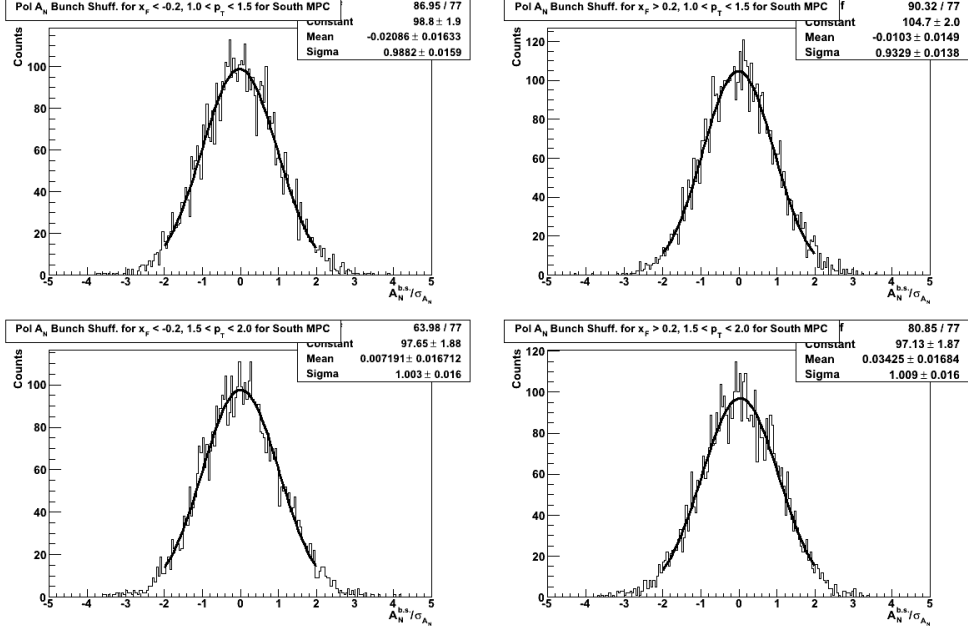


Figure E.4: The  $x_F$  bunch shuffling results for Minimum Bias triggered dataset using the South MPC using  $\epsilon_{pol}$  formula.

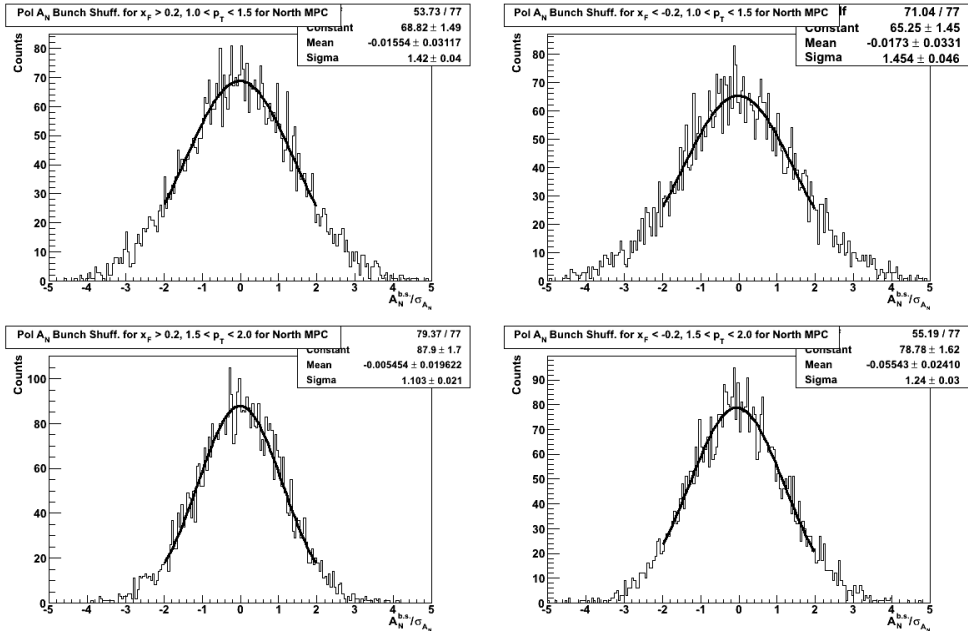


Figure E.5: The  $x_F$  bunch shuffling results for Minimum Bias triggered dataset using the North MPC using  $\epsilon_{pol}$  formula.

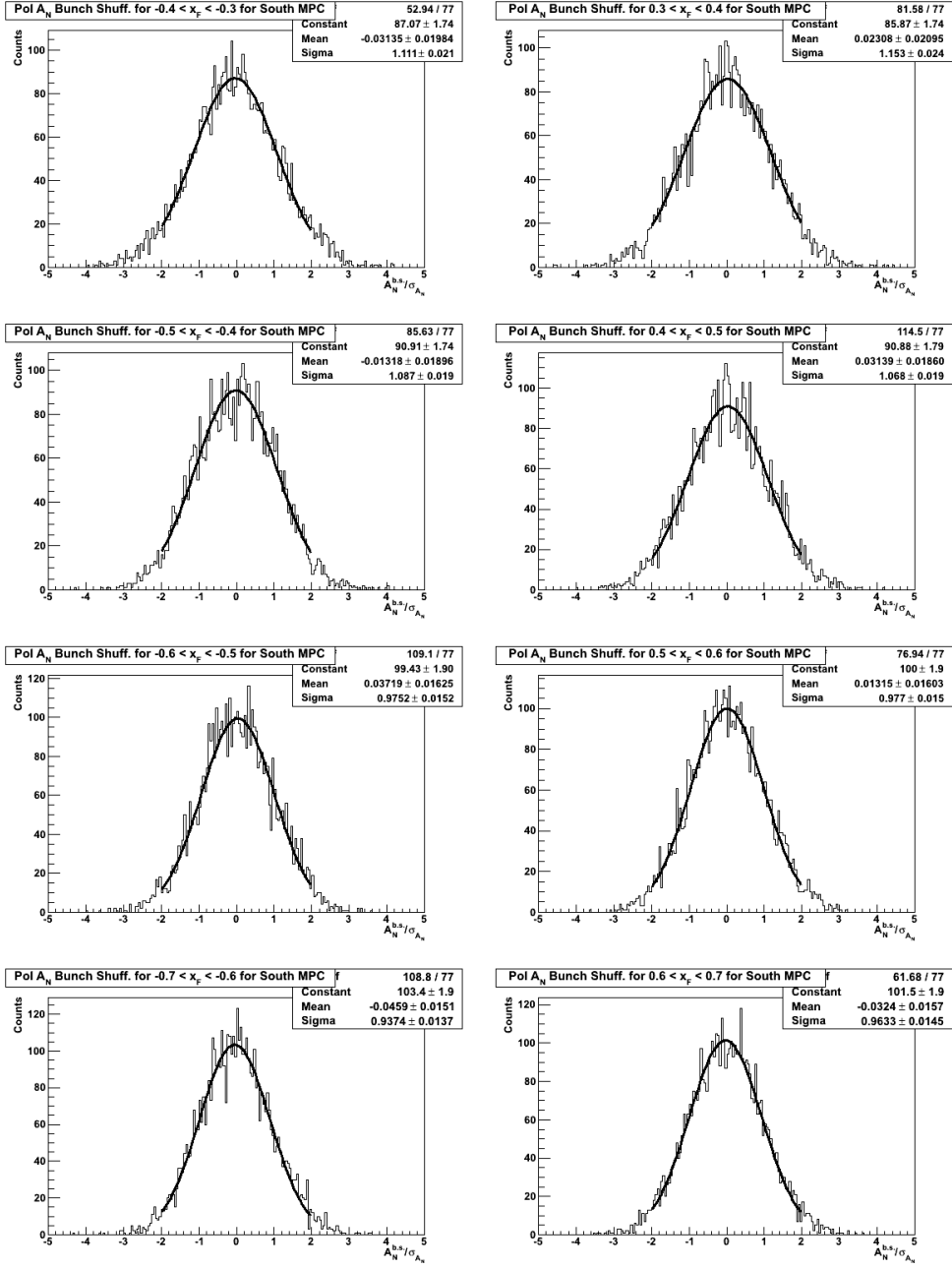


Figure E.6: The  $x_F$  bunch shuffling results for 4×4B triggered dataset using the South MPC using polarization formula.

# Bibliography

- [1] I. Estermann, R. Frisch, and O. Stern, “The spin,” *Nature*, vol. 132, p. 169, 1933.
- [2] R. P. Feynman, “Very high-energy collisions of hadrons,” *Phys. Rev. Lett.*, vol. 23, pp. 1415–1417, 1969.
- [3] J. D. Bjorken, “Asymptotic sum rules at infinite momentum,” *Phys. Rev.*, vol. 179, pp. 1547–1553, 1969.
- [4] J. D. Bjorken and E. A. Paschos, “Inelastic electron-proton and  $\gamma$ -proton scattering and the structure of the nucleon,” *Phys. Rev.*, vol. 185, pp. 1975–1982, 1969.
- [5] R. Brandelik *et al.*, “Evidence for planar events in e+e annihilation at high energies,” *Phys. Lett. B*, vol. 86, pp. 243–249, 1979.
- [6] C. Berger *et al.*, “Evidence for gluon bremsstrahlung in e+e annihilations at high energies,” *Phys. Lett. B*, vol. 86, pp. 418–425, 1979.
- [7] W. Bartel *et al.*, “Observation of planar three-jet events in e+e annihilation and evidence for gluon bremsstrahlung,” *Phys. Lett. B*, vol. 91, pp. 142–147, 1979.
- [8] D. J. Gross and F. Wilczek, “Ultraviolet behavior of non-abelian gauge theories,” *Phys. Rev. Lett.*, vol. 30, pp. 1343–1346, 1973.
- [9] H. D. Politzer, “Reliable perturbative results for strong interactions?,” *Phys. Rev. Lett.*, vol. 30, pp. 1346–1349, 1973.
- [10] J. Ashman *et al.*, “A measurement of the spin asymmetry and determination of the structure function  $g_1$  in deep inelastic muon proton scattering,” *Phys. Lett.*, vol. B206, p. 364, 1988.
- [11] J. Ashman *et al.*, “An investigation of the spin structure of the proton in deep inelastic scattering of polarized muons on polarized protons,” *Phys. Lett.*, vol. B328, p. 364, 1989.
- [12] D. Adams *et al.*, “Analyzing power in inclusive + and - production at high  $xf$  with a 200 gev polarized proton beam,” *Phys. Lett.*, vol. B264, p. 464, 1991.
- [13] D. Adams *et al.*, “Comparison of spin asymmetries and cross sections in 0 production by 200 gev polarized antiprotons and protons,” *Phys. Lett.*, vol. B261, p. 201, 1991.

- [14] G. Altarelli and W. J. Striling, “Phenomenology of the anomalous gluon contribution to polarized lepto production,” *Part. World.*, vol. 1, pp. 40–52, 1989.
- [15] R. D. Carlitz and G. G. Ross, “The role of the axial anomaly in measuring spin dependent parton distributions,” *Phys. Lett.*, vol. B212, p. 391, 1988.
- [16] R. D. Carlitz, J. C. Collins, and A. H. Mueller, “The role of the axial anomaly in measuring spin dependent parton distributions,” *Phys. Lett.*, vol. B214, p. 229, 1988.
- [17] G. Altarelli and G. Parisi, “Asymptotic freedom in parton language,” *Nucl. Phys.*, vol. B126, p. 298, 1977.
- [18] E. Aschenauer *et al.*, “The rhic spin program, achievements and future opportunities,” tech. rep., Brookhaven National Laboratory, 2012. <http://www.bnl.gov/npp/docs/RHIC-Spin-WriteUp-121105.pdf>.
- [19] J. Collins, *Foundations of perturbative QCD*. Cambridge University Press, Mar 2014.
- [20] R. Ellis, H. Georgi, M. Machacek, H. Politzer, and G. Ross, “Factorization and the parton model in qcd.,” *Phys. Lett.*, vol. B78, p. 281, 1978.
- [21] R. Ellis, H. Georgi, M. Machacek, H. Politzer, and G. Ross, “Perturbation theory and the parton model in qcd.,” *Nucl. Phys.*, vol. B152, p. 285, 1979.
- [22] F. Halzen and A. D. Martin, *Quarks and Leptons*. Wiley, 1985.
- [23] M. E. Peskin and D. V. Schroeder, *An Introduction To Quantum Field Theory (Frontiers in Physics)*. Westview Press, 1995.
- [24] K. Boyle, *Measurements of the Double Helicity Asymmetry in Pion Production in Proton Collisions at  $\sqrt{s} = 200 \text{ GeV}$  and the Resulting Constraints on the Polarized Gluon Distribution in the Proton*. PhD thesis, Stony Brook University, 2008.
- [25] A. Adare *et al.*, “Cross section and double helicity asymmetry for  $\eta$  mesons and their comparison to  $\pi^0$  production in  $p + p$  collisions at  $\sqrt{s} = 200 \text{ GeV}$ ,” *Phys. Rev. D*, vol. 83, p. 032001, Feb 2011. <http://link.aps.org/doi/10.1103/PhysRevD.83.032001>.
- [26] C. A. Aidala, F. Ellinghaus, R. Sassot, J. P. Seele, and M. Stratmann, “Global analysis of fragmentation functions for eta mesons,” *Phys. Rev. D*, vol. 83, p. 034002, Feb 2011.
- [27] A. Martin, W. Stirling, R. Thorne, , and G. Watt, “Update of parton distributions at nnlo.,” *Phys. Lett.*, vol. B652, p. 292299, 2007.
- [28] HEPDATA, “The durham hep databases,” 2003. <http://durpdg.dur.ac.uk>.
- [29] D. de Florian, R. Sassot, M. Stratmann, and W. Vogelsang, “Extraction of spin-dependent parton densities and their uncertainties,” *Phys. Rev. D*, vol. 80, p. 034030, 2009.
- [30] J. Ralston and D. Soper, “Production of dimuons from high-energy polarized proton proton collisions.,” *Nucl. Phys.*, vol. B152, p. 109, 1979.

- [31] W. Vogelsang, M. Stratmann, and A. Mukherjee, “Double-transverse spin asymmetries at nlo,” in *Conference on the Intersections of Particle and Nuclear Physics (CIPANP)*, May 2003.
- [32] R. Jaffe and X. Ji, “Chiral-odd parton distributions and drellyan processes,” *Nucl. Phys.*, vol. B375, p. 527, 1992.
- [33] M. Mulders and R. Tangermann, “The complete tree-level result up to order  $1/q$  for polarized deep-inelastic lepto-production,” *Nucl. Phys.*, vol. B461, p. 197, 1996. *Erratum: ibid.* **B484** (1997) 538.
- [34] R. L. Jaffe and X. Ji, “Chiral-odd parton distributions and polarized drell-yan process,” *Phys. Rev. Lett.*, vol. 67, pp. 552–555, Jul 1991.
- [35] T. C. Rogers and P. J. Mulders, “No generalized tmd-factorization in hadro-production of high transverse momentum hadrons,” *Phys.Rev.*, vol. D81, p. 094006, 2010.
- [36] T. C. Rogers, “Extra spin asymmetries from the breakdown of tmd-factorization in hadron-hadron collisions,” *Phys.Rev.*, vol. D88, p. 014002, 2013.
- [37] G. L. Kane, J. Pumplin, and W. Repko, “Transverse quark polarization in large  $p(t)$  reactions,  $e+ e-$  jets, and leptonproduction: A test of qcd,” *Phys. Rev. Lett.*, vol. 41, p. 1689, 1978.
- [38] W. H. Dragoset, J. B. Roberts, J. E. Bowers, H. W. Courant, H. Kagan, M. L. Marshak, E. A. Peterson, K. Ruddick, and R. D. Klem, “Asymmetries in inclusive proton-nucleon scattering at 11.75 gev/  $c$ ,” *Phys. Rev. D*, vol. 18, pp. 3939–3954, Dec 1978.
- [39] S. Saroff, B. R. Baller, G. C. Blazey, H. Courant, K. J. Heller, M. L. Marshak, M. A. Shupe, D. S. Barton, G. Bunce, A. S. Carroll, S. Gushue, Y. I. Makdisi, L. Remsberg, S. Heppelmann, and J. J. Russell, “Single-spin asymmetry in inclusive reactions  $p^\uparrow + p \rightarrow \pi^+ + x$ ,  $\pi^- + x$ , and  $p + x$  at 13.3 and 18.5 gev/  $c$ ,” *Phys. Rev. Lett.*, vol. 64, pp. 995–998, Feb 1990.
- [40] C. E. Allgower *et al.*, “Measurement of analyzing powers of  $\pi^+$  and  $\pi^-$  produced on a hydrogen and a carbon target with a 22GeV/ $c$  incident polarized proton beam,” *Phys. Rev. D*, vol. 65, p. 092008, May 2002.
- [41] I. Arsene *et al.*, “Single-transverse-spin asymmetries of identified charged hadrons in polarized  $pp$  collisions at  $\sqrt{s} = 62.4$  GeV,” *Phys. Rev. Lett.*, vol. 101, p. 042001, Jul 2008.
- [42] B. I. Abelev *et al.*, “Forward neutral-pion transverse single-spin asymmetries in  $p + p$  collisions at  $\sqrt{s} = 200$  GeV,” *Phys. Rev. Lett.*, vol. 101, p. 222001, Nov 2008.
- [43] M. Chiu *et al.*, “Measurement of transverse-single-spin asymmetries for midrapidity and forward-rapidity production of hadrons in polarized  $p + p$  collisions at  $\sqrt{s} = 200$  and 62.4 gev.” <http://arxiv.org/abs/1312.1995>.
- [44] D. Sivers, “Single-spin production asymmetries from the hard scattering of pointlike constituents,” *Phys. Rev. D*, vol. 41, pp. 83–90, Jan 1990.

- [45] D. Sivers, “Hard-scattering scaling laws for single-spin production asymmetries,” *Phys. Rev. D*, vol. 43, pp. 261–263, Jan 1991.
- [46] A. Bacchetta and M. Radici, “Constraining quark angular momentum through semi-inclusive measurements,” *Phys. Rev. Lett.*, vol. 107, p. 212001, Nov 2011.
- [47] A. Bacchetta and M. Contalbrigo, “The proton in 3d,” *Il Nuovo Saggiatore (Italian)*, vol. 28, pp. 16–27, 2012.
- [48] J. Collins, “Fragmentation of transversely polarized quarks probed in transverse momentum distributions,” *Nucl. Phys.*, vol. B396, p. 161, 1993.
- [49] M. Anselmino, , *et al.*, “Simultaneous extraction of transversity and collins functions from new semi-inclusive deep inelastic scattering and  $e^+e^-$  data,” *Phys. Rev. D*, vol. 87, p. 094019, May 2013.
- [50] J. Qiu and G. Sterman, “Single transverse-spin asymmetries in hadronic pion production,” *Phys. Rev. D*, vol. 59, p. 014004, Nov 1998.
- [51] Y. Kanazawa and Y. Koike, “Chiral-odd contribution to single-transverse spin asymmetry in hadronic pion production,” *Phys. Lett.*, vol. B478, p. 121, 1991.
- [52] K. Kanazawa and Y. Koike, “New analysis of the single transverse-spin asymmetry for hadron production at rhic,” *Phys. Rev. D*, vol. 82, p. 034009, Aug 2010.
- [53] X. Ji, J.-W. Qiu, W. Vogelsang, and F. Yuan, “Unified picture for single transverse-spin asymmetries in hard-scattering processes,” *Phys. Rev. Lett.*, vol. 97, p. 082002, Aug 2006.
- [54] Z.-B. Kang, J.-W. Qiu, and H. Zhang, “Quark-gluon correlation functions relevant to single transverse spin asymmetries,” *Phys. Rev. D*, vol. 81, p. 114030, Jun 2010.
- [55] Z. B. Kang, “Single transverse-spin asymmetry in inclusive hadron production,” June 2010. [http://ntc0.lbl.gov/~fyuan/spin10/Zhongbo\\_Kang.pdf](http://ntc0.lbl.gov/~fyuan/spin10/Zhongbo_Kang.pdf).
- [56] D. Adams *et al.*, “Measurement of single spin asymmetry in -meson production in pp and pp interactions in the beam fragmentation region at 200 gev/c,” *Nucl. Phys.*, vol. B510, p. 3, 1998.
- [57] L. Adamczyk *et al.*, “Transverse single-spin asymmetry and cross section for  $\pi^0$  and  $\eta$  mesons at large feynman  $x$  in  $p^\uparrow + p$  collisions at  $\sqrt{s}=200$  GeV,” *Phys. Rev. D*, vol. 86, p. 051101, Sep 2012.
- [58] K. Kanazawa and Y. Koike, “A phenomenological study of single transverse-spin asymmetry for inclusive light-hadron productions at rhic,” *Phys. Rev. D*, vol. 83, p. 114024, Jun 2011.
- [59] K. Adcox *et al.*, “Phenix detector overview.,” *Nucl. Instrum. Meth.*, vol. A499, p. 469479, 2003.
- [60] K. Ackerman *et al.*, “The star detector overview,” *Nucl. Instrum. Meth.*, vol. A499, pp. 624–632, 2003.
- [61] B. Back *et al.*, “The phobos detector at rhic.,” *Nucl. Instrum. Meth.*, vol. A499, pp. 437–468, 2003.

- [62] M. Adamczyk *et al.*, “The brahms detector at rhic.,” *Nucl. Instrum. Meth.*, vol. A499, pp. 603–623, 2003.
- [63] I. Alekseev *et al.*, “Polarized proton collider at rhic,” *Nucl. Instrum. Meth.*, vol. A499, pp. 392–414, 2003.
- [64] Y. Derbenev *et al.*, “Polarized proton collider at rhic,” *Part. Accel.*, vol. 8, p. 115, 1978.
- [65] I. Zelenski *et al.*, “Absolute polarized h-jet polarimeter development, for rhic.,” *Nucl. Instrum. Meth.*, vol. A536, pp. 248–254, 2005.
- [66] H. Okada *et al.*, “Measurement of the analyzing power an in pp elastic scattering in the cni region with a polarized atomic hydrogen gas jet target,” *Phys. Lett. B*, vol. 638, pp. 450–454, 2006.
- [67] C. Adler *et al.*, “The rhic zero degree calorimeters,” *Nucl. Instrum. Meth.*, vol. A470, pp. 488–499, 2001.
- [68] Y. Fukao *et al.*, “Single transverse-spin asymmetry in very forward and very backward neutral particle production for polarized proton collisions at  $\sqrt{s}=200$  gev,” *Phys. Lett. B*, vol. 650, pp. 325–330, 2007.
- [69] C. Aidla, *Measurement of the Transverse Single-Spin Asymmetry for Mid-rapidity Production of Neutral Pions in Polarized p+p Collisions at 200 GeV Center-of-Mass Energy*. PhD thesis, Columbia University, 2006.
- [70] S. Aronson *et al.*, “Phenix magnet system.,” *Nucl. Instrum. Meth.*, vol. A499, pp. 480–488, 2003.
- [71] K. Adcox *et al.*, “Phenix central arm tracking detectors.,” *Nucl. Instrum. Meth.*, vol. A499, pp. 489–507, 2003.
- [72] M. Aizawa *et al.*, “Phenix central arm particle id detectors.,” *Nucl. Instrum. Meth.*, vol. A499, pp. 508–520, 2003.
- [73] H. Akikawa *et al.*, “Phenix muon arms.,” *Nucl. Instrum. Meth.*, vol. A499, pp. 537–548, 2003.
- [74] M. Allen *et al.*, “Phenix inner detectors.,” *Nucl. Instrum. Meth.*, vol. A499, pp. 549–559, 2003.
- [75] S. Adler *et al.*, “Phenix online systems.,” *Nucl. Instrum. Meth.*, vol. A499, pp. 560–592, 2003.
- [76] S. Adler *et al.*, “Phenix online and offline computing.,” *Nucl. Instrum. Meth.*, vol. A499, pp. 593–602, 2003.
- [77] K. Imai, “Possible polarimetry at collision point (phenix).,” in *RHIC Spin Meeting*, August 1999.
- [78] M. Chiu, “Muon piston calorimeter.,” *PHENIX Letter of Intent.*, 2005.
- [79] J. Koster, *Measurement of Transverse Spin Asymmetries in Polarized Proton-Proton Collisions, and the Realization of New Electromagnetic Calorimeters for Forward Physics*. PhD thesis, University of Illinois, Urbana-Champagne, 2010.

- [80] W. Leo, *Techniques for Nuclear and Particle Physics Experiments: A How-to Approach*. Springer, 1994.
- [81] G. Knoll, *Radiation Detection and Measurement*. John Wiley & Sons, 2010.
- [82] R. Y. Zhu *et al.*, “A study on the properties of lead tungstate crystals,” *Nucl. Instrum. Meth.*, vol. A376, pp. 319–334, 1996.
- [83] B. Meredith, *A Study of Nuclear Effects using Forward-Rapidity Hadron Production and Di-Hadron Angular Correlations in  $\sqrt{s} = 200$  GeV d+Au and p+p Collisions with the PHENIX Detector at RHIC*. PhD thesis, University of Illinois, Urbana-Champaign, 2011.
- [84] J. Beringer *et al.*, “Review of particle physics,” *Phys. Rev. D*, vol. 86, p. 010001, Jul 2012.
- [85] K. J. others, “Phenix analysis note 927. mpc calibration.”
- [86] T. Sjöstrand, S. Mrenna, and P. Z. Skands, “PYTHIA 6.4 Physics and Manual,” *JHEP*, vol. 05, p. 026, 2006.
- [87] S. Agostinelli *et al.*, “Geant4a simulation toolkit,” *Nuclear Instruments and Methods in Physics Research Section A: Accelerators, Spectrometers, Detectors and Associated Equipment*, vol. 506, no. 3, pp. 250 – 303, 2003.
- [88] R. K. *et al.*, “Phenix analysis note 175. measurement of neutral pions in  $\sqrt{s_{\text{NN}}} = 200$  gev p+p-collisions with the pbgl calorimeter.”
- [89] B. S. *et al.*, “Phenix analysis note. determination of the absolute luminosity for the proton-proton data at  $\sqrt{s_{\text{NN}}} = 200$  gev recorded by phenix during rhic run-02.”
- [90] S. Bazilevsky *et al.*, “Phenix analysis note. relative measurements of bbc trigger efficiency in pp runs 2, 3 and 4.”
- [91] M. Stratmann, ““calculation of  $\sigma(p + p \rightarrow \eta + x)$  at forward rapidity using nlo pqcd”.” Private communication.
- [92] E. Leader, *Spin in Particle Physics*. Cambridge University Press, 2001.
- [93] G. G. Ohlsen and P. W. Keatorn Jr., “Techniques for measurement of spin- $\frac{1}{2}$  and spin-1 polarization analyzing tensors,” *Nucl. Instrum. Meth.*, vol. 109, pp. 41–59, 1973.
- [94] S. Dairaku *et al.*, “Phenix analysis note 929. phenix local polarimeter analysis in polarized proton-proton collisions at  $\sqrt{s} = 200$  gev from rhic run-6 and run-8,” 2010.
- [95] K. Kanazawa and Y. Koike, “Private communication. calculation base on [58],” 2011.
- [96] S. Campbell *et al.*, “A proposal for the muon piston calorimeter extension (mpc-ex) to the phenix experiment at rhic phenix collaboration,” January 2013. <http://arxiv.org/abs/1301.1096>.